Effects of Resonant Magnetic Perturbations on the STOR-M Tokamak Discharges

A Thesis Submitted to the College of

Graduate Studies and Research

in Partial Fulfillment of the Requirements

for the Degree of Doctor of Philosophy

in the Department of Physics and Engineering Physics

University of Saskatchewan

Saskatoon

By

Sayf Gamudi Elgriw

Permission to Use

In presenting this thesis in partial fulfilment of the requirements for a Postgraduate degree from the University of Saskatchewan, I agree that the Libraries of this University may make it freely available for inspection. I further agree that permission for copying of this thesis in any manner, in whole or in part, for scholarly purposes may be granted by the professor or professors who supervised my thesis work or, in their absence, by the Head of the Department or the Dean of the College in which my thesis work was done. It is understood that any copying or publication or use of this thesis or parts thereof for financial gain shall not be allowed without my written permission. It is also understood that due recognition shall be given to me and to the University of Saskatchewan in any scholarly use which may be made of any material in my thesis.

Requests for permission to copy or to make other use of material in this thesis in whole or part should be addressed to:

Head of the Department of Physics and Engineering Physics

116 Science Place

University of Saskatchewan

Saskatoon, Saskatchewan

S7N 5E2

Dedicated to my family

Abstract

Studies of resonant magnetic perturbations (RMP) have been an active topic in the tokamak research. The RMP technique involves the use of magnetic perturbations generated by external coils installed on a tokamak device. The resonant interaction between the plasma and RMP has favorable effects on magnetohydrodynamic (MHD) stability and other plasma parameters in tokamaks. The RMP experiments are carried out in the Saskatchewan Torus-Modified (STOR-M) tokamak using ($l = 2$, $n = 1$) helical coils carrying a static current pulse. The effect of RMP on the ($m = 2$, $n = 1$) magnetic islands is examined during ohmic discharges with high MHD activities. The amplitude and frequency of (2, 1) Mirnov fluctuations are significantly reduced after application of RMP. A phase of improved plasma confinement, characterized by a reduction in the H_α emission level and an increase in the soft x-ray (SXR) emission, is induced after application of RMP. It is also observed using the ion Doppler spectroscopy (IDS) that RMP can strongly affect the plasma rotation in STOR-M. It is found that during the RMP pulse, the toroidal velocity of C_{III} impurities (located at the plasma edge) increases in the co-current direction. However, the toroidal velocities of O_V and C_{VI} impurities (located near the plasma core) change direction from counter-current to co-current. The reduction of the toroidal flow velocity is accompanied by a reduction of the MHD frequency. It is also found that radial profiles of ion saturation current and floating potential in the edge region can be modified by RMP. An increase in the pedestal plasma density and a more negative electric field are observed at the plasma edge region during the RMP pulse. An internal probe array is assembled and installed in STOR-M to study the RMP penetration and the plasma response to RMP.

Acknowledgements

The research included in this dissertation could not have been possible without the assistance, patience, and support of many individuals. I would like to extend my gratitude first and foremost to my supervisor Dr. Chijin Xiao for his mentorship over the course of my M.Sc. and Ph.D. studies. His insight has helped me through extremely difficult times during my research and for that I sincerely thank him for his confidence in me. I would also like to extend my sincere appreciation to Dr. Akira Hirose, the director of the Plasma Physics Laboratory, for his excellent support and guidance. This research would not have been possible without the technical assistance of David McColl and the Physics Machine Shop. I would also like to thank all my fellow graduate students for their constant support and friendship. Finally, I would like to extend my deepest gratitude to my family and friends. Without their love, support and understanding I could never have completed this doctoral degree.

This research was supported by the grants from the Natural Sciences and Engineering Research Council of Canada (NSERC), the Canada Research Chair (CRC) Program, and the Sylvia Fedoruk Canadian Centre for Nuclear Innovation and through the financial aid from the University of Saskatchewan.

Table of Contents

List of Tables

List of Figures

List of Abbreviations and Symbols

Abbreviation	Definition
AC	Alternating Current
ASDEX-U	Axially Symmetric Divertor Experiment Upgrade
CT	Compact Torus
CWT	Continuous Wavelet Transform
DFT	Discrete Fourier Transform
DRMP	Double Resonant Magnetic perturbation
ECE	Electron Cyclotron Emission
ECRH	Electron Cyclotron Resonance Heating
ELM	Edge Localized Mode
FB	Feedback
FFT	Fast Fourier Transform
FRMP	Fast Resonant Magnetic perturbation
H-Mode	Improved Confinement Discharge
ICRH	Ion Cyclotron Resonance Heating
IDFT	Inverse Discrete Fourier Transform
IGBT	Insulated-Gate Bipolar Transistor
ITER	International Thermonuclear Experimental Reactor
JET	Joint European Torus
L-Mode	Normal Confinement Discharge
MAST	Mega Ampère Spherical Tokamak
MHD	Magnetohydrodynamic
NBI	Neutral Beam Injection
NRMP	Non-Resonant Magnetic Perturbation
NTM	Neoclassical Tearing Mode
OH	Ohmic Heating
PA	Principal Axis
PC	Principal Component

RF	Radio Frequency
RMP	Resonant Magnetic Perturbation
RMS	Root Mean Square
RWM	Resistive Wall Mode
SCR	Semiconductor-Controlled Rectifier
SOL	Scrape-Off Layer
SRMP	Slow Resonant Magnetic Perturbation
STOR-M	Saskatchewan Torus-Modified
STOR-1M	Saskatchewan Torus-1 Modified
SV	Singular Value
SVD	Singular Value Decomposition
SXR	Soft X-Ray
TEXTOR	Tokamak Experiment for Technology Oriented Research
TH	Turbulent Heating
USCTI	University of Saskatchewan Compact Torus Injector
VE	Vertical Equilibrium

Symbol	**Definition**
a	Minor radius
A	Cross-section
B	Magnetic field
B_r	Radial magnetic field
B_z	Axial magnetic field
$B_\perp$	Vertical magnetic field
B_θ	Poloidal magnetic field
B_ϕ	Toroidal magnetic field
c	Speed of light
C	Capacitance
C_m	Fourier cosine coefficient
D	Diffusion coefficient
D	Deuterium
e	Elementary charge
e_r	Radial unit vector
e_θ	Azimuthal unit vector
E	Electric field
f	Frequency

f_b	Wavelet bandwidth frequency
f_c	Wavelet central frequency
F	Force
I	Current
I_p	Plasma current
J	Current density
J_z	Axial current density
J_θ	Azimuthal current density
l_i	Internal inductance
$\ln \Lambda$	Coulomb logarithm
L	Inductance
L_p	Plasma inductance
m	Poloidal mode number
M	Number of samples
n	Toroidal mode number
n_e	Electron density
n_i	Ion density
N	Number of turns
p	Pressure
p_e	Electron pressure
p_i	Ion pressure
P	Heating power density
q	Safety factor
r	Radial coordinate
r_L	Larmor radius
R	Major radius
R_c	Curvature radius
R_p	Plasma resistance
s	Wavelet scale
S_m	Fourier sine coefficient
t	Time
t_s	Sampling time
T_e	Electron temperature
T_i	Ion temperature
T	Tritium
v	Velocity

v_e	Electron velocity
v_i	Ion velocity
V	Voltage
V_f	Floating potential
V_l	Loop voltage
w	Island width
W	Potential energy
x	Signal
z	Axial coordinate
$\parallel$	Parallel to magnetic field direction
$\perp$	Perpendicular to magnetic field direction
∇	Gradient operator
α	Damping coefficient
β_p	Poloidal beta
γ	Adiabatic index
ΔH	Horizontal plasma position
ϵ	Inverse aspect ratio
ε	Permittivity
ζ	Damping factor
η	Resistivity
θ	Azimuthal coordinate
ι	Rotational transform
κ	collisionality coefficient
μ	Permeability
ν	Collision frequency
ξ	Arbitrary displacement
ρ	Mass density
σ	Reaction cross-section
τ	Wavelet time
τ_E	Energy confinement time
ϕ	Toroidal coordinate
Φ	Magnetic flux
ψ	Wavelet function
ω	Angular frequency
ω_0	Resonance frequency
ω_c	Cyclotron frequency

Chapter 1

Introduction

1.1 Energy Resources

Energy is an essential component to sustain life on planet earth and to advance human civilization. The quality of life and the stability of global economy in the modern world are directly correlated with the energy. The global energy consumption and the world population have been rapidly increasing in the major industrialized regions. Several reports issued by the United Nations Development Programme (UNDP) have suggested that the human development index (HDI) of various countries is closely related to the amount of per capita electricity consumption [1]. The HDI curve shown in Figure 1.1 is mostly dominated by the developing nations with low figures for the developed world. It has been estimated that the global energy demand will increase by a factor of 3 by the year 2050 [2].

Since the last century most of the energy production has been mainly based on fossil fuels. Fossil fuels are deemed to be the major source of global warming through the emission of greenhouse gases. Reserves of fossil fuels also began to deplete as the oil and gas reserves will be used up in a few tens of years, and coal reserves will last for only a few hundred years. Political and military conflicts for control of oil and gas reserves have already dominated the world energy scenario over the past few decades. Nuclear energy solutions, such as fission-based nuclear power, have been facing political and public opposition regarding some issues such as nuclear prolifera-

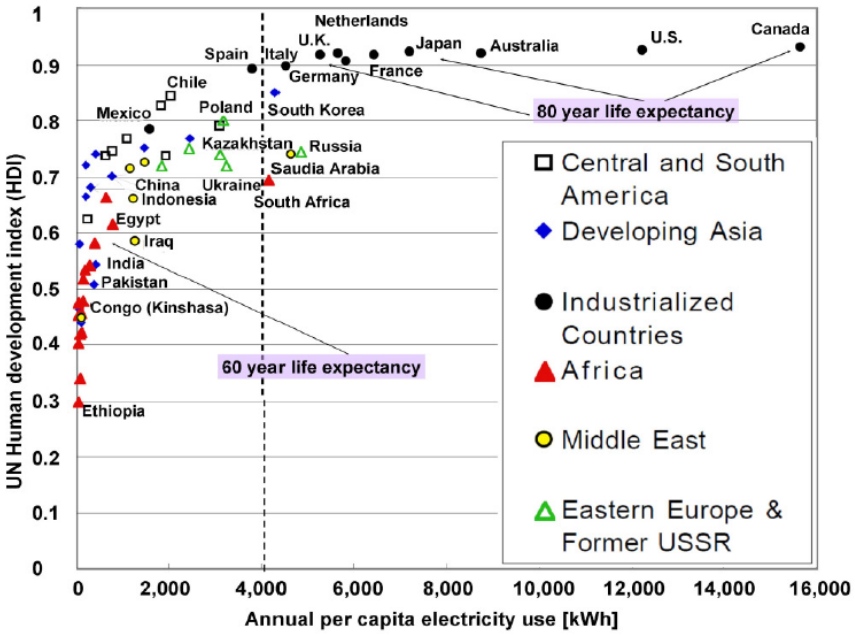

Figure 1.1: United Nations Human development index of 60 countries in 2007 plotted as a function of per capita energy use in kWh [1].

tion, radioactive fuel wastes, and potential nuclear disasters like Chernobyl and Fukushima Daiichi nuclear disasters.

The search for sustainable energy alternatives is still ongoing. The development of a new energy technology will likely take a considerable time before promoting it as a cost efficient, environmentally friendly energy source. Some clean energy resources (i.e. solar and wind power) have shown promising potential to become a reliable energy source. However, energy density, efficiency and production cost have prevented such technologies to become a major energy source especially in large urban industrial nations.

Since the proposal of nuclear fusion as a new energy alternative in the fifties of the past century, the progress of nuclear fusion research has seen many developments and advancements. Fusion power has shown a great potential maintaining the high energy demand with low pollution levels. Fusion energy also has attractive features such as the abundance of fuel, safety, and the low impact on environment. It is estimated that in the next few decades the thermonuclear power will establish itself as the primary energy supplier. However, some technical difficulties must be addressed before promoting the fusion technology for the commercial use. Therefore, the current fusion re-

search programme is aiming towards resolving these issues which requires a global effort. The international cooperation in fusion research led to the construction of the first experimental fusion reactor called the International Thermonuclear Experimental Reactor (ITER) [3].

1.2 Fusion Energy

Fusion energy is released when two light atomic nuclei are fused together to form heavier ones. The sum of two nuclei masses before the fusion reaction is larger than the sum of masses after the reaction. The difference in masses Δm, according to the relativity theory, is released by the fusion reaction as energy in form of Δmc^2, where c is the speed of light. There are many fundamental nuclear reactions that can be used as a source of fusion energy. However, the following fusion reactions are more favorable [4]:

$$\begin{aligned}
&\mathrm{D}^2 + \mathrm{D}^2 \rightarrow \mathrm{T}^3 + p + 4.0\mathrm{MeV} \\
&\mathrm{D}^2 + \mathrm{D}^2 \rightarrow \mathrm{He}^3 + n + 3.3\mathrm{MeV} \\
&\mathrm{D}^2 + \mathrm{T}^3 \rightarrow \mathrm{He}^4 + n + 17.6\mathrm{MeV} \\
&\mathrm{D}^2 + \mathrm{He}^3 \rightarrow \mathrm{He}^4 + p + 18.3\mathrm{MeV}
\end{aligned} \tag{1.1}$$

where D is deuterium, T is tritium, p is proton, He is helium and n is neutron. Due to the abundant supply of deuterium in seawater (0.015% of hydrogen in seawater $\approx 1.35 \times 10^9$ km^3), the D-D reaction seems a practical source for fusion energy. The D-T reaction, however, is easier to realize. The reason why the D-T reaction is preferred to other reactions is clearly shown in Figure 1.2. The cross-section of D-D and D-He^3 reactions are considerably less than that of the D-T reaction except at very high energies.

The probability of a fusion reaction depends on the cross-section of the target nucleus which is defined by σ. The D-T fusion reaction occurs when the D nucleus makes a successful collision with the T nucleus. The probability of such a reaction is a function of the kinetic energy of D nucleus.

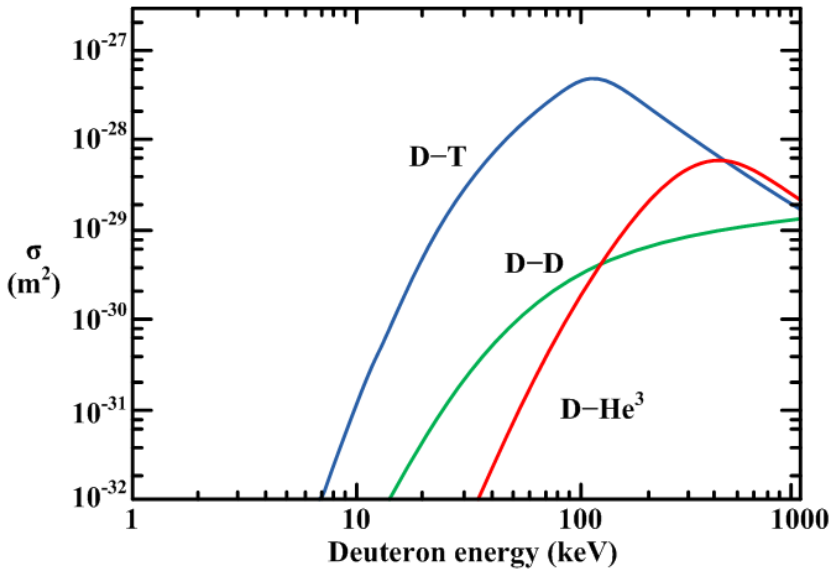

Figure 1.2: Cross-sections of different fusion reactions as a function of the kinetic energy of incident D nucleus on the target nucleus [5].

As shown in Figure 1.2, the cross-section of the D-T reaction has a maximum value of about 5×10^{-28} m^2 when the kinetic energy of the incident D is around 100 keV. When the D nucleus at a velocity of v collides with the T nuclei with a density of n_{T}, the reaction rate (number of reactions per unit time) can be expressed by $n_{\mathrm{T}}\sigma v$. It is necessary to average σv over the velocity distribution when the plasma has a Maxwellian ion temperature distribution T_i. The fitting equation of $\langle \sigma v \rangle$, in the unit of m^3/s, for a D-T reaction as a function of T_i (keV) is given by [6]:

$$\langle \sigma v \rangle = \frac{3.7 \times 10^{-18}}{\left(\frac{T_i}{37} + \frac{5.45}{3 + T_i (1 + \frac{T_i}{37.5})^{2.8}} \right) T_i^{\frac{2}{3}}} e^{\left(-\frac{20}{T_i^{\frac{1}{3}}} \right)} \tag{1.2}$$

The energy released by the fusion reactions exceeds that of the chemical reactions by millions of times. For example, the chemical reaction typically produces energy of 2.96 eV for the reaction $H_2 + \frac{1}{2}O_2 \rightarrow H_2O$. The energy released by the D-D reaction is around 3.3 MeV, which is about six orders of magnitude higher. The binding energy per nucleon is much smaller in very light nuclides compared with the binding energy of nuclides with atomic mass number around 60. For this reason, a tremendous amount of energy can be released when the light nuclei are fused.

1.3 Fusion Techniques

In order to utilize fusion for energy production, high-density fusion reactants have to be heated to a sufficiently high temperature and confined for a long time away from any surrounding materials. Fuels at such high temperatures are ionized and form a plasma. There are two main approaches for achieving fusion in the laboratory: inertial confinement and magnetic confinement. The inertial confinement works on a pulsed fashion. The fusion reactions in inertial confinement are achieved through micro-implosions of fuel pellets induced by high power laser or particle beams at a high repetition rate [7].

The magnetic confinement, on the other hand, utilizes the properties of the charged plasma particles in electromagnetic fields. The charged particles are magnetically confined away from the surrounding walls using a specific magnetic field configuration. A steady magnetic field can restrain the motion of the charged particles in a plasma across magnetic field lines. The plasma particles, however, are free to move along the field lines. The research on magnetic confinement led to a variety of confinement configuration concepts. However, the most successful approach of confining the plasma particles along the magnetic field lines has been achieved by the tokamak concept.

A tokamak is one of several magnetic confinement devices proposed for producing controlled thermonuclear fusion power. The idea of the tokamak was originally proposed by the two Russian physicists *Igor Tamm* and *Andrei Sakharov* at the Kurchatov Institute back in the 1950's [8]. The term "Tokamak" is an acronym of a Russian phrase (**To**roidal'naya **ka**mera s **ma**gnitnymi **k**atushkami) which literally means "toroidal chamber with magnetic coils". The tokamak is a torus-shaped device that uses a strong magnetic field to confine the plasma in a toroidal chamber. This simple, toroidal magnetic field alone, however, is not sufficient to establish a plasma equilibrium.

In order to achieve equilibrium in tokamaks, in which the plasma pressure is balanced by the magnetic forces, it is necessary to have a poloidal magnetic field. This field is produced by the plasma current flowing in the toroidal direction. The superposition of the toroidal field B_ϕ and the poloidal field B_θ produces magnetic field lines that move around the torus in a helical trajectory.

The toroidal field travels around the torus in circles, whereas the poloidal field travels in circles orthogonal to the toroidal field. As shown in Figure 1.3, The plasma torus is regarded as a single secondary winding of a transformer. A current flowing in the primary transformer winding induces a plasma current by transformer actions (with either iron or air core).

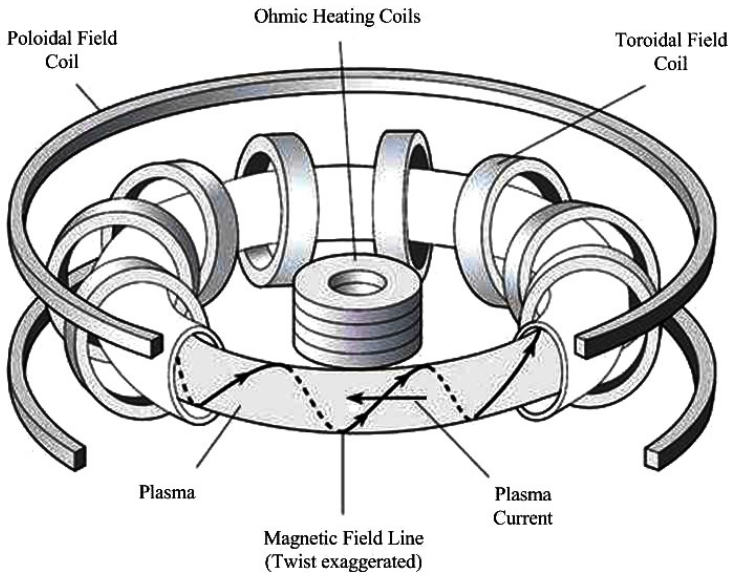

Figure 1.3: Schematic view of a tokamak device.

It was clear from early experiments that tokamak plasmas are subject to a wide range of large-scale (macroscopic) instabilities. Those instabilities limit the amount of plasma current and pressure confined by the helical magnetic field. The most active instabilities in tokamaks can be described, in a simple form, by the magnetohydrodynamic (MHD) model. Those instabilities are driven mainly by two destabilizing sources: current gradients and pressure gradients. A typical example of current and pressure-driven instabilities are the kink and the ballooning instabilities. The current-driven instabilities can be suppressed by applying a strong toroidal magnetic field. The pressure-driven instabilities (i.e. ballooning modes) can be avoided by operating the tokamak in the stable domain of the (s, α) diagram, where s is the magnetic shear parameter and α is the ballooning parameter. Nevertheless, other types of instabilities can still be excited in tokamaks [9].

The tearing modes are another class of MHD instabilities which are driven by the magnetic shear. The tearing modes tend to break magnetic flux surfaces to form helical structures known

as magnetic islands. Magnetic islands are radially localized magnetic structures developed on so-called rational flux surfaces [10]. The destabilizing effects of tearing modes on the plasma may result in minor and major disruptions. The minor disruptions destabilize the plasma and degrade the particle and energy confinement. The major disruptions, however, are more severe since they can end a plasma discharge [11].

The tearing modes grow on resonant magnetic surfaces with rational values of the safety factor q. The fluctuations associated with the tearing mode instabilities in tokamaks, such as Mirnov oscillations [12] and sawtooth oscillations [13], are usually monitored and analyzed by various diagnostics and data processing techniques. Mirnov and sawtooth oscillations do not significantly affect the operation of the tokamak, hence can be observed during the normal operation. The fluctuating signals of Mirnov and sawtooth oscillations are characterized by temporal evolutions and spatial structures expressed by the poloidal and toroidal mode numbers (m, n).

It is believed that Mirnov oscillations are generally caused by the rotation of nonlinearly saturated magnetic islands formed by the tearing modes. The rotation of magnetic islands causes oscillating helical perturbations in the poloidal magnetic fields (B_θ) which can be detected at the edge of plasma using magnetic probes called Mirnov coils [14]. The soft x-ray (SXR) radiation emitted from the plasma can be observed by SXR photodiodes typically installed inside tokamaks. The radiation intensity of SXR depends on the electron temperature, density and on the impurity concentration in the plasma. The SXR radiation is mainly produced by the impurity spectral lines and bremsstrahlung radiation [15]. There are two typical SXR signals observed in tokamaks: helical oscillations correlated with Mirnov oscillations and sawtooth oscillations. The sawtooth oscillations are best observed when the amplitudes of Mirnov oscillations are small.

It has been reported in many tokamaks that the major disruptions are likely caused by the interaction of (2, 1) magnetic islands with the limiter or with the cold plasma surroundings [16]. Other theories suggested that the major disruptions are triggered by coupling of a growing (2, 1) island with (1, 1) mode [17] or with (3, 2) mode [18]. Since most of the major disruptions are related to (2, 1) islands, the growth of (2 ,1) mode was expected to be either postponed or activated

by means of ($l = 2, n = 1$) helical coils [19]. The resonant magnetic perturbations (RMP) generated by the coils can strongly influence the magnetic islands on the $q = 2$ resonant surface in tokamaks, leading to more stable plasma discharges especially when the coils are fed with small DC currents (typically 1-4$\%$ of the total plasma current). RMP can effectively reduce the width of magnetic islands and hence suppress the Mirnov oscillations [20].

1.4 Resonant Magnetic Perturbations

It has been known that major disruptions impose serious limitations on the normal operation of tokamaks. Different procedures and techniques have already been proposed to avoid disruptions [21]. One of the proposed techniques is influencing the tokamak plasmas with radial magnetic fields called resonant magnetic perturbations (RMP) produced by external helical coils with low m and n winding values. The produced RMP counteracts magnetic islands of the same helicity. On one hand, the application of moderate RMP showed that Mirnov oscillations could be strongly suppressed and the onset of the disruptive instability could be delayed. On the other hand, the external helical coils have been used to study the nature of major disruptions since the disruptions can be artificially triggered if the coils are fed with substantially higher RMP current (I_{RMP}).

The first study with RMP was carried out in the Pulsator tokamak [22], which showed that the occurrence of major disruptions can be controlled by means of external helical windings. The early RMP experiments have been performed with a variety of coils, either complete or local sets mainly to study the interaction between RMP and MHD modes. Most of the early experiments have been conducted with an (2, 1) windings, such as in Pulsator [22], ATC [23], TO-1 [24], HT-6B [25], TBR-1 [26], Tokoloshe [27] and DITE [28] tokamaks. The resonant coils have also been used to interact with (1, 1) [29], (3, 2) [30], (4, 2) [31], (3, 1) [32] and (4, 1) [33] islands.

Alternating current (AC) coils with a mode-locking feedback system have been used in several early tokamaks (e.g. ATC [23], DITE [28] and TO-1 [34] tokamaks), and more recently in TEXTOR [35] and J-TEXT [36] tokamaks. The suppression of (2, 1) tearing modes, resulted from the

phase locking between the coils and tearing modes, has been clearly demonstrated in those machines. Reduction in MHD frequency and improvement in energy and particle confinement times have been observed as well. In the earlier experiments with DC RMP currents (i.e. TOSCA [37] and TORIUT-4 [38] tokamaks), a regime of suppressed Mirnov signals has been observed, which delayed the precursor of the disruptive instability. Other observations include sawtooth modulations and changes in particle and energy confinement times. However, as mentioned earlier, the disruptive instabilities can be precipitated by applying relatively high helical coil currents. The most harmful characteristics of disruptive instabilities are energy dissipation, the complete loss of plasma confinement, and the induced forces on the tokamak structure [39]. The hypothesis that disruptive instabilities are caused by a (2, 1) island interacting with another structure (island or limiter) inside the plasma has been supported by many experimental evidences. Disruptive instabilities can also be triggered by radiation losses, magnetic field line ergodization, multifaceted asymmetric radiation from the edges (MARFES) and microturbulence [40].

The first successful attempt to influence a tokamak plasma by a local, external resonant helical field was carried out in the Pulsator tokamak (major radius $R = 70$ cm, minor radius $a = 14$ cm, toroidal magnetic field $B_\phi = 2.7$ T and plasma current $I_p = 125$ kA) [41]. Pulsator is equipped with a set of (2, 1) windings. The main purpose of this set was to achieve equilibrium for a current-less pre-ionization plasma which could improve the startup schemes in tokamaks. However, this purpose was never realized, instead the helical windings have been proven to be a very effective tool for the investigation of disruptive instabilities. It has been found that if the tokamak magnetic field and the superimposed RMP have the same helicity, a disruption in plasma current can be stimulated by a well-producible value of I_{RMP}. On the other hand, at lower helical currents, a drastic reduction in the $m = 2$ mode amplitude has been observed, which led to longer plasma pulses even with high density.

The stabilization of the $m = 2$ tearing mode was explained by the local flatness of the temperature and current density profiles at the resonant surfaces. When the particles move along the field lines of the island, they connect the inner and outer regions after a few toroidal rotations, which

enhances the radial transport process of energy and particles. It has also been observed that the width of magnetic island increases with I_{RMP}. It is believed that when the island edge approaches the limiter, an effective magnetic limiter is formed due to the energy and particles transfer from the island to the limiter. Furthermore, more pronounced ergodization of field lines was created by helical currents antiparallel to the plasma current, resulting in smaller critical values of I_{RMP}.

The previous works have reported different explanations for the suppression of Mirnov oscillations observed during RMP. It was not clear whether the observed suppression of Mirnov signals was due to mode suppression, to a change in mode rotation, or to a combination of both effects. A systematic study conducted in COMPASS-C [42] has shown that in low q and low density plasmas the Mirnov oscillations can be drastically suppressed as a result of mode stabilization. The mode stabilization occurs when the rotating frequency of magnetic islands is reduced during application of RMP. It has been found that the reduction of mode frequency correlates with the reduction of mode amplitude rather than with the RMP amplitude. The earlier belief that the reduction in mode frequency is associated with the mode locking has been argued by the fact that the locked modes, in the JET tokamak for example [43], are often followed by a plasma current degradation and high-current disruptions, which is not the case for RMP if it is properly applied [44]. However, since locked modes can occur without causing disruptions [45], a better argument can be made in terms of the amplitude and frequency behaviour of locked modes [46]. In general, the suppression of Mirnov oscillation signals ($\dot{B}$) may be attributed to the reduction of mode magnitude and/or the reduction in frequency.

It should also be noted that the applied helical current (I_{RMP}) has a critical limit. Exceeding this threshold results in a plasma disruption. The reported disruption has no characteristic differences to that caused by natural disruptive instabilities. The disruptive instabilities are usually preceded by the growth of $m = 2$ mode to a large amplitude. The disruption is often characterized by negative spikes in the loop voltage, sudden loss in particle and energy confinement, and unpredictable expansion in the plasma minor radius. The disruptive instabilities can terminate the plasma discharge and damage the walls. However, these instabilities can be avoided by optimizing the operating

parameters, such as q-value and plasma density profile [47].

RMP has also been used for error field correction [48]. In theory, the configuration of magnetic fields in tokamaks is ideally axisymmetric. However, the presence of eddy currents and the imperfection of manufacturing and assembling the coil systems in tokamaks cause asymmetries in magnetic fields called error fields. A small deviation in the magnetic field symmetry with amplitude as low as $B_r/B_\phi \sim 10^{-4}$ (where B_r is the radial magnetic field and B_ϕ is the toroidal magnetic field) can create mode locking in large tokamaks such as ITER [49]. The error field correction with RMP has been carried out in many tokamaks such as COMPASS-D [50], DIII-D [51] and JET [52] tokamaks. It has been found that the direct compensation for error fields in tokamaks is rather complicated since the magnetic structure of error fields contains a wide range of harmonics (m, n). Most of the correction systems in tokamaks are designed to compensate for error fields with different harmonic numbers. It has been found that harmonics with odd n numbers are usually dominant, particularly the $n = 1$ harmonic [53].

One of the common applications of RMP is the active control of the so-called edge localized modes (ELMs). ELMs are a type of non-disruptive MHD instability occurring at the edge of a tokamak plasma during the improved confinement phase (H-mode) [54]. The first successful attempt to mitigate ELMs by RMP was conducted in the DIII-D tokamak [55]. RMP coil systems have been widely implemented in many tokamaks, such as JET [56], ASDEX-U [57] and MAST [58], to control ELMs during the H-mode operation. It is believed that the peeling-ballooning modes are responsible for ELMs formation [59]. When RMP fields are applied near the plasma edge they form a stochastic magnetic field layer, causing an enhancement in the local radial transport [60]. During the ELMs mitigation the pedestal pressure gradient is reduced below the stability limit of peeling-ballooning modes. It has been observed during ELMs suppression phase that the pedestal temperature increases and the reduction in the pedestal pressure gradient is mainly caused by a phenomenon called the density pump-out effect [61]. The density pump-out effect does not always occur during ELMs mitigation. For example, it has been observed in the TEXTOR tokamak that in some discharge scenarios the electron density is increased due to the increase of electric field

shear ($\mathbf{E} \times \mathbf{B}$) [62]. The density pump-out effect can also be observed during the normal confinement phase (L-mode) if there is a good alignment between RMP and the pitch of equilibrium magnetic field lines which would maximize the size of the resonant components of the applied perturbation [63].

The RMP fields have been successfully utilized to control plasma rotation in tokamaks. Previous experiments have shown that tokamak plasmas can be confined and stabilized by plasma rotation. The efficiency and the performance of tokamaks can be enhanced by understanding the mechanism of plasma rotation and maintaining the optimal rotation profile. Plasma rotation also has stabilizing effects on edge plasma turbulence and MHD instabilities, most notably the resistive wall modes (RWM) [64] and the neoclassical tearing modes (NTM) [65]. The $\mathbf{E} \times \mathbf{B}$ shear resulting from the interaction between plasma rotation and the radial electric fields affects the turbulent transport in tokamaks [66]. It has been demonstrated in many tokamaks that both resonant [67–69] and non-resonant (NRMP) [70–72] configurations of RMP modify the rotation profile and the $\mathbf{E} \times \mathbf{B}$ shear. It has been reported that RMP fields induce either electromagnetic (EM) torque in the resonant configuration [73], or neoclassical toroidal viscosity (NTV) torque in the non-resonant configuration [74]. The NTV torque is generated by a nonambipolar radial particle flux caused by the breaking of the toroidal magnetic symmetry in low collisionality plasmas [75]. Plasma rotation also reduces the error field penetration depth which can enhance the error field tolerance in tokamaks [76].

RMP has been implemented in other important applications in tokamaks such as modifying the edge transport [77–79] and suppressing the runaway electrons [80–82]. RMP fields are also used to study the linear and nonlinear plasma response to external magnetic fields in tokamaks both in experiment [83–85] and theory [86–88]. The plasma response to RMP was measured in the TEXTOR tokamak using an internal magnetic probe array inserted from the low-field side on TEXTOR [89]. The magnetic array measures the radial, poloidal and toroidal components of the local magnetic field inside the plasma. The local magnetic field contribution comes from both vacuum field and plasma response field. The pure plasma response to RMP can be obtained by

subtracting the vacuum magnetic field from the local magnetic field. The local measurements of magnetic field provides a better understanding of the local interaction between RMP and the tokamak plasma as well as the role of plasma flow rotation in RMP penetration and screening [90–94].

The implementation of the ion Doppler spectroscopy (IDS) systems in many tokamak devices allowed the non-intrusive measurements of plasma flow velocity of different ion impurities [95–97]. The IDS system is a novel approach to detect Doppler broadening and shifting of ion spectral lines in tokamak plasmas. The IDS system can be used to estimate the ion temperature and the flow velocity at different radial locations. The IDS measurements depend mainly on the line radiation of impurity ions rather than the primary plasma ions. The temperature and the flow velocity of main plasma ions have to be approximated from the IDS measurements. A new IDS system has been installed in the Saskatchewan Torus-Modified (STOR-M) tokamak to measure the toroidal flow velocity of impurity ions [98]. The toroidal flow velocities measured in STOR-M are obtained mostly from C_{III}, O_V and C_{VI} line emissions. The toroidal plasma flow has been examined in STOR-M during RMP with different magnitudes and configurations [99].

Within the framework of this Ph.D. research, the emphasis is to actively control the MHD instabilities by RMP. The RMP field in STOR-M is generated by an ($l = 2$, $n = 1$) helical coil powered by a set of capacitor banks and gated by an insulated-gate bipolar transistor (IGBT) switch. Additional capacitor bank was also added to the existing power supply of RMP coil system. A separate charging circuit, trigger circuit and semiconductor-controlled rectifier (SCR) switch were designed and built for the new RMP bank. The additional capacitor bank provides a sharp current pulse, similar to the turbulent heating (TH) current pulse [100]. The sharp RMP pulse is typically fired during the current flat-top phase of RMP pulse to study the RMP penetration. The flat RMP pulse presets the rotation speed of plasma flow and the superimposed sharp RMP pulse is used to study the radial penetration/attenuation of the magnetic field at that rotation speed.

The magnetic fluctuations associated with MHD modes are monitored in STOR-M by a set of discrete Mirnov coils placed at various poloidal and toroidal locations. The Mirnov arrays are com-

plemented with an SXR detection system and electrostatic probe arrays to measure density, temperature and potential fluctuations in the STOR-M tokamak. An internal magnetic probe array was assembled and installed on STOR-M to study the RMP penetration and the plasma response to the RMP fields. The valuable information regarding MHD instabilities are retrieved by using various signal processing techniques. The time-resolved frequency analysis of transient and non-stationary fluctuating MHD signals is performed by the Morlet wavelet function [101]. The harmonic MHD analysis is carried out using the spatial Fourier series [102] and the singular value decomposition algorithm [103].

1.5 Thesis Motivations and Objectives

The primary goal of this thesis is to implement RMP technique in the STOR-M tokamak and to study its effects on MHD instabilities, toroidal plasma flow, and plasma properties in the edge and the scrape-off layer (SOL) regions. An array of internal magnetic probes is also used to investigate the features of RMP penetration and plasma response in STOR-M. The main objectives and motivations of this thesis work are outlined below:

1. Winding two sets of ($l = 2, n = 1$) helical windings poloidally separated by 90° and installed outside the vacuum chamber of STOR-M.

2. Constructing an RMP power supply consisting of two capacitor banks and IGBT switch to generate a slow RMP (SRMP) pulse.

3. Building an additional capacitor bank gated by SCR to produce a fast RMP (FRMP) pulse superimposed on the SRMP pulse.

4. Designing, fabricating and calibrating a movable internal magnetic probe array comprised of 4 poloidal magnetic probes which are radially separated by 1 cm.

5. Investigating the influence of SRMP on MHD instabilities using Mirnov coil arrays and SXR camera system.

6. Studying the effects of SRMP on the toroidal plasma flow and edge/SOL plasma parameters using the IDS system and a rake array of Langmuir probes.

7. Employing the internal probe array and the FRMP pulse to study the plasma response and RMP penetration in STOR-M.

1.6 Thesis Outline

Chapter 1 was an introduction to the global energy consumption, fusion energy and the common fusion approaches used in the fusion energy research. A literature review of the history of RMP as well as its current applications in tokamaks was also highlighted in this chapter.

The basics of magnetic confinement, plasma equilibrium and heating methods in tokamaks are briefly explained in Chapter 2. An overview of STOR-M tokamak and related diagnostics is also presented.

Chapter 3 covers the fundamentals of MHD instabilities, magnetic islands, plasma rotation and transport in tokamaks. This chapter also explains the mathematical background of numerical techniques used for data analysis.

The apparatus of RMP system is described in Chapter 4. The diagnostics used in RMP experiments such as the Mirnov coil arrays, the SXR cameras, the IDS system, the rake probe and the internal probe array are discussed as well.

Chapter 5 highlights the main results of RMP experiments. The effects of RMP pulse on magnetic islands, toroidal plasma flow and other plasma parameters are studied in STOR-M. The plasma response and the RMP penetration are also examined using the internal probe array.

Chapter 6 summarizes the major results of this work and provides suggestions for future research.

Chapter 2

Tokamak

2.1 Introduction

The tokamak is a fusion research device that utilizes the concept of magnetic confinement to confine hot plasmas. The tokamak plasmas are generated by several heating techniques including the ohmic heating, the neutral beam injection and the radio frequency heating. The charged particles in the plasma (i.e. electrons and ions) are subject to guiding center drifts that deteriorate the plasma confinement in a simple toroidal field configuration. These particle drifts can be neutralized by a helical magnetic field formed by a combination of external toroidal field and poloidal field induced by the plasma itself. The fundamentals of magnetic confinement, plasma equilibrium and heating are discussed in this chapter. An overview of the main components and diagnostics in the STOR-M tokamak is also presented.

2.2 Magnetic Confinement

Plasmas are confined in tokamaks by a combination of toroidal magnetic field B_ϕ generated by external coils and poloidal magnetic field B_θ induced by the plasma current flowing in the toroidal direction. A single-particle model is often used to explain how a tokamak works. As shown in Figure 2.1, when a current flows in the primary transformer windings, it induces a toroidal plasma

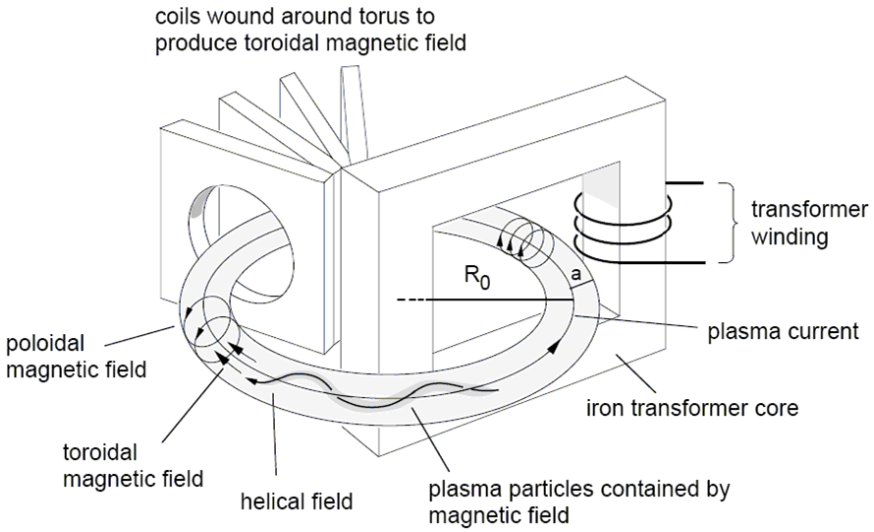

Figure 2.1: Coil system and magnetic fields in tokamak. The transformer winding acts as a primary winding of a transformer and the plasma current is regarded as a one-turn secondary winding.

current by transformer actions. The motion of plasma particles in a magnetic field B is determined by the Lorentz force [104]:

$$m\frac{d\mathbf{v}}{dt} = q(\mathbf{v} \times \mathbf{B}) \tag{2.1}$$

where q and m are the particle charge and mass, respectively. For a straight, uniform magnetic field B generated by a helical current, plasma species (i.e. electrons and ions) move along the magnetic field lines in a spiral motion, depending on the initial velocity of particles. The helical motion of particles is characterized by the cyclotron frequency ω_c [105]:

$$\omega_c = \frac{|q|B}{m} \tag{2.2}$$

The radius of gyration of particles about their guiding centers is defined by the Larmor radius:

$$r_L = \frac{v_\perp}{\omega_c} = \frac{mv_\perp}{|q|B} \tag{2.3}$$

where $v_\perp$ is the velocity component of the particle in the plane perpendicular to the magnetic field. The motion of particles perpendicular to the magnetic field lines is bound within the Larmor radius. The particles, however, are free to move along the field lines. Although the toroidal magnetic field

provides the main confinement of the plasma in tokamaks, bending the straight magnetic field lines to close on themselves and to form a torus is not sufficient to confine the plasma. The toroidal magnetic field in tokamaks is stronger at smaller radii and weaker at larger radii, causing different types of particle drifts.

The orbital radius of particles, according to Equation 2.3, is determined by the strength of the magnetic field. The particles rotate at smaller major radial locations with stronger B have narrower orbits than those at larger major radial locations. The particles in this simple toroidal configuration are subject to two types of particle drifts [106], the curvature drift

$$\mathbf{v}_R = \frac{mv_\parallel^2}{qB^2}\frac{\mathbf{R}_c \times \mathbf{B}}{R_c^2} \tag{2.4}$$

and the gradient (or grad-B) drift:

$$\mathbf{v}_{\nabla B} = \pm\frac{1}{2}v_\perp r_L \frac{\mathbf{B} \times \nabla B}{B^2} \tag{2.5}$$

where R_c is the radius of magnetic field curvature, $v_\parallel$ and $v_\perp$ are the parallel and the perpendicular components of the particle velocity relative to the magnetic field. The direction of curvature and gradient drifts is determined by the sign of the particle charge. As shown in Figure 2.2, the electrons and ions move in opposite vertical directions, creating a charge separation. The charge separation between the plasma species induces a vertical electric field which causes another type of drift called the $\mathbf{E} \times \mathbf{B}$ drift:

$$\mathbf{v}_{\mathbf{E}\times\mathbf{B}} = \frac{\mathbf{E} \times \mathbf{B}}{B^2} \tag{2.6}$$

In a pure toroidal configuration, the $\mathbf{E} \times \mathbf{B}$ drift degrades the plasma confinement as it causes the particles to drift towards the outer wall. The concept to confine charged particles in tokamaks is to superimpose an additional poloidal magnetic field B_θ on the toroidal magnetic field B_ϕ. The poloidal field in tokamaks is induced by the toroidal plasma current. The combination of the toroidal and poloidal fields results in a magnetic field with closed, helical magnetic field lines. This

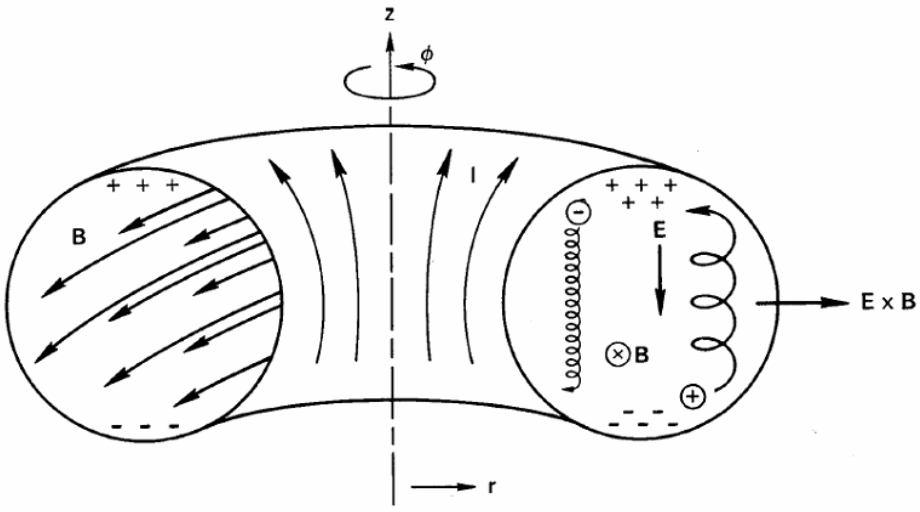

Figure 2.2: Particle drifts in a simple toroidal magnetic field [106].

helical magnetic field can neutralize the charge separation; this is because the electrons and ions spiral along the helical magnetic field lines. The motion of electrons and ions along the toroidal direction will eventually move them to the bottom (top) and neutralize the charge separation caused by the curvature and grad-B drifts. This concept is called the rotational transform and it is essential in any toroidal magnetic confinement device.

2.3 Plasma Equilibrium

Tokamak plasmas are subject to two kinds of equilibria. Firstly there is the internal balance between the pressure gradient of plasma and the forces due to the magnetic field. Secondly there is an equilibrium between the expansion forces acting on the plasma and the Lorentz force induced by an external vertical magnetic field. A single-fluid model is often used to analyze the plasma equilibrium. The force balance equation between the pressure and the magnetic forces in plasma is given by [107]:

$$\nabla p = \mathbf{J} \times \mathbf{B} \tag{2.7}$$

where $p = nT$ is the plasma pressure which may be assumed to be isotropic in tokamaks. Substituting Ampère's law

$$\nabla \times \mathbf{B} = \mu_0 \mathbf{J} \tag{2.8}$$

into the force balance equation (Equation 2.7) yields:

$$\nabla p = \frac{1}{\mu_0} (\nabla \times \mathbf{B}) \times \mathbf{B} \tag{2.9}$$

The above equation can be reduced to:

$$\nabla p = \frac{1}{\mu_0} \left[(\mathbf{B} \cdot \nabla)\mathbf{B} - \nabla \left(\frac{B^2}{2} \right) \right] \tag{2.10}$$

where the vector identity

$$\nabla(\mathbf{A} \cdot \mathbf{B}) = \mathbf{A} \times (\nabla \times \mathbf{B}) + \mathbf{B} \times (\nabla \times \mathbf{A}) + (\mathbf{B} \cdot \nabla)\mathbf{A} + (\mathbf{A} \cdot \nabla)\mathbf{B} \tag{2.11}$$

has been used. Equation 2.10 can be rearranged as:

$$\nabla \left(p + \frac{B^2}{2\mu_0} \right) = \frac{1}{\mu_0} (\mathbf{B} \cdot \nabla)\mathbf{B} \tag{2.12}$$

The above equation is called the pressure balance equation which is a nonlinear differential equation for $\mathbf{B}$. It can be solved for $\mathbf{B}$ subject to the constraint $\nabla \cdot \mathbf{B} = 0$. When rewritten in terms of the poloidal magnetic flux function, the pressure balance equation reduces to the Grad-Shafranov equation. The gradients of the plasma pressure p and the magnetic pressure $\frac{B^2}{2\mu_0}$ on the left hand side are counterbalanced by the curvature term $(\mathbf{B} \cdot \nabla)\mathbf{B}$ which comes from bending the magnetic field lines.

Figure 2.3 shows an example of equilibrium in a cylindrical plasma column of radius a with cylindrical coordinates (r, θ, z). The equilibrium is treated by assuming axial symmetry. The axial plasma current has a current density distribution $J_z(r)$. The axial current $J_z(r)$ generates an

azimuthal magnetic field $B_\theta(r)$. The combination of $B_\theta(r)$ and the magnetic field $B_z(r)$ (directed along the axis of the cylinder) is a helical magnetic field $\mathbf{B} = \mathbf{B}_\theta + \mathbf{B}_z$. The radial component of the pressure balance equation (Equation 2.12) is given by [108]:

$$\frac{\partial}{\partial r}\left(p + \frac{B_\theta^2}{2\mu_0} + \frac{B_z^2}{2\mu_0}\right) = -\frac{1}{\mu_0}\frac{B_\theta^2}{r} \tag{2.13}$$

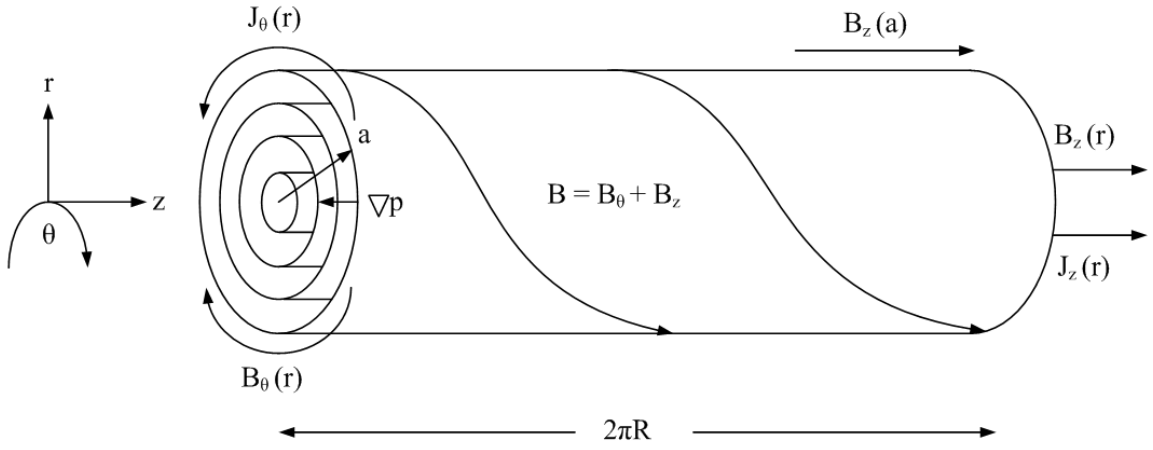

Figure 2.3: Equilibrium in a cylindrical plasma column.

The axial field B_z is omitted because it is assumed to be straight and the curvature term acts only in the azimuthal direction (θ):

$$(\mathbf{B}\cdot\nabla\mathbf{B})_r = \frac{B_\theta}{r}\frac{\partial}{\partial\theta}\left(B_\theta \mathbf{e}_\theta\right) = -\frac{B_\theta^2}{r}\mathbf{e}_r \tag{2.14}$$

where the vector identity

$$\frac{\partial \mathbf{e}_\theta}{\partial\theta} = -\mathbf{e}_r \tag{2.15}$$

has been substituted in Equation 2.14. The radial balance equation (Equation 2.13) can be written as:

$$\frac{\partial}{\partial r}\left(p + \frac{B_z^2}{2\mu_0}\right) = -\frac{1}{2\mu_0}\frac{1}{r^2}\frac{\partial}{\partial r}(rB_\theta)^2 \tag{2.16}$$

Further manipulation yields:

$$\frac{\partial p}{\partial r} = J_\theta B_z - J_z B_\theta = -\frac{1}{\mu_0}\frac{\partial}{\partial r}\frac{B_z^2}{2} - \frac{1}{\mu_0}\frac{B_\theta}{r}\frac{\partial}{\partial r} r B_\theta \tag{2.17}$$

Multiplying the above equation by r^2 and integrating over the plasma cross-section provide the equilibrium condition for the cylindrical plasma:

$$\langle p \rangle = \frac{1}{2\mu_0}\left[B_\theta^2(a) + B_z^2(a) - \langle B_z^2 \rangle\right] \tag{2.18}$$

where $\langle p \rangle$ and $\langle B_z^2 \rangle$ are the averages across the plasma cross-section:

$$\langle p \rangle = \frac{2\pi}{\pi a^2}\int_0^a p(r) r dr \tag{2.19}$$

$$\langle B_z^2 \rangle = \frac{2\pi}{\pi a^2}\int_0^a B_z^2(r) r dr \tag{2.20}$$

Equation 2.18 describes the force balance condition in the minor radius direction. It remains valid even when the straight discharge is weakly bent into a torus as in tokamaks. The toroidal magnetic field in tokamaks is much larger than the poloidal field ($B_\phi \gg B_\theta$). More importantly, since the tokamak is characterized by a curvature radius R, an equilibrium condition in the major radius direction is required to maintain the balance with the expansion forces acting in that direction.

The plasma confined in a toroidal chamber has a natural tendency to expand outward in the radial direction to increase its inductance [109]:

$$L = \mu_0 R\left[\ln\left(\frac{8R}{a}\right) - 2 + \frac{l_i}{2}\right] \tag{2.21}$$

where μ_0 is the vacuum permeability, R is the major radius of the plasma and a is the minor radius. The parameter l_i is the internal inductance parameter defined for a plasma cylinder by:

$$l_i = \frac{\langle B_\theta^2 \rangle}{B_\theta^2(a)} = \frac{2\pi\int_0^a B_\theta^2(r) r dr}{\pi a^2 B_\theta^2(a)} \tag{2.22}$$

The above expression for l_i is also valid for large aspect ratio tokamaks ($\epsilon = \frac{a}{R} \ll 1$, where ϵ is the inverse aspect ratio). The internal inductance parameter l_i has known values depending on the radial profile of toroidal current density J_ϕ. As shown in Figure 2.4, the internal inductance l_i ranges from zero for a skin current, $l_i = \frac{1}{2}$ for a uniform toroidal current, to greater than $\frac{1}{2}$ for a centrally peaked current distribution.

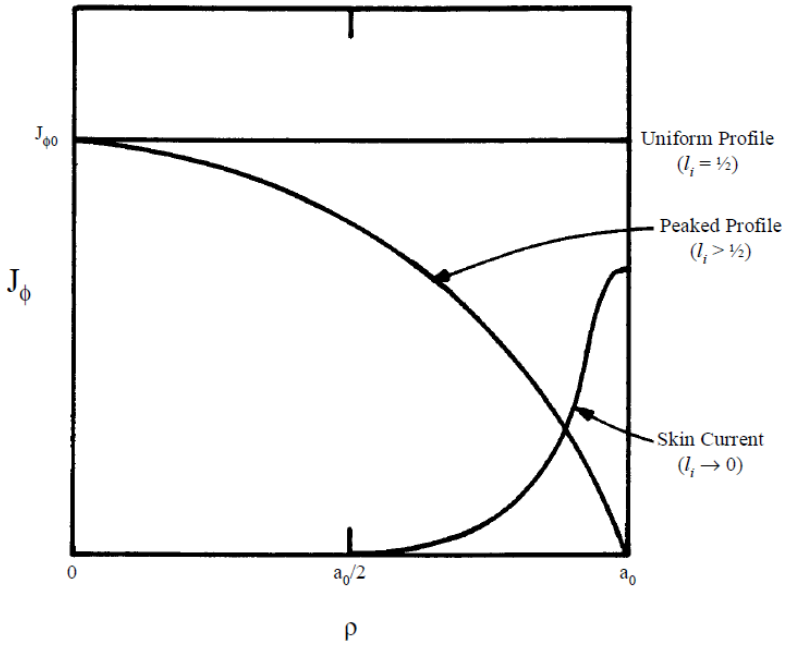

Figure 2.4: Dependence of the internal inductance l_i on the radial distribution of toroidal plasma current density [110].

The magnetic energy associated with the self-inductance of plasma induces a radially expanding force given by:

$$\begin{aligned} F_1 &= \frac{\partial}{\partial R}\left(\frac{1}{2}LI_p^2\right) \\ &= \frac{1}{2}\mu_0 I_p^2\left[\ln\left(\frac{8R}{a}\right) - 1 + \frac{l_i}{2}\right] \end{aligned} \tag{2.23}$$

The ballooning force also exerts an outward radial force on the plasma:

$$F_2 = \frac{\partial}{\partial R}\left(2\pi^2 R a^2 \langle p\rangle\right) = 2\pi^2 a^2 \langle p\rangle \tag{2.24}$$

where $\langle p \rangle$ is the average plasma pressure defined by Equation 2.19. The radial force due to the change in the toroidal magnetic field is:

$$F_3 = -2\pi^2 a^2 \frac{1}{2\mu_0} \left[\langle B_\phi^2 \rangle - B_\phi^2 \right] \tag{2.25}$$

where $\langle B_\phi^2 \rangle$ is the toroidal magnetic field averaged over the plasma cross-section:

$$\langle B_\phi^2 \rangle = \frac{2\pi}{\pi a^2} \int_0^a B_\phi^2(r) r dr \tag{2.26}$$

Recalling the force balance equation (Equation 2.18) in the toroidal coordinate system (r, θ, ϕ) yields:

$$\frac{1}{2\mu_0} \left[\langle B_\phi^2 \rangle - B_\phi^2 \right] = \frac{1}{2\mu_0} B_\theta^2(a) - \langle p \rangle \tag{2.27}$$

The left hand side term can be simplified to:

$$\frac{1}{2\mu_0} \left[\langle B_\phi^2 \rangle - B_\phi^2 \right] = \frac{B_\theta^2(a)}{2\mu_0} (1 - \beta_p) \tag{2.28}$$

where

$$\beta_p = \frac{\langle p \rangle}{B_\theta^2(a)/2\mu_0} \tag{2.29}$$

is the poloidal beta. The total expansion force F_R acting on the tokamak plasma in the major radial direction is given by:

$$F_R = \frac{\mu_0 I_p^2}{2} \left[\ln\left(\frac{8R}{a}\right) + \beta_p + \frac{l_i}{2} - \frac{3}{2} \right] \tag{2.30}$$

As shown in Figure 2.5, the radial force F_R can be counterbalanced by applying an additional magnetic field $B_\perp$. The vertical magnetic field induces a radially inward Lorentz force, so that $F_L = F_R = 2\pi R I_p B_\perp$, where F_L is the Lorentz force. The required vertical field is expressed by:

$$B_\perp = \frac{F_R}{2\pi R I_p} = \frac{\mu_0 I_p}{4\pi R} \left[\ln\left(\frac{8R}{a}\right) + \beta_p + \frac{l_i}{2} - \frac{3}{2} \right] \tag{2.31}$$

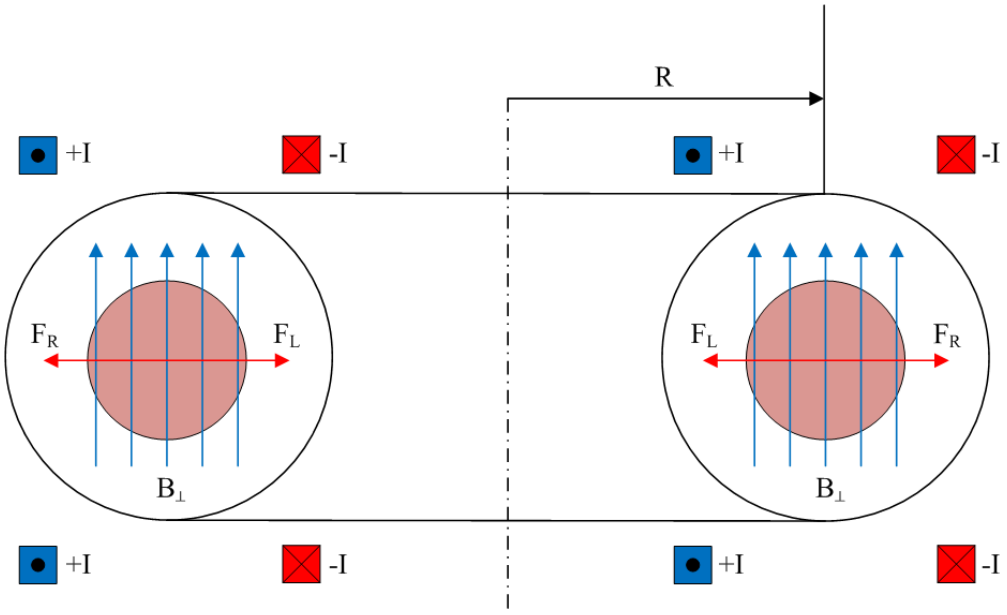

Figure 2.5: Tokamak equilibrium in the major radius direction. The outward expanding force F_R is counterbalanced by the inward Lorentz force F_L induced by the vertical magnetic field $B_\perp$.

As the plasma pressure and current density distribution vary, the vertical field should accordingly be adjusted to maintain the plasma discharge at a desired position. In modern tokamaks (including STOR-M), the majority of vertical field is provided by a pre-programmed field which is roughly proportional to the plasma current. The vertical feedback field based on the measured plasma horizontal position ΔH provides the remaining vertical field.

2.4 Plasma Heating

The tokamak plasmas require substantial heating to reach relevant fusion temperatures ($\sim$ 20keV). Tokamak plasmas are initially formed by the ohmic heating which is also used for the current ramp-up and quasi-steady current phase. The ohmic heating exploits the finite resistivity in a plasma caused by the electron-ion collisions. The ohmic heating density is given by [111]:

$$P_\Omega = \eta J^2 \tag{2.32}$$

where η is the resistivity of the plasma and J is the current density. At low temperatures the ohmic heating is very effective. However, according to the Spitzer resistivity, the ohmic heating becomes ineffective since the resistivity rapidly decreases when the electron temperature (T_e) increases. The Spitzer resistivity based on Coulomb scattering is given by [112]:

$$\eta = 1.65 \times 10^{-9} \frac{Z_{\text{eff}} \ln \Lambda}{T_e^{\frac{3}{2}}} \tag{2.33}$$

where T_e is the electron temperature in keV, Z_{eff} is the effective ion charge number (≈ 1.5), and $\ln \Lambda$ is the Coulomb logarithm calculated from:

$$\ln \Lambda = \ln \left(12\pi n_e \left(\frac{\varepsilon_0 T_e}{n_e e^2} \right)^{3/2} \right) \tag{2.34}$$

which is insensitive to plasma density and temperature. For a typical STOR-M discharge ($n_e \simeq 5 \times 10^{18}$ m^{-3}, $T_e \simeq 200$ eV), $\ln \Lambda$ is around 17. The ohmic heating can achieve a maximum electron temperature of a few keV due to the anomalously short energy confinement times in tokamaks. However, since the energy confinement scales with the tokamak size, it is expected for future tokamaks to attain higher temperature plasmas by ohmic heating alone. Implementing ohmic heating at high temperatures also requires high magnetic field. The modern tokamaks use other supplementary heating methods to increase the plasma temperatures to ignition temperatures.

The two main auxiliary methods used for plasma heating in tokamaks are the neutral beam injection (NBI) and the radio frequency (RF) heating. These heating techniques have been successfully used to heat the plasma to the temperature required for fusion. They have also shown significant degradation in the energy confinement time as the injected power increased. The energy confinement time (τ_E) has a strong dependence on the heating power [113]:

$$\tau_E \propto \frac{1}{\sqrt{P}} \tag{2.35}$$

where P is the auxiliary heating power. The energy confinement is determined mainly by turbulent

processes in plasmas, which are significantly influenced by the heating processes themselves.

NBI is one of the auxiliary heating methods used in tokamaks [114]. It involves injecting high energy neutral atoms ($\sim$ 100 keV) into the tokamak plasma. When the energetic atoms penetrate the plasma core, they become ionized and transfer their energy to the plasma, raising the overall temperature. Higher NBI energy is required as the tokamak size increases. The NBI accelerator proposed for ITER will provide neutral beams with energies up to 1 MeV [115].

The ion cyclotron resonance heating (ICRH) has been the most successful method in RF heating [116]. The ICRH heating has many attractive features such as the relatively low frequency (tens of MHz) and efficient power absorption. However, the electron cyclotron resonance heating (ECRH) has some advantages over ICRH like the ability to deposit energy at a desired location where the resonance occurs. This feature is useful for controlling the plasma current profile, which is important in optimizing the energy confinement and in stabilizing the plasma. Figure 2.6 shows a typical RF heating system used in tokamaks.

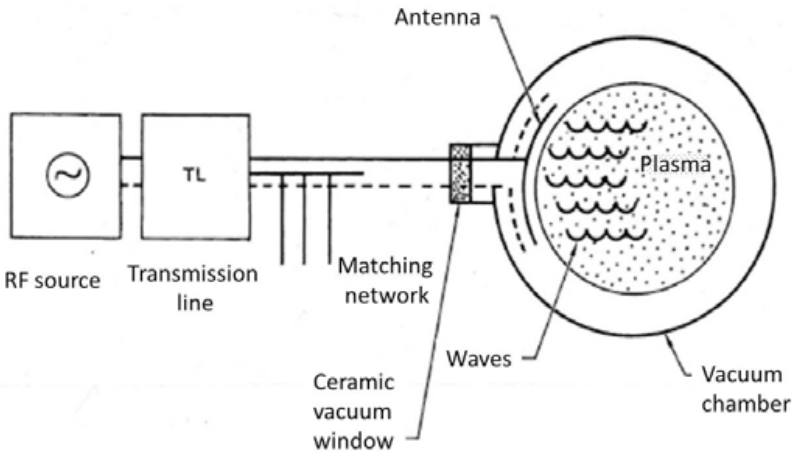

Figure 2.6: Schematic layout of a typical RF heating system [117].

2.5 STOR-M Tokamak

The Saskatchewan Torus-Modified (STOR-M) tokamak is currently the only Canadian research tokamak which is located at the University of Saskatchewan. STOR-M is a small iron core toka-

mak built in 1987 as an upgrade for the previous Saskatchewan Torus-1 Modified (STOR-1M) tokamak [118] which is currently on loan to Utah State University. The toroidal coil system of STOR-M was upgraded in 1994 to increase the strength of toroidal field [119]. Several experiments have been conducted on STOR-M with relevance to larger tokamak programs. Those experiments include alternating current (AC) plasma operation [120], turbulent heating (TH) current pulse [100], plasma biasing [121], spheromak startup simulation [122], density fluctuations studies [123], characterization of MHD instabilities [124], diamagnetic [125] and plasma edge measurements [126, 127]. The University of Saskatchewan Compact Torus Injector (USCTI) was also implemented in STOR-M in 1995 to study fueling in tokamaks, control of plasma rotation, and to drive the bootstrap current through density profile optimization [128]. The compact torus (CT) injector has the ability to fire tangential [129, 130] and vertical [131] CTs relative to the toroidal field of STOR-M. The discharge parameters in STOR-M are listed in Table 2.1

Parameter	**Value**
Toroidal Magnetic Field (B_ϕ)	$\leqslant$ 1 T
Vertical Magnetic Field ($B_\perp$)	60 G
Plasma Current (I_p)	20-30 kA
Loop Voltage (V_l)	3 V
Average Electron Density ($\langle n_e \rangle$)	10^{18}-10^{19} m^{-3}
Average Electron Temperature ($\langle T_e \rangle$)	150 eV
Average Ion Temperature ($\langle T_i \rangle$)	50 eV
Energy Confinement Time (τ_E)	2 ms
Discharge Duration	40 ms
Minor Radius (a)	12.5 cm
Major Radius (R)	46 cm

Table 2.1: Typical discharge parameters in STOR-M.

The STOR-M tokamak consists of a donut-shaped vacuum chamber and a circular limiter made of stainless steel (304L alloy). The limiter consists of a circular part with a radius of 13 cm and a horizontal rail at 12 cm, allowing up to ± 1 cm of horizontal plasma displacement without additional scrape-off. The vacuum chamber has two circular stainless steel elbows attached on one end to

stainless steel bellows to form the two halves of the vacuum chamber. Bellows are used to reduce the mechanical stress on the machine. The chamber is equipped with 23 ports: 11 vertical, 10 horizontal, and 2 tangential available for diagnostics, pumps, the CT injector, and the gas feed system. The vacuum chamber is evacuated to a base pressure of 1×10^{-7} Torr using a turbo-molecular pump (TMP) with a pumping capacity up to 1000 L/sec [132], complemented with a rotary pump for rough pumping. The vacuum chamber is filled with ultra pure hydrogen (99.999%) through a PV-10 piezoelectric valve [133] to maintain a typical operating pressure of about 1.8×10^{-4} Torr through a feedback control system. Additional gas puffing pulses are used to adjust the plasma density during the discharge.

An iron core transformer with inductive magnetic flux capacity of ± 0.1 Wb is used for generating the toroidal ohmic plasma current in STOR-M. The plasma is initiated with a negative bias magnetic flux to gain a sufficient flux swing. The ohmic discharge circuit consists of three capacitor banks. A bias bank (20 mF, 450 V) induces a negatively biased magnetic flux on the iron core. The initial ionization and the current ramp-up is provided by a fast bank (200 mF, 450 V). A slow bank (10 F, 100 V) is used to maintain the plasma current plateau. The horizontal position of the plasma column is controlled by a vertical magnetic field provided by the image currents and the pre-programmed vertical field. A real-time PID feedback (FB) controller [134] maintains the horizontal plasma position based on the position signals. Figure 2.7 shows a vertical cross-section of STOR-M tokamak and the locations of the ohmic heating (OH) primary coils, the vertical equilibrium (VE) coils, and FB coils.

2.6 STOR-M Diagnostics

The discharge parameters are monitored in tokamaks by various diagnostic tools. Some of the diagnostics, like the magnetic probes, are passive, thus they are installed away from the plasma. The non-invasive diagnostics allow the measurements of plasma parameters without disturbing the plasma itself. However, other probes (e.g. Langmuir probes) require a direct contact with the

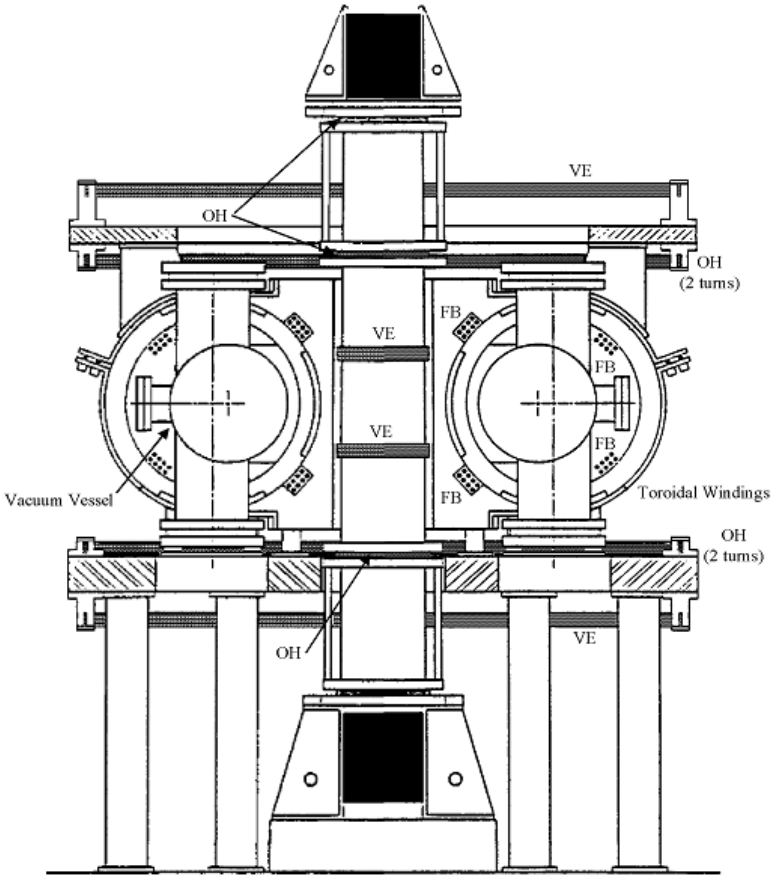

Figure 2.7: Side view of the STOR-M tokamak showing the locations of the vertical equilibrium (VE), ohmic heating (OH), and feedback (FB) windings.

plasma which can be a source of impurities. The long exposure to the hot plasma may also burn and damage the probes. Discharge parameters are routinely monitored in STOR-M by a variety of diagnostic instruments listed in Table 2.2. This section describes the basics of some diagnostics used in STOR-M.

2.6.1 Rogowski Coils

Tokamaks are equipped with numerous Rogowski coils to measure electric currents and to compensate for stray magnetic fields. As shown in Figure 2.8, Rogowski coil is a torus-shaped solenoid with a winding density n (turns/m) and a uniform cross-section A. According to Ampère's law, an electric current (I) passing through the center of the coil induces a perpendicular magnetic

Diagnostic	Parameter
Rogowski Coils	Plasma Current (I_p) and Toroidal Field (B_ϕ)
Voltage Pick-Up Loop	Loop Voltage (V_l) and Transformer Flux (Φ_{OH})
Microwave Interferometer (4 mm)	Line-Averaged Electron Density ($\langle n_e \rangle$)
Position Sensing Coils	Plasma Position (ΔH)
Mirnov Coils	MHD Magnetic Fluctuations ($\tilde{B}$)
Optical Spectrometry	H_α Emissions
Ion Doppler Spectroscopy	Impurity Flow Measurements
Gundestrup Probe	Plasma Flow Measurements ($M_{\parallel,\perp}$)
Langmuir Probes	Floating Potential (V_f) and Ion Saturation Current (I_{si})
Soft X-Ray Cameras	Perturbed Electron Density ($\tilde{n}_e$) and Temperature ($\tilde{T}_e$)

Table 2.2: List of available STOR-M diagnostics.

field B_θ [135]:

$$\oint_l \mathbf{B}_\theta \cdot d\mathbf{l} = \mu I \tag{2.36}$$

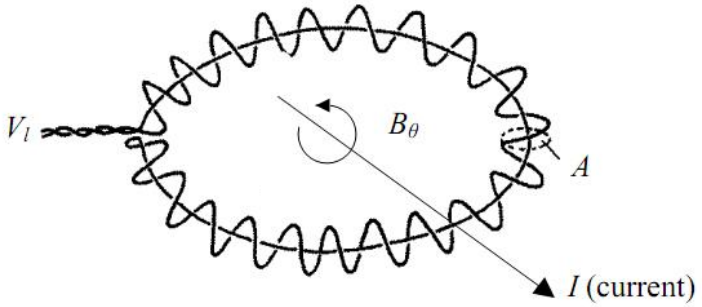

Figure 2.8: Schematic of Rogowski coil [136].

where $d\mathbf{l}$ is the the line element along the solenoidal axis, and μ is the magnetic permeability of the medium in the solenoid. The total magnetic flux Φ enclosed by the coil is determined by the Faraday's law of induction as:

$$\Phi = n \oint_l \int_A dA \mathbf{B}_\theta \cdot d\mathbf{l} \tag{2.37}$$

Substituting Equation 2.36 into Equation 2.37 provides the magnetic flux expressed in terms of I:

$$\Phi = nA\mu I \tag{2.38}$$

The time rate of change of the magnetic flux represents the voltage picked up by the Rogowski coil:

$$V = \dot{\Phi} = nA\mu\dot{I} \tag{2.39}$$

Integrating the above equation yields the current measured by the Rogowski coil:

$$I = \frac{1}{nA\mu}\int V dt \tag{2.40}$$

Rogowski coils used in STOR-M are homemade coils that measure the currents in various field windings and in the plasma itself. Each coil has a frequency response up to 800 kHz which is adequate for current measurements in STOR-M. The coils are calibrated against a commercial Rogowski coil (Pearson Electronics). The output signals of the coils are integrated by actively gated integrators and connected to a data acquisition system.

2.6.2 Voltage Pick-Up Loop

The measurements of loop voltage in tokamaks provide useful information about the plasma resistance and temperature as well as the level of impurities concentration. The measured loop voltage (V_l) consists of resistive and inductive components:

$$V_l = I_p R_p + \frac{d}{dt}\left(I_p L_p\right) \tag{2.41}$$

where R_p is the plasma resistance and L_p is the plasma inductance. The plasma resistance is given by [137]:

$$R_p = \eta\frac{2\pi R}{\pi a^2} \tag{2.42}$$

where R is the major radius, a is the minor radius and η is the plasma resistivity. The plasma inductance was previously introduced in Equation 2.21. The loop voltage, combined with the plasma current, is used to estimate the electron temperature from the neoclassical plasma resistivity (η_{nc}). In the quasi-steady plasma, the plasma resistance defined by Equation 2.42 can be simplified

to $R_p \approx V_l/I_p$. The neoclassical resistivity can be approximated with the following expression [138]:

$$\eta_{nc} = \frac{\eta_S}{1 - 1.95\sqrt{\epsilon} + 0.95\epsilon} \tag{2.43}$$

where η_S is the classical Spitzer resistivity defined by Equation 2.33, and ϵ is the inverse aspect ratio of a tokamak ($\epsilon = \frac{a}{R} \approx 0.3$ in STOR-M) which accounts for trapped electrons. $\sqrt{\epsilon}$ is approximately the fraction of trapped electrons. The electron temperature can be estimated from the plasma resistivity as:

$$T_e \approx \left(\frac{0.01326}{1 - 1.95\sqrt{\epsilon} + 0.95\epsilon} \frac{I_p R}{V_l a^2} \right)^{2/3} \tag{2.44}$$

For a typical STOR-M discharge ($I_p \approx 25$ kA, $V_l \approx 3$ V), the average electron temperature is around 200 eV.

The loop voltage is measured in STOR-M by a single turn coaxial cable mounted on top of the vacuum chamber and parallel to the plasma current. The output signal is transmitted to the data acquisition system via a triaxial cable. A 100:1 voltage divider is used to attenuate the output voltage and to provide the necessary impedance matching. Figure 2.9 shows the loop voltage circuit used in STOR-M.

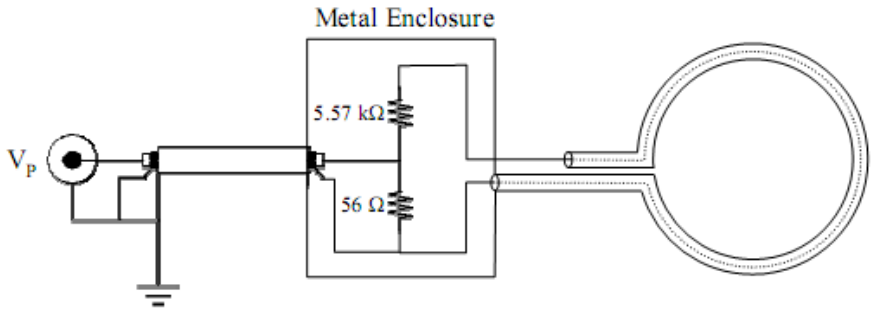

Figure 2.9: Voltage pick-up loop circuit [139].

2.6.3 Position Sensing Coils

The performance of a tokamak discharge depends on the accuracy of the plasma position (ΔH) control. A set of magnetic coils called position sensing coils are implemented in tokamaks to

measure the location of the plasma inside the vacuum chamber. The coil arrangement shown in Figure 2.10 is used in STOR-M to measure the vertical and horizontal displacement of the plasma column. The coils are installed outside the vacuum chamber at a radius of $r = 17$ cm. The coil system consists of six magnetic probes. Four of the probes, poloidally separated by 90°, measure the poloidal magnetic field B_θ at the same toroidal location. The remaining two coils are installed above and below the vacuum chamber to detect the radial magnetic field B_r.

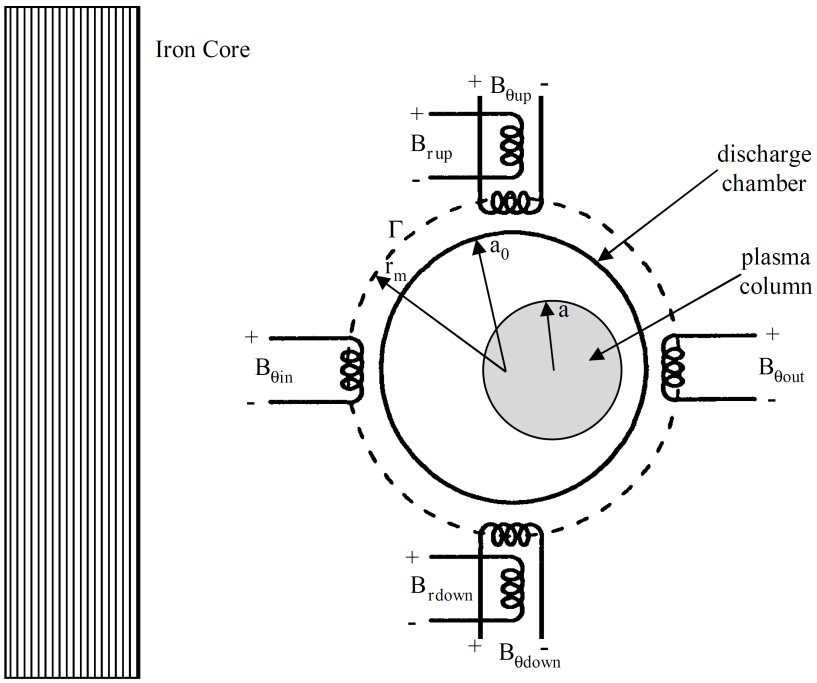

Figure 2.10: Position sensing coils in STOR-M [140].

The position coils detect magnetic fields from the plasma as well as from the toroidal coil system due to the coils misalignment and imperfection. The unwanted fields can be eliminated from the position signals by using a compensation circuit. Rogowski coils are used to determine the current waveforms that produce the stray fields. These waveforms are then added with the appropriate amplitude and polarity to the position sensing coil signals to cancel out the unwanted fields.

2.6.4 Optical Spectrometer

The quality of a tokamak plasma can be determined by measuring the intensity of the line emissions from hydrogen and impurities in the plasma. The H_α radiation represents the recycling process of plasma particles in the edge region. A lower H_α emission level indicates better plasma confinement. As shown in Figure 2.11, the H_α emission line (656.28 nm) is measured in STOR-M by a 350 mm focal length single-pass Czerny-Turner grating monochromator (Heath EU-700) with a relative aperture of $f/6.8$ and a resolution of 1 Å. The grating has 1180 lines/mm and is blazed at 2500 Å. The monochromator is connected to optical lenses via a fiber optical bundle to detect the light emission from a quartz window located at the bottom of the vacuum chamber. The dispersed light is collected by a photomultiplier tube (RCA IP-28) shielded from the external magnetic fields with μ-metal and enclosed in a brass and copper housing.

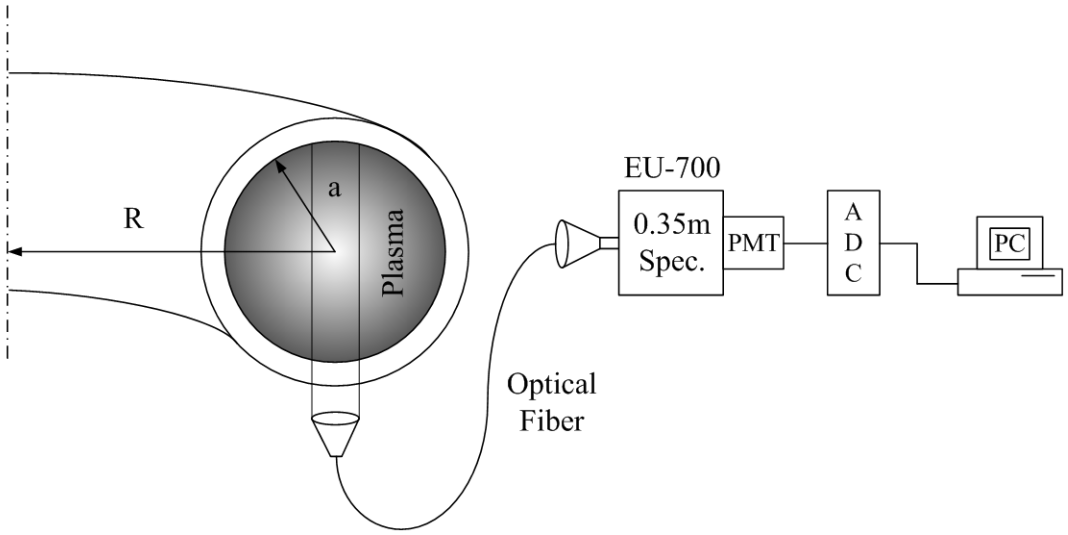

Figure 2.11: Monochromator set-up for H_α measurements in STOR-M.

Chapter 3

Theory

3.1 Introduction

One of the successful models to study the plasma dynamics is the MHD model. The MHD theory is a single-fluid approximation which can explain the behaviour of a conductive fluid in electric and magnetic fields (such as plasmas). Furthermore, plasma equilibria and macroscopic instabilities observed in tokamaks are well described by the MHD theory. This chapter explains the basics of the MHD theory and the macroscopic instabilities, particularly the magnetic islands. The mechanisms of plasma rotation and transport in tokamaks are also discussed along with a theoretical background of some signal processing techniques.

3.2 MHD Theory

The MHD theory is a theoretical model that describes the macroscopic dynamics created by the motion of charged particles in a charge-neutral fluid such as a plasma. The MHD theory also studies the interaction between the charged particles and the surrounding magnetic fields. The motion of the charged particles creates electric currents which in turn generate magnetic fields. In the ideal MHD theory, all dissipative effects such as viscosity, resistivity and thermal conductivity are negligible, except the thermal conductivity along the magnetic field which is taken to be infinite.

Furthermore, the collisions between electrons and ions are ignored, and the simple Ohm's law $\mathbf{E} + \mathbf{v} \times \mathbf{B} = 0$ is adopted.

The two-fluid model treats the electron and ion fluids separately as a conducting fluid. The two fluids interact through the self-induced electric and magnetic fields. These fields respond to the changes in the charge densities and currents of the two fluids. The macroscopic scale of each fluid is assumed to contain a large number of charged particles. The spatial scale of the two fluids is large compared to the mean-free path between the particle collisions and the Larmor radius of each individual particle [141].

In the ideal MHD model, the derivation of MHD equations can be limited to the case of a hydrogen plasma, in which the ions and electrons have respective charges $\pm e$ and the charge neutrality is satisfied ($n_i \approx n_e \approx n$). The contribution of electrons to the fluid inertia can also be neglected due to the incomparable mass of electrons to that of ions. The MHD model treats the plasma as a single fluid with ion mass density [142]

$$\rho = n_i M + n_e m \approx n\,(M + m) \approx nM \tag{3.1}$$

ion mass velocity

$$\mathbf{v} = \frac{n_i M \mathbf{v}_i + n_e m \mathbf{v}_e}{\rho} \approx \frac{M\mathbf{v}_i + m\mathbf{v}_e}{M + m} \approx \mathbf{v}_i \tag{3.2}$$

and current density:

$$\mathbf{J} = e(n_i \mathbf{v}_i - n_e \mathbf{v}_e) \approx ne(\mathbf{v}_i - \mathbf{v}_e) \tag{3.3}$$

where m is the electron mass, M is the ion mass, n is the plasma density, $\mathbf{v}_e$ is the electron velocity and $\mathbf{v}_i$ the ion velocity. The terms that contain the mass ratio m/M are ignored because the electron mass m is negligible compared with the ion mass M. The single-fluid MHD equations can be derived by taking various linear combinations of the individual ion and electron equations. In particular, the two individual continuity equations

$$\frac{\partial n_{i,e}}{\partial t} + \nabla \cdot (n_{i,e} \mathbf{v}_{i,e}) = 0 \tag{3.4}$$

are multiplied by the ion and electron masses M and m, and added together to produce the mass continuity equation:

$$\frac{\partial \rho}{\partial t} + \nabla \cdot (\rho \mathbf{v}) = 0 \tag{3.5}$$

Similarly, the individual fluid equations of motion [143]

$$Mn_i \frac{d\mathbf{v}_i}{dt} = en_i(\mathbf{E} + \mathbf{v}_i \times \mathbf{B}) - \nabla p_i \tag{3.6}$$

$$mn_e \frac{d\mathbf{v}_e}{dt} = -en_e(\mathbf{E} + \mathbf{v}_e \times \mathbf{B}) - \nabla p_e \tag{3.7}$$

are added together to produce the combined single-fluid equation of motion:

$$\rho \frac{d\mathbf{v}}{dt} = \rho \left(\frac{\partial \mathbf{v}}{\partial t} + \mathbf{v} \cdot \nabla \mathbf{v} \right) = \mathbf{J} \times \mathbf{B} - \nabla p \tag{3.8}$$

where $(\mathbf{v} \cdot \nabla \mathbf{v})$ is the convection term and the total pressure p is the sum of the ion and electron pressures:

$$p = p_e + p_i = n(T_e + T_i) \tag{3.9}$$

where T_e and T_i are the electron and ion temperatures, respectively. The MHD model also requires an equation of state to describe the time variation of plasma pressure p:

$$p = C\rho^\gamma \quad \rightarrow \quad \frac{d}{dt}\left(\frac{p}{\rho^\gamma} \right) = 0 \tag{3.10}$$

where C is a constant and γ is the adiabatic index defined for an ideal gas with an N number of degrees of freedom as:

$$\gamma = \frac{2 + N}{N} \tag{3.11}$$

The set of MHD equations is completed by including Maxwell's equations with some approxima-

tions for plasma, i.e., the displacement current and the net charge density are negligible [144]:

$$\nabla \times \mathbf{B} = \mu_0 \mathbf{J} \tag{3.12}$$

$$\nabla \times \mathbf{E} = -\frac{\partial \mathbf{B}}{\partial t} \tag{3.13}$$

$$\nabla \cdot \mathbf{B} = 0 \tag{3.14}$$

$$\nabla \cdot \mathbf{E} = 0 \tag{3.15}$$

3.3 MHD Instabilities

Tokamak plasmas are subject to various types of instabilities. The simplest form of tokamak instabilities is described by the MHD model. MHD instabilities are long wavelength electromagnetic modes characterized by large spatial scales ($\lambda \gg$ ion Larmor radius) and long temporal scales ($\omega \ll \omega_{ci}$). MHD instabilities cause the destruction of magnetic surfaces, the degradation of plasma confinement, and the termination of tokamak discharge [145]. MHD instabilities are divided into two main categories: ideal MHD modes which occur when the plasma is perfectly conducting, and resistive MHD modes which are dependant on the finite resistivity of the plasma.

The stability of ideal MHD modes can be determined by a theoretical principle called the energy principle. The energy principle examines the change in the potential energy due to the plasma displacement. It implies that the ideal MHD modes are regarded as unstable if they lower the potential energy of the plasma. The resistive MHD modes are also considered unstable if the plasma resistivity η is significant in the MHD equations. The change in the potential energy can be estimated by introducing an arbitrary displacement $\boldsymbol{\xi}$:

$$\boldsymbol{\xi} = \boldsymbol{\xi}_0 e^{i(m\theta - n\phi - \omega t)} \tag{3.16}$$

where m and n are the poloidal and toroidal oscillation modes, and ω is the angular frequency of MHD mode that grows and/or decays at rate of $i\omega$. The displacement $\boldsymbol{\xi}$ defines the deviation from

the equilibrium position. The energy change due to the displacement $\boldsymbol{\xi}$ is given by the integration over the plasma volume:

$$\delta W = -\frac{1}{2}\int \boldsymbol{\xi}\cdot\mathbf{F}(\boldsymbol{\xi})dV \tag{3.17}$$

where $\mathbf{F}(\boldsymbol{\xi})$ is the force causing the displacement $\boldsymbol{\xi}$. The force $\mathbf{F}(\boldsymbol{\xi})$ is defined by the linearized momentum equation as:

$$\mathbf{F}(\boldsymbol{\xi}) = \rho\frac{\partial^2\boldsymbol{\xi}}{\partial t^2} = \tilde{\mathbf{J}}\times\mathbf{B}_0 + \mathbf{J}_0\times\tilde{\mathbf{B}} - \nabla\tilde{p} \tag{3.18}$$

where the indices 0 and $\sim$ describe the stable and perturbed quantities, respectively. The perturbed pressure $\tilde{p}$ can be related to the plasma displacement by integrating and linearizing the adiabatic equation (Equation 3.10):

$$\tilde{p} = \gamma p_0\nabla\cdot\boldsymbol{\xi} - \boldsymbol{\xi}\cdot\nabla p_0 \tag{3.19}$$

The perturbed magnetic field $\tilde{\mathbf{B}}$ is derived from integrating Faraday's law of induction (Equation 3.13) together with Ohm's law for a perfect conductor

$$\mathbf{E} + \mathbf{v}\times\mathbf{B} = \eta\mathbf{J} = 0 \tag{3.20}$$

to obtain:

$$\tilde{\mathbf{B}} = \nabla\times(\boldsymbol{\xi}\times\mathbf{B}_0) \tag{3.21}$$

The perturbed current density $\tilde{\mathbf{J}}$ can be obtained from Ampère's law (Equation 3.12) as:

$$\tilde{\mathbf{J}} = \frac{\nabla\times\tilde{\mathbf{B}}}{\mu_0} \tag{3.22}$$

Substituting Equations 3.18, 3.19, 3.21, and 3.22 into Equation 3.17 yields:

$$\delta W = \frac{1}{2}\int\left(\frac{\tilde{B}^2}{\mu_0} + \gamma p_0(\nabla\cdot\boldsymbol{\xi})^2 + (\boldsymbol{\xi}\cdot\nabla p_0)\nabla\cdot\boldsymbol{\xi} - \mathbf{J}_0\cdot(\tilde{\mathbf{B}}\times\boldsymbol{\xi})\right)dV + \frac{1}{2}\int\left(\tilde{p} + \frac{1}{\mu_0}\mathbf{B}_0\cdot\tilde{\mathbf{B}}\right)\boldsymbol{\xi}\cdot d\mathbf{S} \tag{3.23}$$

The last term on the right hand side is a surface term arising from the Gauss's theorem which was

also used in deriving the previous equation. This term is zero if the normal displacement at the surface is zero. The surface term represents the energy transferred from the plasma to the vacuum if there is a vacuum region outside the plasma. The amount of energy transferred to the vacuum is given by:

$$\delta W_{\text{vacuum}} = \int \left(\frac{\tilde{B}_{\text{v}}^2}{2\mu_0} \right) dV \tag{3.24}$$

where $\tilde{B}_{\text{v}}$ is the perturbed magnetic field in vacuum. The total change in the potential energy can be rewritten as:

$$\delta W = \frac{1}{2} \int_{\text{plasma}} \left(\frac{\tilde{B}^2}{\mu_0} + \gamma p_0 (\nabla \cdot \boldsymbol{\xi})^2 + (\boldsymbol{\xi} \cdot \nabla p_0) \nabla \cdot \boldsymbol{\xi} - \mathbf{J}_0 \cdot (\tilde{\mathbf{B}} \times \boldsymbol{\xi}) \right) dV + \int_{\text{vacuum}} \left(\frac{\tilde{B}_{\text{v}}^2}{2\mu_0} \right) dV \tag{3.25}$$

The plasma is regarded as stable if the change in the potential energy is positive ($\delta W > 0$). Otherwise, the plasma is unstable. According to Equation 3.25, MHD instabilities are driven mainly by the plasma pressure gradient and the current density gradient [146]. Therefore, MHD instabilities are classified relative to their destabilizing forces into two types: pressure-driven instabilities which are proportional to the pressure gradient term ∇p_0, and current-driven instabilities correspond to the current source J_0.

Figure 3.1 shows examples of MHD instabilities observed in tokamak plasmas. The sausage and kink modes are typical current-driven instabilities. The plasma is vulnerable mostly to the screw instabilities due to the finite resistivity of the plasma and the helical nature of the magnetic fields in tokamaks. The stability of the screw instabilities is determined by the Shafranov-Kruskal criterion for a toroidal plasma cylinder [147]:

$$B_\phi > \frac{R}{a} B_\theta(a) = \frac{B_\phi}{q(a)} \rightarrow q(a) = \frac{a B_\phi}{R B_\theta} > 1 \tag{3.26}$$

where q is a safety factor typically varies from 1 at the plasma center ($r = 0$) to 3 or higher at the plasma edge ($r = a$). The maximum plasma current achieved in a tokamak discharge is also limited by the so-called $q = 2$ barrier. It is difficult to cross the $q = 2$ barrier without a sufficient

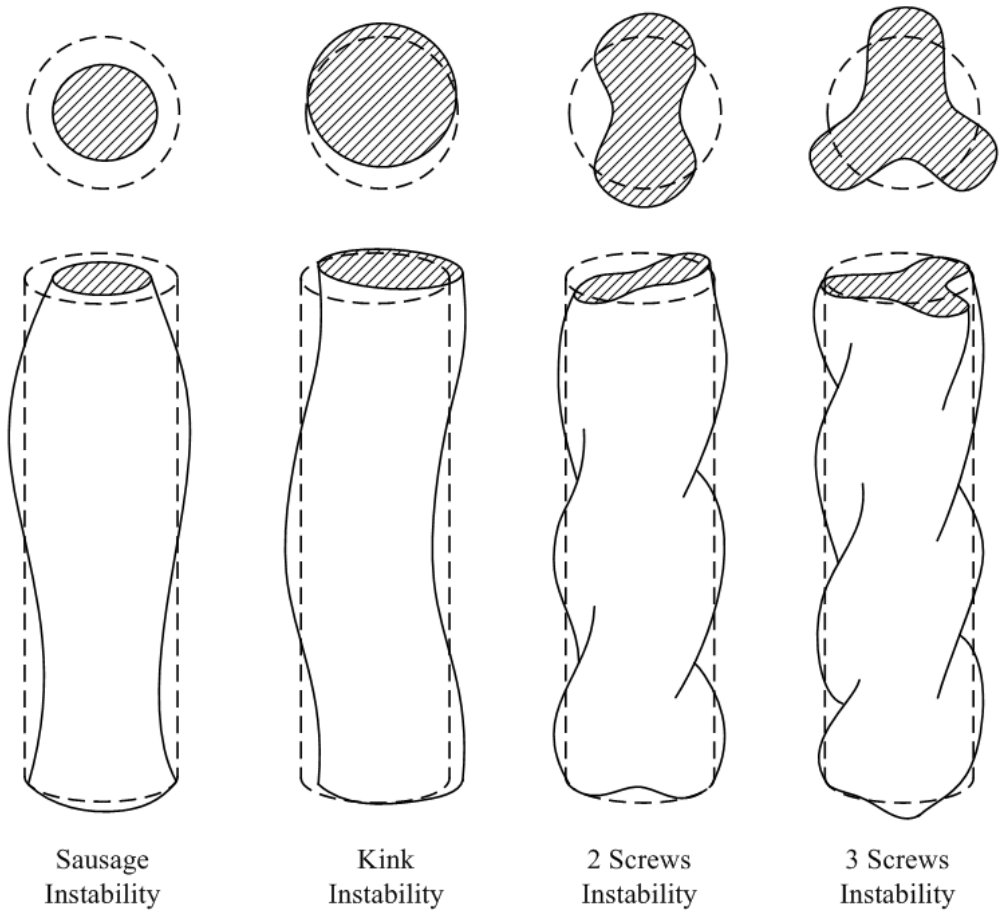

Figure 3.1: Plasma column perturbed by different types of MHD instabilities. The dashed lines outline the unperturbed plasma column.

plasma current ramp-up. The maximum plasma current allowed by the $q = 2$ barrier is determined by:

$$I_p \leqslant \frac{1}{\mu_0}\frac{\pi a^2}{R}B_\phi \tag{3.27}$$

which in turn limits the ohmic heating power in tokamaks.

3.4 Magnetic Islands

The helicity of magnetic field lines plays an important role in characterizing magnetic surfaces in a toroidal equilibrium configuration such as in tokamaks. MHD equilibrium is defined in low beta tokamaks by the magnetic surfaces nested around a single magnetic axis. A field line following

a helical path along a surface either encloses onto itself after a finite integer number of toroidal rotations m around the major axis of the torus with another integer number of poloidal rotations n around the minor torus axis, or continues filling the entire surface indefinitely without closing on itself. The rotation of magnetic field lines inside a toroidal device is described by the rotational transform factor ι [148]:

$$\iota(r) = \frac{RB_\theta(r)}{rB_\phi(r)} \tag{3.28}$$

which depends on the poloidal and toroidal magnetic fields. The rational values of ι factor can be expressed by the ratio of two integer numbers m and n:

$$\iota = \frac{n}{m} \tag{3.29}$$

where m and n are the poloidal mode number and the toroidal mode number, respectively. The twist of magnetic field lines is defined by the safety factor q, the inverse of ι [149]:

$$q(r) = \iota^{-1}(r) = \frac{rB_\phi(r)}{RB_\theta(r)} \tag{3.30}$$

hence:

$$q = \frac{m}{n} \tag{3.31}$$

The magnetic field **B** is well defined inside the plasma by the current density **J**. The magnetic field satisfies the following divergence-free conditions [150]:

$$\nabla \times \mathbf{B} = \mu_0 \mathbf{J} \tag{3.32}$$

$$\nabla \cdot \mathbf{B} = 0 \tag{3.33}$$

As mentioned in Section 2.3, the plasma equilibrium is maintained by the force balance between

the Lorentz force $\mathbf{J} \times \mathbf{B}$ and the pressure gradient ∇p:

$$\mathbf{J} \times \mathbf{B} = \nabla p \tag{3.34}$$

The above equation yields the following conditions for the plasma equilibrium:

$$\mathbf{B} \cdot \nabla p = 0 \tag{3.35}$$

$$\mathbf{J} \cdot \nabla p = 0 \tag{3.36}$$

It is evident from the previous equations that the pressure p is a constant quantity along both the magnetic field $\mathbf{B}$ and the current $\mathbf{J}$. It is also clear from Equation 3.35 that the magnetic field lines cover the surface of a constant p, and the pressure gradient ∇p is perpendicular to that surface. Furthermore, surfaces with different constant pressures do not cross each others. These conditions, however, are satisfied only if the surfaces are nested toroidally. In the magnetic field equilibrium, the nested toroidal surfaces covered by the field lines are called the magnetic flux surfaces. Figure 3.2 shows a schematic of magnetic surfaces uniformly nested around the magnetic axis.

It has been explained earlier that in a low beta equilibrium the magnetic surfaces are toroidally concentric around the magnetic axis. The radial magnetic perturbations in tokamaks, however, tend to break the magnetic surfaces with rational values of q (i.e. resonant surfaces) into thin helical structures called magnetic islands. The magnetic islands, also known as tearing modes, are driven by current gradients in the resistive plasma. As shown in the left diagram of Figure 3.3, there are two equilibrium regions of magnetic field B with opposite directions at both sides of the (m, n) resonant surface. For a plasma with equilibrium magnetic field B, a small radial magnetic perturbation can be assumed in the form:

$$B_r = B_{r,0} e^{im\chi} \tag{3.37}$$

where $B_{r,0}$ is the radial magnetic field at equilibrium, and χ is an angular coordinate orthogonal to

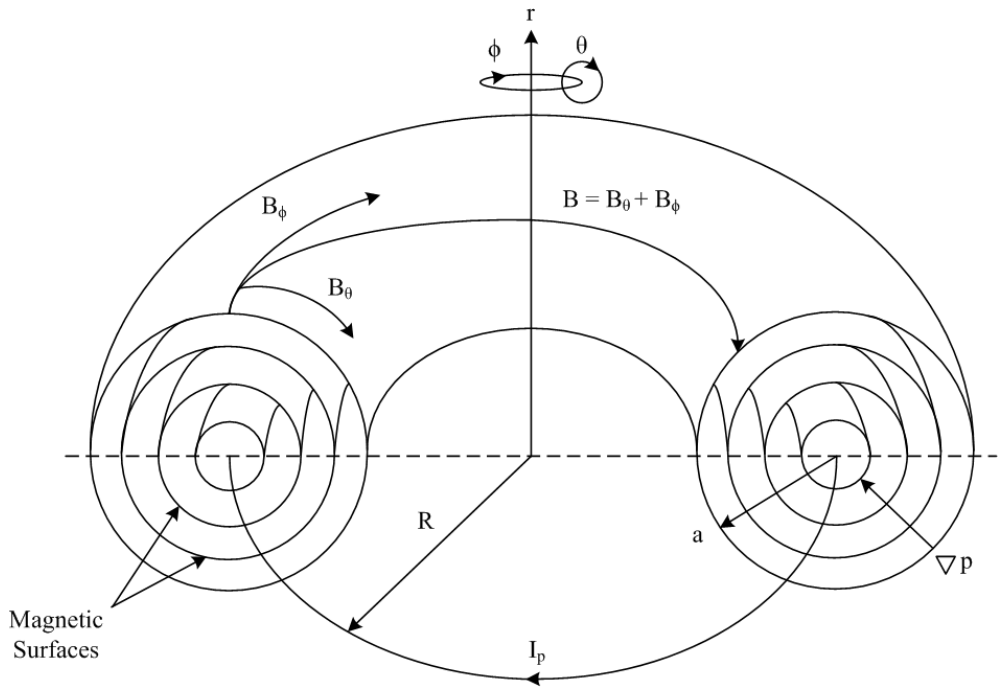

Figure 3.2: Nested magnetic flux surfaces formed by magnetic field lines.

the equilibrium field lines at the (m, n) resonant surface:

$$\chi = \theta - \frac{n}{m}\phi \tag{3.38}$$

The amplitude of the radial perturbations B_r is constant over the minor radius and grows only at the resonant surface s. The equilibrium field in the χ direction is defined by:

$$B^* = B_\theta \left(1 - \frac{n}{m}q\right) \tag{3.39}$$

The Taylor expansion of the above equation around the resonant surface yields:

$$B^* = -\left(B_\theta \frac{q'}{q}\right)_s z \tag{3.40}$$

where $z = r - r_s$ is the radial distance to the rational surface s at minor radius r_s, and $q' = dq/dr$ is the local magnetic shear. The change in the magnetic geometry can be estimated by determining

the trajectory of the magnetic field line:

$$\frac{dr}{r_s d\chi} = \frac{B_r}{B^*} \tag{3.41}$$

The last equation suggests that the presence of any small radial perturbations can alter the topology of the magnetic field lines. The radial magnetic perturbations B_r can be written in the following form [151]:

$$B_r = B_{r,0} \sin(m\chi) \tag{3.42}$$

The differential equation for the magnetic field line is defined in a slab geometry by:

$$-\left(B_\theta \frac{q'}{q}\right)_s z dz = r_s B_{r,0} \sin(m\chi) d\chi \tag{3.43}$$

which is derived from substituting Equations 3.40 and 3.42 into Equation 3.41. The radial magnetic field $B_{r,0}$ is constant over the radial extent of the magnetic island. Integrating Equation 3.43 yields the equation of the magnetic field line:

$$z^2 = \frac{w^2}{8} \left(\cos(m\chi) - \cos(m\chi_0)\right) \tag{3.44}$$

where χ_0 is the value of χ at $z = 0$, and w is the width of the magnetic island defined by the following relation [152]:

$$w = 4\sqrt{\left(\frac{rqB_{r,0}}{mq'B_\theta}\right)_s} \tag{3.45}$$

In the region where the perturbed radial field is positive, the field line located below the rational surface will move up through the surface, resulting in magnetic reconnection with the field line located above the rational surface and pushed down by the negative radial perturbations. The magnetic structure after the reconnection is shown in the right diagram of Figure 3.3, which illustrates the typical topology of a magnetic island. The magnetic flux surfaces inside the reconnection zone are nested around a single magnetic axis called the O-point. The point where the magnetic

reconnection occurs is called the X-point. The flux surfaces connecting the X-points define the separatrix. The island width w is defined by the distance of two separatrix surfaces near the O-point.

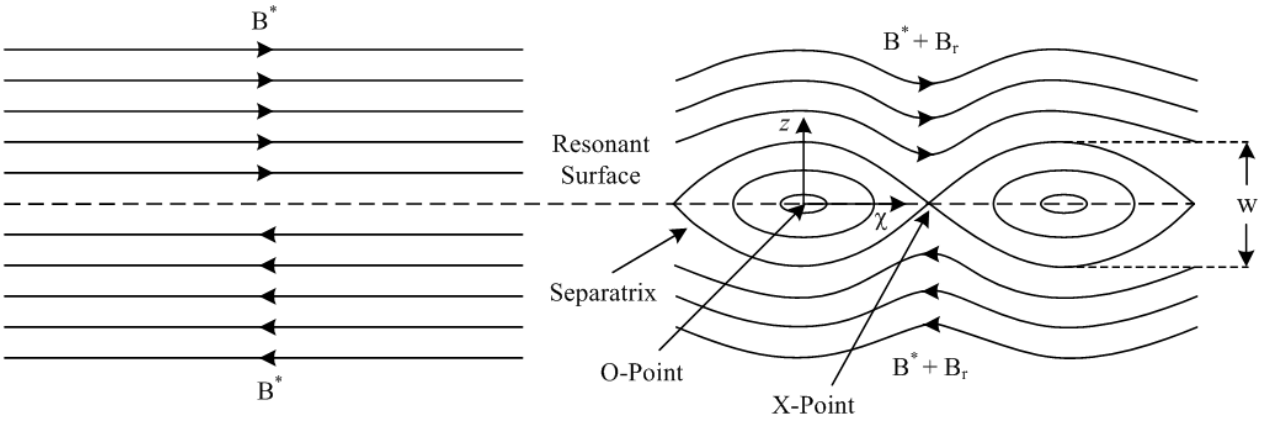

Figure 3.3: The topology of the magnetic island before the magnetic reconnection (left) and after the reconnection (right). The island is formed by the superposition of the perturbed radial magnetic field B_r on the equilibrium field B^* at the resonant surface.

3.5 Plasma Rotation

Plasma rotation plays an important role in many physical phenomena observed in tokamaks. Plasma rotation enhances the stability of magnetic confinement, and suppresses plasma turbulence and MHD instabilities in the edge region. Plasma rotation also controls the plasma transport in tokamaks through the interaction with the radial magnetic fields. The velocity of plasma flow is governed mainly by ions in tokamaks due to the larger ion mass compared with that of electrons:

$$\mathbf{v} \approx \frac{M\mathbf{v}_i + m\mathbf{v}_e}{M+m} \approx \mathbf{v}_i \tag{3.46}$$

The direction of plasma flow velocity can be defined either with respect to the tokamak coordinate system (r, θ, ϕ), or with respect to the total magnetic field **B**. As shown in Figure 3.4, the geometric velocities v_ϕ and v_θ represent the toroidal and poloidal components of the plasma velocity v. The components of plasma velocity parallel and perpendicular to the magnetic field are given

by $v_{\parallel}$ and $v_{\perp}$, respectively. In tokamaks, different diagnostics measure different components of plasma flow. For instance, the optical diagnostics measure the toroidal and poloidal flow velocities, whereas the electrostatic probes (i.e. Mach and Gundestrup probes) measure the plasma flow in parallel and perpendicular directions to the magnetic field.

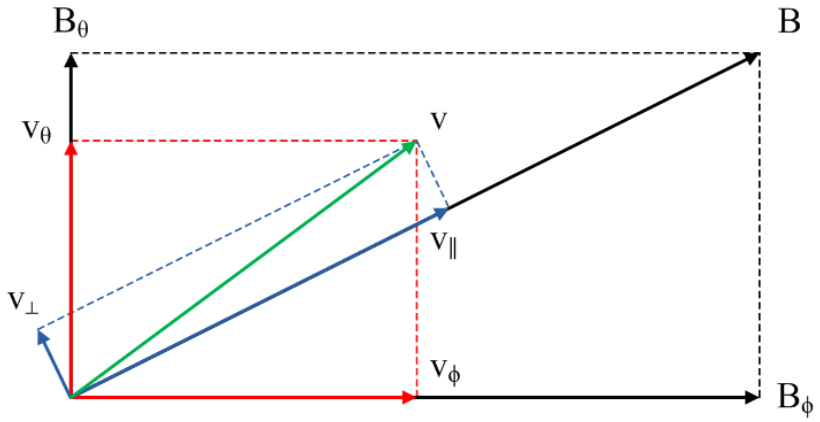

Figure 3.4: The velocity components of plasma flow with respect to the tokamak coordinates (r, θ, ϕ) and the total magnetic field **B**.

The plasma flow is dominated by two types of drifts: the $\mathbf{E} \times \mathbf{B}$ drift and the diamagnetic drift. These basic plasma drifts can be derived for the hydrogen plasma ($Z = 1$) using the equation of motion for ions [153]:

$$Mn\left(\frac{\partial \mathbf{v}}{\partial t} + \mathbf{v} \cdot \nabla \mathbf{v}\right) = en(\mathbf{E} + \mathbf{v} \times \mathbf{B}) - \nabla p \tag{3.47}$$

Assuming a steady state plasma ($\partial/\partial t = 0$) and negligible convective term ($\mathbf{v} \cdot \nabla \mathbf{v}$), the above equation can be reduced to:

$$en(\mathbf{E} + \mathbf{v} \times \mathbf{B}) - \nabla p = 0 \tag{3.48}$$

Taking the cross product with **B** produces the velocity component perpendicular to the magnetic field:

$$en(\mathbf{E} \times \mathbf{B} - \mathbf{v}_{\perp} B^2) - \nabla p \times \mathbf{B} = 0 \tag{3.49}$$

where $\mathbf{v}_\perp$ is the perpendicular ion velocity. Solving Equation 3.49 for $\mathbf{v}_\perp$ yields:

$$\mathbf{v}_\perp = \frac{\mathbf{E}\times\mathbf{B}}{B^2} + \frac{1}{en}\frac{\mathbf{B}\times\nabla p}{B^2} \tag{3.50}$$

The first term in Equation 3.50

$$\mathbf{v}_{\mathbf{E}\times\mathbf{B}} = \frac{\mathbf{E}\times\mathbf{B}}{B^2} \tag{3.51}$$

is the $\mathbf{E}\times\mathbf{B}$ drift velocity, and the second term

$$\mathbf{v}_i^* = \frac{1}{en}\frac{\mathbf{B}\times\nabla p}{B^2} \tag{3.52}$$

is the diamagnetic drift velocity for ions. The diamagnetic drift velocity can be generalized for ions and electrons as:

$$\mathbf{v}^* = \frac{1}{qn}\frac{\mathbf{B}\times\nabla p}{B^2} \tag{3.53}$$

The diamagnetic drift is a fluid drift that creates ion and electron diamagnetic currents of opposite directions. On the contrary, the $\mathbf{E}\times\mathbf{B}$ drift is a particle drift which only causes a charge separation. The main contribution of electric field in the plasma flow comes from the radial component E_r since the toroidal electric field E_ϕ mostly drives electrons rather than ions. The magnetic field in tokamaks is radially asymmetric due to the toroidal geometry of the vacuum chamber. The radial profile of the toroidal magnetic field

$$B_\phi \simeq B_0\left(1 - \frac{r}{R}\cos\theta\right) \tag{3.54}$$

implies that the toroidal magnetic field is stronger in the inner tokamak side compared with the outer side. The poloidal plasma flow v_θ experiences a periodic variation in the magnetic field which called the magnetic pumping [154]. Therefore, the poloidal rotation is damped except for the neoclassical contribution of the ion temperature gradient. The toroidal flow velocity v_ϕ can be derived from the radial force balance equation. The radial force balance equation is defined

by [155]:

$$B_\theta v_\phi - B_\phi v_\theta = E_r - \frac{1}{en}\frac{dp}{dr} \tag{3.55}$$

which is the radial component of Equation 3.48. The toroidal flow velocity is the sum of the $\mathbf{E} \times \mathbf{B}$ drift velocity and the ion diamagnetic velocity in the toroidal direction:

$$v_\phi = \frac{1}{B_\theta}\left(E_r - \frac{1}{en}\frac{dp}{dr}\right) \tag{3.56}$$

The poloidal flow v_θ is omitted due to the poloidal flow damping. The previous equation clearly suggests that the direction of v_ϕ is determined by the direction of the poloidal magnetic field B_θ that is produced by the plasma current I_p in tokamaks. As shown in Figure 3.5, the direction of toroidal flow is assumed to be in the same direction as that of I_p, so that $\mathbf{v}_i^* > \mathbf{v}_{\mathbf{E}\times\mathbf{B}}$. Reversing the direction of plasma current causes the reversal of the poloidal magnetic field, which consequently reverses the direction of toroidal flow.

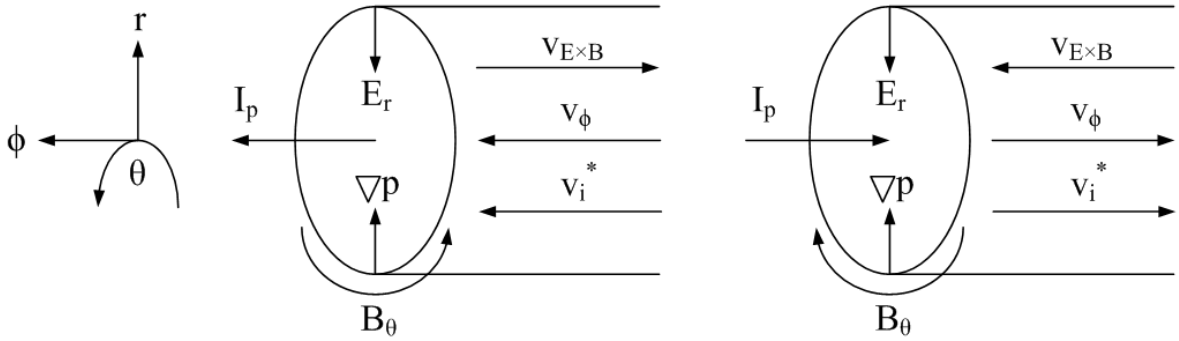

Figure 3.5: The direction of toroidal flow velocity v_ϕ with normal plasma current configuration and reversed current configuration.

3.6 Plasma Transport

In a collisionless plasma with straight magnetic field lines, particles move along the field lines in a circular motion with a radius defined by the Larmor radius r_L. In such a plasma, there is no perpendicular particle transport since there is no perpendicular displacement of particles from one

field line to another. However, collisions between the particles cause a deviation in the particle trajectory. The particles are displaced by a distance in the order of Larmor radius and in the direction perpendicular to the magnetic field. The classical transport in a cylindrical plasma is given by the particle diffusivity across the magnetic field:

$$D_c = \nu r_L^2 \tag{3.57}$$

where ν is the collision frequency which is the electron-ion collision frequency in a fully ionized plasma. The magnetic curvature and gradient in the toroidal magnetic field lead to an enhanced transport called the neoclassical transport. The neoclassical transport depends on the collisionality of the plasma. In a highly collisional plasma, the transport is known as the Pfirsch-Schlüter transport, whereas in a low collisional plasma, the trapped particles cause the so-called banana transport. The classical diffusivity in a toroidal geometry is enhanced by a factor of $(1 + q^2)$ due to the toroidicity [156]:

$$D_{ps} = \nu r_L^2 (1 + q^2) \tag{3.58}$$

where q is the safety factor. The above equation is known by the Pfirsch-Schlüter formula which is valid in the collisional regime characterized by:

$$\nu > \frac{v_T}{qR} \tag{3.59}$$

where v_T is the electron thermal velocity. It seems that as the plasma temperature increases the collision frequency decreases, leading to less diffusivity in the plasma. On the contrary, in the collisionless regime (banana region), the diffusivity is enhanced by the trapped particles [157]:

$$D \simeq \frac{D_{ps}}{\epsilon^{3/2}} \tag{3.60}$$

where ϵ is the inverse aspect ratio. Equation 3.60 is only valid in regimes with a collision frequency of:

$$\nu < \epsilon^{3/2} \frac{v_T}{qR} \tag{3.61}$$

In the intermediate collisionality regime, where

$$\epsilon^{3/2} \frac{v_T}{qR} < \nu < \frac{v_T}{qR} \tag{3.62}$$

the diffusivity becomes insensitive to the collision frequency:

$$D \simeq r_L^2 q^2 \frac{v_T}{qR} \tag{3.63}$$

This regime is called the plateau regime [158]. Figure 3.6 shows the neoclassical prediction of the diffusion coefficient D as a function of the collisionality parameter ν^* ($= \frac{\nu qR}{v_T}$).

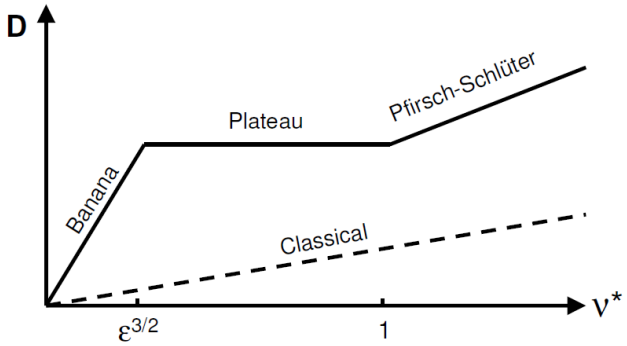

Figure 3.6: The variation of the diffusion coefficient with the collisionality parameter in the three neoclassical transport regimes. The dashed line represents the behaviour of the classical diffusion coefficient.

For standard STOR-M parameters at the plasma center ($n_e \simeq 2 \times 10^{19}$ m^{-3}, $T_e \simeq 200$ eV), the electron-ion collision frequency is about 2.2 $\times 10^5$ s^{-1}. The estimated collision frequency is three times smaller than $\epsilon^{3/2} v_T/qR$ ($\simeq$ 6.9 $\times 10^5$ s^{-1}), and the plasma is marginally in the collisionless regime. However, the plasma density and temperature are low in the edge region of STOR-M ($n_e \simeq 3 \times 10^{18}$ m^{-3}, $T_e \simeq 30$ eV). The collision frequency at the plasma edge is around 1 $\times 10^6$ s^{-1}, which is smaller than v_T/qR ($\simeq$ 2 $\times 10^6$ s^{-1}) and larger than $\epsilon^{3/2} v_T/qR$ ($\simeq$ 2.6 $\times 10^5$ s^{-1}).

Therefore, the edge plasma in STOR-M is in the plateau regime, or near the collisional regime.

3.7 Frequency Analysis

Plasma diagnostics often measure fluctuations caused by plasma instabilities in tokamaks. These fluctuations contain useful information in the frequency domain. Different numerical techniques are implemented to convert the fluctuating signals from the time domain to the frequency domain. The Fourier transform is considered the leading technique of domain conversion. However, the Fourier transform is known for its limitation in handling transient and non-stationary signals. Alternative methods such as the wavelet transform are necessary for the time-resolved frequency analysis. The Fourier and wavelet transforms are discussed in this section.

3.7.1 Fourier Transform

The Fourier transform is one of the best-known integral transforms. It was first introduced by *Joseph Fourier* in the early 1800's. The Fourier transform has led to the development of many efficient algorithms for signal processing. The Fourier transform decomposes any waveform into an infinite sum of harmonic oscillations at definite frequencies equal to the integer multiples of the fundamental frequency (lowest non-zero frequency in the sequence). Any aperiodic function can be expressed by the Fourier transform as an integral sum over a continuous range of frequencies. The equivalent Fourier integral for a continuous function $x(t)$ in the time domain can be expressed by [159]:

$$x(t) = \int_{-\infty}^{\infty} X(f) e^{i2\pi ft} df \tag{3.64}$$

The determination of $X(f)$ represents the central problem of Fourier analysis. The function $X(f)$ is known as the Fourier transform of $x(t)$ in the frequency domain:

$$X(f) = \int_{-\infty}^{\infty} x(t) e^{-i2\pi ft} dt \tag{3.65}$$

where the independent variable t represents time in seconds, and the transform variable f is the frequency in hertz. A discrete version of Fourier transform has also been developed for data recorded by digitizers. The discrete Fourier transform (DFT) of a discrete signal $x(t_n)$ with a total number of samples M and sampling time t_s is defined by [160]:

$$X(f_k) = \sum_{n=0}^{M-1} x(t_n) e^{-i2\pi kn/M}, \quad k = 0, 1, 2, \cdots, M-1 \tag{3.66}$$

where $X(f_k)$ is computed at discrete frequencies f_k. The inverse discrete Fourier transform (IDFT) is given by:

$$x(t_n) = \frac{1}{M} \sum_{k=0}^{M-1} X(f_k) e^{i2\pi kn/M}, \quad n = 0, 1, 2, \cdots, M-1 \tag{3.67}$$

The definition of DFT in Equation 3.66 indicates that M complex multiplications are needed to calculate one output. In order to compute M outputs, a total of approximately M^2 complex multiplications are required. A 1024-point DFT requires more than one million complex multiplications and additions. The number of DFT computations was drastically reduced when the fast Fourier transform (FFT) was introduced by *James Cooley* and *John Tukey* [161]. The FFT algorithm takes the advantage of the fact that many computations are redundant in the DFT analysis due to the periodic nature of the twiddle factor $e^{-i2\pi/M}$. However, the FFT algorithm is more complicated to implement than DFT because it becomes lengthy when M is not a power of 2. This restriction on M can be overcome by appending zeros at the end of the sequence to make M a power of 2 without changing the spectrum of the signal.

3.7.2 Wavelet Transform

The wavelet transform is based on a concept called the multi-resolution analysis which provides a comprehensive time-frequency spectrum for any transient signal. The wavelet analysis calculates the spectrum using a fully scalable modulated window shifted along the signal. This process is repeated multiple times with a slightly shorter (or longer) window for every new cycle. The wavelet spectrum contains a collection of time-frequency representations of the signal with different reso-

lutions, which defines the concept of multi-resolution analysis. The wavelet transform described earlier is known as the continuous wavelet transform (CWT). The wavelet coefficients for a one-dimensional signal $x(t)$ are rigorously calculated from [162]:

$$\text{CWT}\{x(t)\}(s,\tau) = \langle x(t), \psi_{s,\tau} \rangle = \int_{-\infty}^{\infty} x(t)\psi^*_{s,\tau}(t)dt \tag{3.68}$$

where the asterisk (*) denotes complex conjugate. The wavelet coefficients are generated from the mother wavelet $\psi(t)$. The time and the frequency axes of the wavelet spectrum are determined respectively by the time parameter τ and the scale s. The wavelet function $\psi_{s,\tau}(t)$ (also called the child wavelet) is defined as the translation and the re-scale of the mother wavelet $\psi(t)$:

$$\psi_{s,\tau}(t) = \frac{1}{\sqrt{s}}\psi\left(\frac{t-\tau}{s}\right) \tag{3.69}$$

There is a wide variety of choices for mother wavelets. The choice of a particular mother wavelet is utterly determined by the application of interest. For a basic signal analysis, it is preferable to choose a complex-valued mother wavelet with a simple relationship between the scale and the frequency. This criteria is well satisfied by a modulated Gaussian function called the Morlet wavelet. The Morlet wavelet $\psi_{\text{Morlet}}(t)$ is defined by [101]:

$$\psi_{\text{Morlet}}(t) = \frac{1}{\sqrt{\pi f_b}} e^{i2\pi f_c t - \left(\frac{t^2}{f_b}\right)} \tag{3.70}$$

which depends on the bandwidth frequency f_b and the central frequency f_c. Although the central frequency of the Morlet wavelet has a full control on the time and the frequency resolutions, the admissibility condition of the Morlet wavelet is verified only if $f_c > 0.8$ Hz (the wavelet duration is in seconds) to avoid problems at low central frequency (high time resolution) [163].

The scales of the wavelet analysis are similar to those used in maps. The high scales correspond to a non-detailed view of the signal, whereas the low scales provide more details about the signal. In a real signal analysis, the low scales do not last the entire duration of the signal as they appear

from time to time as short bursts, unlike the high scales which usually last longer.

3.8 Harmonic Analysis

Magnetic islands observed in tokamaks usually rotate on different resonant surfaces with either the same or different oscillating frequencies. The corresponding magnetic oscillations contain information about the spatial and temporal harmonics of islands. Numerical techniques such as the spatial Fourier series and the singular value decomposition algorithm are utilized to perform a harmonic analysis on signals carrying multiple harmonics. The techniques used for the harmonic analysis are explained briefly below.

3.8.1 Spatial Fourier Series

The spatial Fourier series decomposes any continuous function into an infinite set of simple oscillating functions, namely sines and cosines. The time-varying function $x(t)$ can be decomposed into an infinite sum of harmonics m at multiples of the fundamental frequency f. The Fourier series expansion of $x(t)$ is given by [164]:

$$x(t) = \frac{C_0}{2} + \sum_{m=1}^{\infty} [C_m \cos(2\pi m f t) + S_m \sin(2\pi m f t)] \tag{3.71}$$

where C_0, C_m and S_m are the Fourier coefficients of the m^{th} harmonic. The Fourier coefficients can be evaluated by integrating over an arbitrary period $(-p, p)$:

$$\begin{aligned} C_0 &= \frac{1}{p}\int_{-p}^{p} x(t)dt \\ C_m &= \frac{1}{p}\int_{-p}^{p} x(t)\cos\frac{m\pi t}{p}dt \\ S_m &= \frac{1}{p}\int_{-p}^{p} x(t)\sin\frac{m\pi t}{p}dt \end{aligned} \tag{3.72}$$

where the frequency f was replaced by $\frac{1}{2p}$. C_0 is the cosine coefficient at $m = 0$, whereas C_m and S_m are the cosine and the sine coefficients of $m \geqslant 1$. The sine coefficient S_0 at $m = 0$ is zero because $\sin(0) = 0$. The Fourier series of a periodic function $x(t)$ can be reduced to a half-ranged expansion within the interval (0, p):

$$\begin{aligned} C_0 &= \frac{2}{p}\int_0^p x(t)dt \\ C_m &= \frac{2}{p}\int_0^p x(t)\cos\frac{m\pi t}{p}dt \\ S_m &= \frac{2}{p}\int_0^p x(t)\sin\frac{m\pi t}{p}dt \end{aligned} \tag{3.73}$$

The Fourier coefficients in Equation 3.73 can be generalized for a discrete signal $x(\theta, t)$ as [165]:

$$\begin{aligned} C_0(t) &= \frac{2}{N}\sum_{i=1}^{N} x(\theta_i, t) \\ C_m(t) &= \frac{2}{N}\sum_{i=1}^{N} x(\theta_i, t)\cos m\theta_i \\ S_m(t) &= \frac{2}{N}\sum_{i=1}^{N} x(\theta_i, t)\sin m\theta_i \end{aligned} \tag{3.74}$$

where m is a spatial harmonic carried by the signal $x(\theta_i, t)$ and observed at the angular location $\theta_i = i\left(\frac{2\pi}{N}\right)$. The Fourier expansion of $x(\theta, t)$ is given by:

$$x(\theta, t) = \frac{C_0(t)}{2} + \sum_{m=1}^{N/2}\left[C_m(t)\cos(m\theta) + S_m(t)\sin(m\theta)\right] \tag{3.75}$$

The above equation can be rewritten as:

$$x(\theta, t) = \frac{C_0(t)}{2} + \sum_{m=1}^{N/2}\left[b_m(t)\cos(m\theta - \phi_m(t))\right] \tag{3.76}$$

where $b_m(t)$ and ϕ_m are the magnitude and the phase of the m^{th} harmonic:

$$b_m(t) = \sqrt{C_m^2(t) + S_m^2(t)} \tag{3.77}$$

$$\phi_m(t) = \tan^{-1}\left(\frac{S_m(t)}{C_m(t)}\right) \tag{3.78}$$

3.8.2 Singular Value Decomposition

Singular value decomposition (SVD) is a linear algebraic algorithm that calculates the eigenvectors and the eigenvalues of the covariance matrix for any data matrix. SVD decomposes any matrix **X** with a size of $M \times N$, where $M(\text{number of rows}) \geqslant N(\text{number of columns})$, into a factorization of three matrices $\mathbf{USV}^T$. The **U** matrix is an $M \times M$ column-orthogonal matrix, **S** is an $M \times N$ diagonal matrix, and $\mathbf{V}^T$ is the transpose of **V**, an $N \times N$ orthogonal matrix. The full expansion of **X** is given by [166]:

$$\mathbf{X} = \begin{pmatrix} x_{11} & \cdots & x_{1N} \\ x_{21} & \cdots & x_{2N} \\ \vdots & \ddots & \vdots \\ x_{M1} & \cdots & x_{MN} \end{pmatrix} = \begin{pmatrix} u_{11} & u_{12} & \cdots & u_{1M} \\ u_{21} & u_{22} & \cdots & u_{2M} \\ \vdots & \vdots & \ddots & \vdots \\ u_{M1} & u_{M2} & \cdots & u_{MM} \end{pmatrix} \cdot \begin{pmatrix} s_{11} & \cdots & 0 \\ \vdots & \ddots & \vdots \\ 0 & \cdots & s_{NN} \\ \vdots & \ddots & \vdots \\ 0 & \cdots & 0 \end{pmatrix} \cdot \begin{pmatrix} v_{11} & \cdots & v_{1N} \\ \vdots & \ddots & \vdots \\ v_{N1} & \cdots & v_{NN} \end{pmatrix}^T \tag{3.79}$$

The columns of **U** are the normalized eigenvectors of the time-covariance matrix $\mathbf{XX}^T$. Similarly, the columns of **V** are the normalized eigenvectors of the space-covariance matrix $\mathbf{X}^T\mathbf{X}$. The columns of **U** and **V** are orthogonal, so that $\mathbf{U}^T\mathbf{U} = \mathbf{V}^T\mathbf{V} = \mathbf{I}$, where **I** is the unitary matrix [167]. In signal processing applications, the columns of **V** are called principal axes (PAs) which represent the spatial structure of signal harmonics. The projection of **X** along **U** (the product of **US**) defines the matrix of principal components (PCs). The columns of PC matrix carry the time information of the corresponding principal axes. The diagonal elements of matrix **S**, called singular values (SVs), are the square root of the non-zero eigenvalues obtained from solving the covariance ma-

trices $\mathbf{X}\mathbf{X}^T$ and $\mathbf{X}^T\mathbf{X}$. The SVs are stored in descending order proportional to the amplitude of the signal harmonics [168].

The output of SVD analysis can be examined by assuming a simple sinusoidal signal representing a traveling wave in a form of $x(\theta, t) = \cos(m\theta - 2\pi ft)$. The data matrix of a signal $x(\theta, t)$ carrying a spatial harmonic m and collected at N equidistant angles (i.e. $\theta_j = \frac{2\pi(j-1)}{N}$) can be written in the form of equation:

$$X_{ij} = \frac{1}{\sqrt{M}} \cos\left[\frac{2\pi m}{N}(j-1) - 2\pi f t_s(i-1)\right] \tag{3.80}$$

where i and j are the row and column indices. The signal $x(\theta\,, t)$ is sampled every t_s and normalized by a factor of $\frac{1}{\sqrt{M}}$. Equation 3.80 generates the following $M \times N$ data matrix:

$$\mathbf{X} = \frac{1}{\sqrt{M}} \begin{pmatrix} x_1(0) & \cdots & x_N(0) \\ \vdots & \ddots & \vdots \\ x_1((M-1)t_s) & \cdots & x_N((M-1)t_s) \end{pmatrix} \tag{3.81}$$

SVD decomposes the matrix $\mathbf{X}$ into three matrices $\mathbf{U}\mathbf{S}\mathbf{V}^T$. The diagonal matrix $\mathbf{S}$ contains two dominant SVs with equal values of $\frac{\sqrt{N}}{2}$. The dominant SVs correspond to the sine and cosine coefficients of the spatial mode m. The spatial structure of m is determined by the first two PAs in the $\mathbf{V}$ matrix. The PAs lag each other with a phase difference of $\frac{\pi}{2}$:

$$\begin{aligned} v_i^{(1)} &= \sqrt{\frac{2}{N}} \cos\left[\frac{2\pi m}{N}(i-1)\right] \\ v_i^{(2)} &= \sqrt{\frac{2}{N}} \sin\left[\frac{2\pi m}{N}(i-1)\right] \end{aligned} \tag{3.82}$$

The first two PCs (divided by their corresponding SVs) represent the time evolution of the spatial mode m. The PCs also lag each other by a phase angle of $\frac{\pi}{2}$:

$$u_i^{(1)} = \sqrt{\frac{2}{M}} \cos\left[2\pi f t_s(i-1)\right]$$

$$u_i^{(2)} = \sqrt{\frac{2}{M}} \sin\left[2\pi f t_s (i-1)\right] \tag{3.83}$$

The remainder of SVs are very small compared with the two dominant SVs. The small SVs are usually below the noise level and, therefore, can be discarded.

Chapter 4

Experimental Setup

4.1 Introduction

Plasma parameters and instabilities are monitored in STOR-M by various diagnostics. The magnetic perturbations are measured outside the vacuum chamber using arrays of discrete Mirnov coils. The SXR emissions associated with the internal MHD instabilities are monitored by two SXR cameras inserted through vertical and horizontal ports on STOR-M. The toroidal flow measurements of impurity ions are carried out using an IDS system. A rake probe array consisting of 16 Langmuir probes is used for measuring plasma parameters, such as the electron density and temperature, in the edge and SOL regions. A new magnetic probe array is assembled and calibrated to study the plasma response to external fields. This chapter describes the general layout of diagnostics used in this research along with the main components of the RMP system.

4.2 Mirnov Arrays

The magnetic perturbations are monitored in STOR-M by 32 discrete Mirnov probes. Each probe consists of 200 turns of 30 AWG magnet wire with a cross-section of 0.25 $\times$ 3 cm^2. The Mirnov probes are approximately 1 cm long, corresponding to an angular spread of 3.3°. The probes are arranged into four poloidal arrays. The coils are wound around a teflon strip with a

length of 108 cm, corresponding to the circumference of a circle with a radius of 17.2 cm. Two of the poloidal arrays consist of 12 Mirnov coils with a poloidal separation of 30°. The arrays are mounted on thin bellows with a thickness of 0.5 mm and toroidally apart by 180°. The spatial resolution of arrays can resolve poloidal mode numbers up to $m = 6$ (= total no. of coils/2).

The remaining 8 probes are wound on two additional arrays (4 coils per array), allowing the measurement of poloidal modes up to $m = 2$. The magnetic probes are evenly spaced by 90°. The additional arrays are 90° away from the bellows and installed on the chamber wall with a thickness of 4 mm. The toroidal modes can be identified by four sets of toroidal arrays. Each toroidal array consists of 4 Mirnov coils toroidally separated by 90°. The outboard toroidal array is often used to detect the toroidal mode numbers $n = 1$ and $n = 2$ which are the dominant toroidal modes in STOR-M [169]. Figure 4.1 shows a schematic of Mirnov arrays installation in STOR-M.

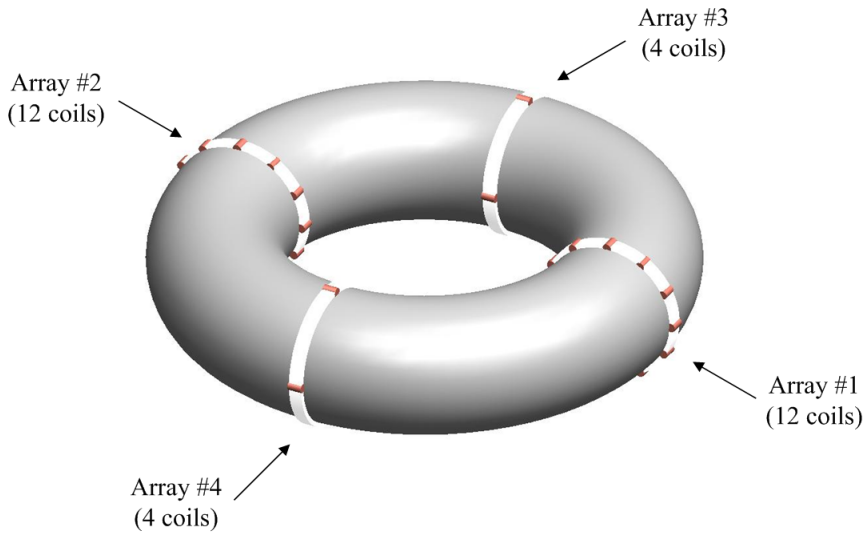

Figure 4.1: The arrangement of Mirnov arrays in STOR-M.

Mirnov coils detect the perturbations in the poloidal magnetic field. The perturbed poloidal field $\tilde{B}_\theta(\theta, t)$ detected at N poloidal locations can be written as a sum of poloidal Fourier harmonics [170]:

$$\tilde{B}_\theta(\theta, t) = \frac{C_0(t)}{2} + \sum_{m=1}^{N/2} [C_m(t)\cos(m\theta) + S_m(t)\sin(m\theta)] \tag{4.1}$$

where the factor $\frac{C_0(t)}{2}$ is associated with the unperturbed poloidal field $B_{\theta,0}$. The numerical methods

mentioned in Sections 3.7 and 3.8 are used to extract the dominant harmonics and their corresponding frequencies from the raw Mirnov signals. The Mirnov signals are terminated by 50 Ω resistors and transmitted to an aluminium break-out box via a 1.5 m flat-twisted ribbon cable. The signals are sent across the tokamak room to a multichannel data acquisition system through 50 Ω coaxial cables. The data acquisition system consists of 5 National Instruments digitizer cards (NI PXI-6133), each with 14-bit resolution. There are 8 analog input channels for each card with a maximum sampling rate of 3 MS$/$s per channel [171].

4.3 SXR System

The internal instabilities of a tokamak plasma can be studied by monitoring the SXR radiation emitted from the plasma core. MHD perturbations near the $q = 1$ surface are associated with the internal kink instability and characterized by relaxations with a fast collapse or crash of the central plasma pressure followed by a gradual build-up phase. The SXR radiation is produced by the thermal electrons emitted from the plasma. The SXR radiation consists of the bremsstrahlung and recombination radiation of partially ionized impurities. The SXR energy is usually in the range of 0.1-10 keV. The radiation intensity is sensitive to the electron density n_e, the electron temperature T_e and the concentration of impurities. The perturbations in the electron density $\tilde{n}_e$ and temperature $\tilde{T}_e$ appear in the SXR signals as sawtooth oscillations superimposed on the sawtooth crashes. The sawtooth oscillations can be observed by photodiodes installed outside the plasma [172].

The SXR system in STOR-M consists of two miniature pinhole cameras. Each SXR camera consists of a 20-channel photodiode array (IRD AXUV-20EL) and a rectangular slit with a size of 1 $\times$ 4 mm^2. The photodiode arrays are located 1 cm away from the entrance slit. The SXR radiation level is monitored by a total of 24 fan-like lines of sight. The size and location of the pinhole is optimized to provide a fine spatial resolution with minimal overlapping between the nearby lines of sight. Aluminum foils with a thickness of 1.8 μm are placed at each camera pinhole to filter out the low energy photons (i.e. visible light) from the high energy spectrum. The SXR cameras are

inserted through small circular horizonal and vertical ports separated by 90°.

The photodiode current is preamplified using a set of IRD AMP16 preamplifiers with fixed gains of 10^5 V/A. The photodiodes are arranged in a biased common anode configuration and connected to the preamplifiers using coaxial cables with a length of 1 m. The preamplified signals are further amplified and transmitted to the data acquisition system via homemade amplifiers with variable gains [173]. The lines of sight of SXR cameras over the plasma cross-section are illustrated in Figure 4.2.

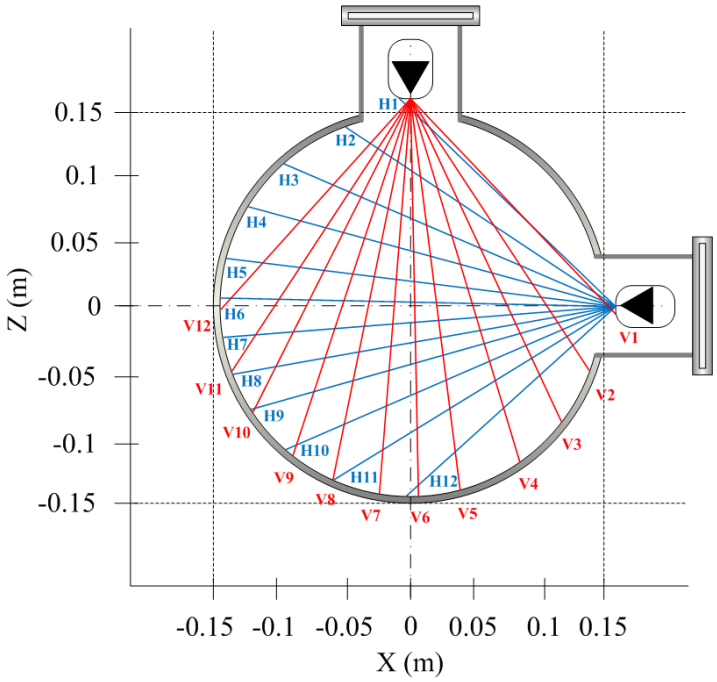

Figure 4.2: Schematic of SXR cameras in STOR-M.

4.4 IDS System

The toroidal flow velocity of impurity ions is measured using an IDS system developed and installed recently in STOR-M [98]. The IDS system uses various emission lines from intrinsic impurities, such as carbon and oxygen emission lines, for the plasma flow measurements. The velocity resolution of the IDS system is in the range of 1-2 km/s. The IDS system consists of fiber optics with collimators, a spectrometer, a cylindrical rod lens and a 16-channel PMT array.

The Czerny-Turner spectrometer (SPEX 1702) consists of an entrance slit, a reflection grating (1200 lines/mm), and two concave mirrors with a focal length of 0.75 m. The spectrometer has an aperture of $f/7.0$ and operates in the range of 0-15000 Å with a mechanical resolution of 0.3 Å. Figure 4.3 shows a schematic layout of the IDS system in STOR-M.

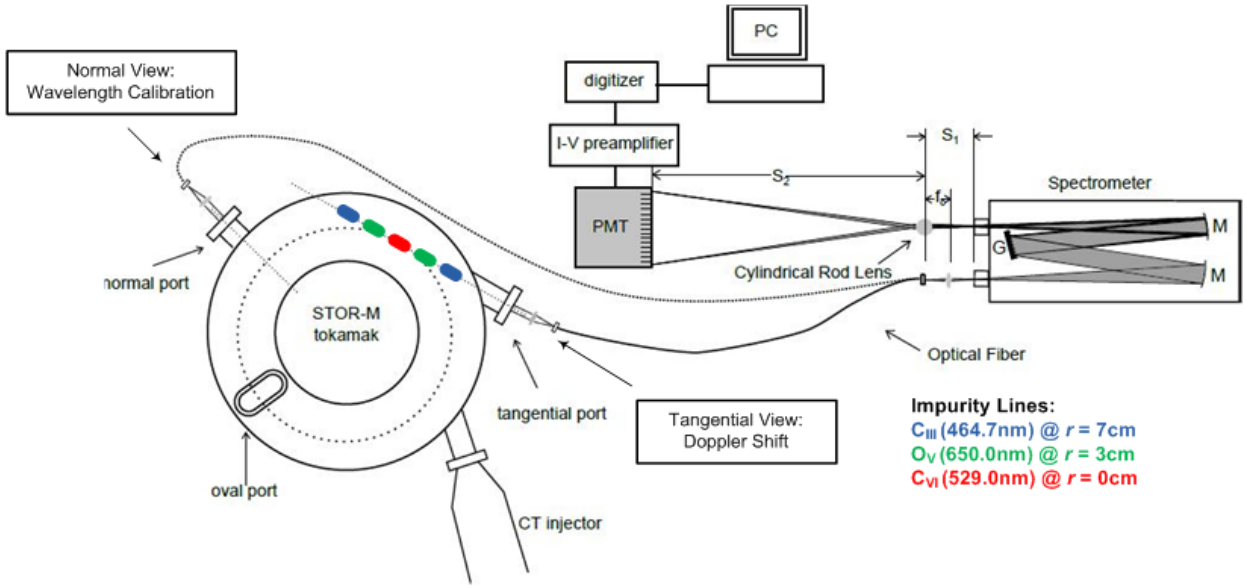

Figure 4.3: Layout of the IDS system in STOR-M.

The IDS system uses tangential, normal and vertical ports for the flow measurements. The ports are equipped with quartz windows to allow the plasma radiation to pass through. The vertical port is used for measuring the radial distribution of the impurity spectral lines. The emission lines collected from the tangential port are used for estimating the Doppler shift, whereas the lines measured from the normal port serve as a reference of the unshifted wavelengths. A collimator with a diameter of 25.4 mm and an aperture of $f/2.0$ collects the light from the plasma. The dispersed spectrum is transmitted to the spectrometer via optical fiber guide and the image of spectrum is magnified by a cylindrical lens. A 16-channel PMT array is used to record the spectrum. The PMT array is enclosed in an aluminum housing. The PMT signals are amplified using current amplifier circuits and sent to the data acquisition system using coaxial cables.

The radial distribution of impurity emissivity is measured through the vertical port by changing the vertical line of sight between discharges. The Abel inversion technique is used to reconstruct

the radial profile from the line-integrated emission signals. Figure 4.4 shows the radial profiles of C_{III} (464.7 nm), O_V (650.0 nm), and C_{VI} (529.0 nm) impurity lines which have different ionization states and radial locations. The radial profile of C_{III} emission line is peaked at $r = 7$ cm, the O_V profile is peaked near $r = 3$ cm, while the C_{VI} profile is peaked at the plasma center ($r = 0$). These emission lines are chosen for the flow measurements in STOR-M because of their high brightness.

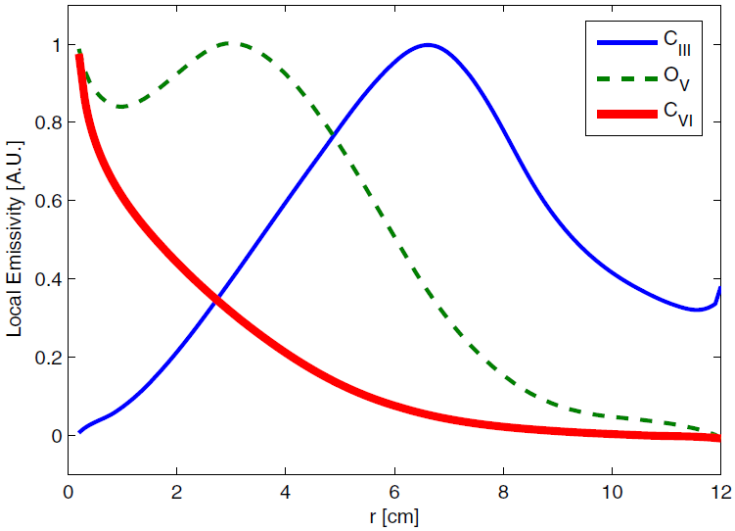

Figure 4.4: The normalized radial profiles of C_{III}, O_V and C_{VI} line emissions [174].

4.5 Rake Probe

A rake probe is an array of Langmuir probes that measures the local plasma properties at different spatial locations simultaneously. The Langmuir probe is a metal tip biased at a fixed voltage or unbiased at the so-called floating potential. The current-voltage (I-V) characteristic curve of a Langmuir probe is obtained by sweeping the biasing voltage and collecting the current as shown in Figure 4.5. The Langmuir probe measures the electron temperature T_e, the electron density n_e, the floating potential V_f and the plasma potential V_p in the plasma. The usage of Langmuir probes is restricted to low temperature plasmas or the edge region of hot plasmas to avoid damaging the probes. The total current collected by the Langmuir probe can be expressed by the sum of the electron and ion currents:

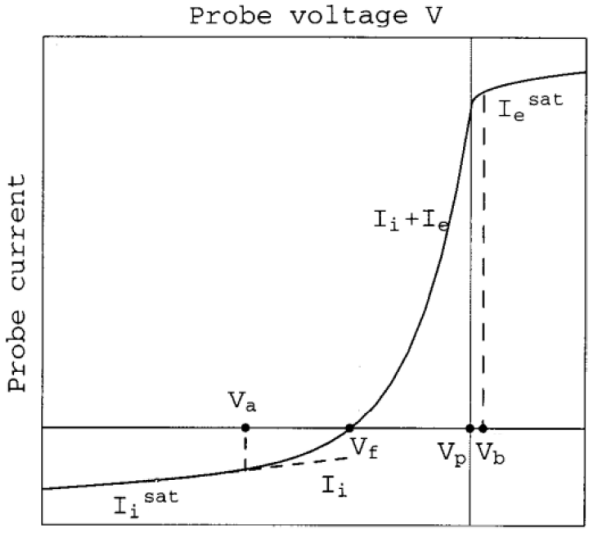

Figure 4.5: The I-V characteristic curve of Langmuir probe [175].

$$I = I_{si}\left(\sqrt{\frac{M}{2\pi m}}e^{e(V_b-V_p)/k_BT_e} - 1\right) \tag{4.2}$$

where V_b and V_p are the electrode and the plasma potentials with respect to ground, and k_B is the Boltzmann constant. The ion saturation current I_{si} is collected by biasing the electrode negatively with respect to the plasma. The ion saturation current is given by:

$$I_{si} = e^{-\frac{1}{2}}en_eA_{\text{eff}}\sqrt{\frac{k_BT_e}{M}} \tag{4.3}$$

where A_{eff} is the effective surface area of the probe. The factor $e^{-\frac{1}{2}}$ accounts for the pre-sheath density reduction and depends on the ratio between the ion and electron temperatures [176]. The floating potential V_f is defined by the plasma potential when there is no current flowing in the electrode ($I = 0$):

$$V_f = \frac{k_BT_e}{2e}\ln\left(\frac{M}{2\pi m}\right) \tag{4.4}$$

The rake probe used in STOR-M consists of 16 Langmuir probes arranged into two rows with poloidal separation of 2.5 mm. Each row includes 8 pins radially separated by 2.5 mm. The pins are made of tungsten wire with a diameter of 0.5 mm and an exposed length of 4 mm. The pins

are 9 mm long and tightly fit in a grid of single-in-line (SIL) sockets inside the probe head. The sockets have 16 leads to connect the pins to electric wires.

As shown in Figure 4.6, the probe head is made of boron nitride with a diameter of 10 mm and a length of 26.7 mm. The head is attached to a 75 mm long alumina rod with inner and outer diameters of 5 mm and 6.35 mm, respectively. The rod is inserted 5 mm into the probe head from one end and attached to a stainless steel mount from the other end. The mount is screwed to a linear-rotary feedthrough which allows the innermost pair of pins to be moved between minor radii 180 mm and 80 mm. The whole probe assembly is secured with Torr Seal epoxy.

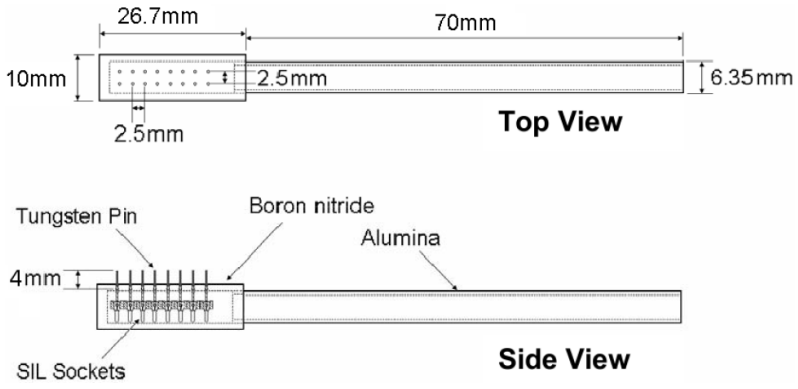

Figure 4.6: Top and side view of the rake probe used in STOR-M [177].

4.6 RMP System

4.6.1 RMP Coils

The RMP system in STOR-M consists of RMP coils, power supplies, trigger circuits, IGBT and SCR switches. The RMP coil is a 30 m long wire formed by two sets of 8 AWG wires with an ($l = 2$, $n = 1$) configuration connected in series. The two sets of helical windings are poloidally separated by 90° illustrated in Figure 4.7(a) by the blue and red lines. The coils are externally wound and secured against the outer surface of the vacuum chamber at a radius of 17 cm. The total resistance and inductance of the RMP windings are about 100 mΩ and 15 μH, respectively.

The RMP fields are produced by driving a current pulse I_{RMP} with equal magnitudes and oppo-

site directions through the coil sets. The resonant interaction can be achieved between RMP and the (2, 1) magnetic islands by matching the helicity direction (pitch angle direction) of the helical coil with the helicity of the targeted islands. The helicity of (2, 1) island is defined by the directions of I_p and B_ϕ. In STOR-M, the resonant condition is satisfied when the direction of I_p is counter-clockwise and B_ϕ is clockwise (viewed from the top). The (2, 1) magnetic islands developed along the twisted magnetic field lines are indicated by the black line in Figure 4.7(a). The non-resonant RMP (NRMP) configuration can be archived by reversing the direction of plasma current. The reversal of plasma current causes a mismatch between the winding direction of the RMP coils and the helicity direction of the (2, 1) islands.

The RMP coils produce a mode spectrum with a dominant mode number of ($m = 2$, $n = 1$). The mode spectrum is obtained by firing a fast current pulse in the RMP coils and collecting the corresponding signals using Mirnov arrays. Figure 4.7(b) shows the normalized magnitude of each poloidal mode calculated by the spatial Fourier series. The dominant mode $m = 2$ represents about 44% of the total spectrum amplitude. The poloidal mode spectrum also consists of other sideband modes, all with dominant $n = 1$ toroidal mode. The sideband modes are found to be $m = 1$ (15%), $m = 3$ (22%) and $m = 4$ (12%) modes.

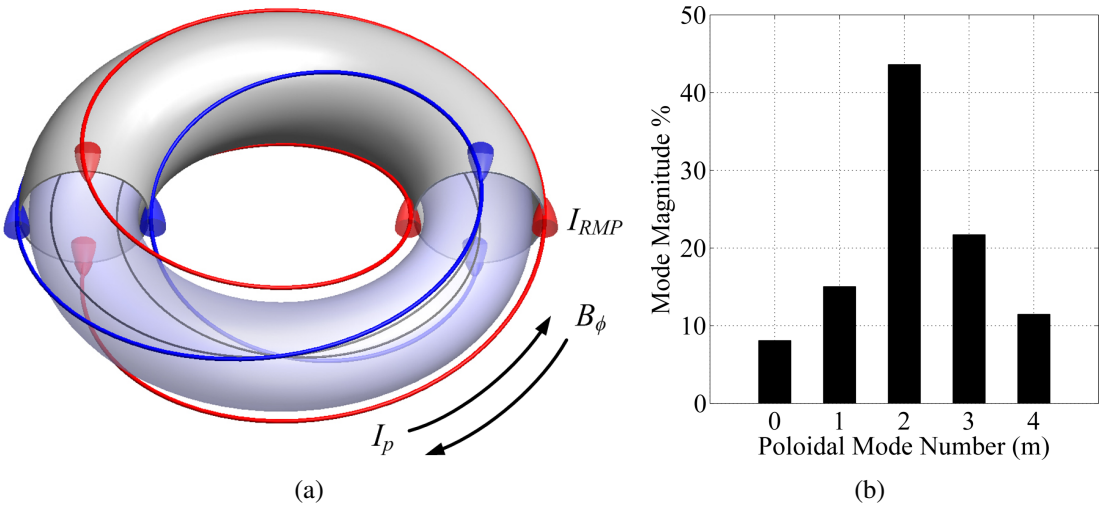

(a) (b)

Figure 4.7: (a) The layout of RMP coils in STOR-M. The blue and red lines illustrate the helical configuration of RMP coils used to control (2, 1) magnetic islands (the black line). (b) The poloidal mode spectrum generated by the RMP field at the plasma edge.

The purpose of generating the RMP field using two sets of helical windings is to avoid an unnecessary coupling between the RMP coils and other toroidal coils of the tokamak, such as the ohmic heating coils and the vertical field coils for the position control. The RMP field can be produced by using only one coil set. However, the single coil configuration couples with tokamak fields, inducing electromotive forces across the RMP coils and driving unwanted currents either with or against the intended I_{RMP} direction. Moreover, the RMP windings act like a transformer, driving the plasma current through transformer actions, which alters the equilibrium plasma. Therefore, it is advantageous to use two sets of windings with opposite polarities to cancel out the induction currents as well as to minimize the transformer effect of other coils on the RMP windings.

4.6.2 RMP Circuit

Figure 4.8 shows a schematic of the RMP circuit used in STOR-M. The RMP circuit produces two types of RMP fields: slow RMP (SRMP) and fast RMP (FRMP) fields. The SRMP field is generated by two capacitor banks. The first bank (50 mF, 450 V) is used to achieve a fast current ramp-up for the SRMP pulse, whereas the second bank (420 mF, 100 V) maintains the current flat-top. The power supplies consisting of variacs, isolation transformers, and bridge rectifiers can charge the banks up to 200 V. However, the voltage on the second bank should not exceed a rated voltage of 100 V. The capacitor banks are equipped with diodes to prevent the banks from charging each other. The banks are designed to be charged simultaneously with the OH banks in STOR-M. The amplitude of the SRMP pulse depends on the voltages of the capacitor banks. The first and second banks are typically charged at voltages of 100 V and 90 V to produce a nearly constant 1 kA SRMP pulse with a duration of 8 ms. The current in the circuit is limited by the IGBT switch.

The FRMP power supply consists of a variac, a 1:2 step-up transformer, a bridge rectifier, and an additional capacitor bank (2.5 mF, 450 V). The FRMP bank and the OH banks are also synchronized to charge together. The FRMP bank can be charged to a voltage of 400 V to produce a 1.5 kA FRMP pulse for about 0.5 ms. The FRMP pulse is typically fired during the SRMP flat-top. The FRMP circuit is equipped with a diode to prevent the RMP current from ringing. The

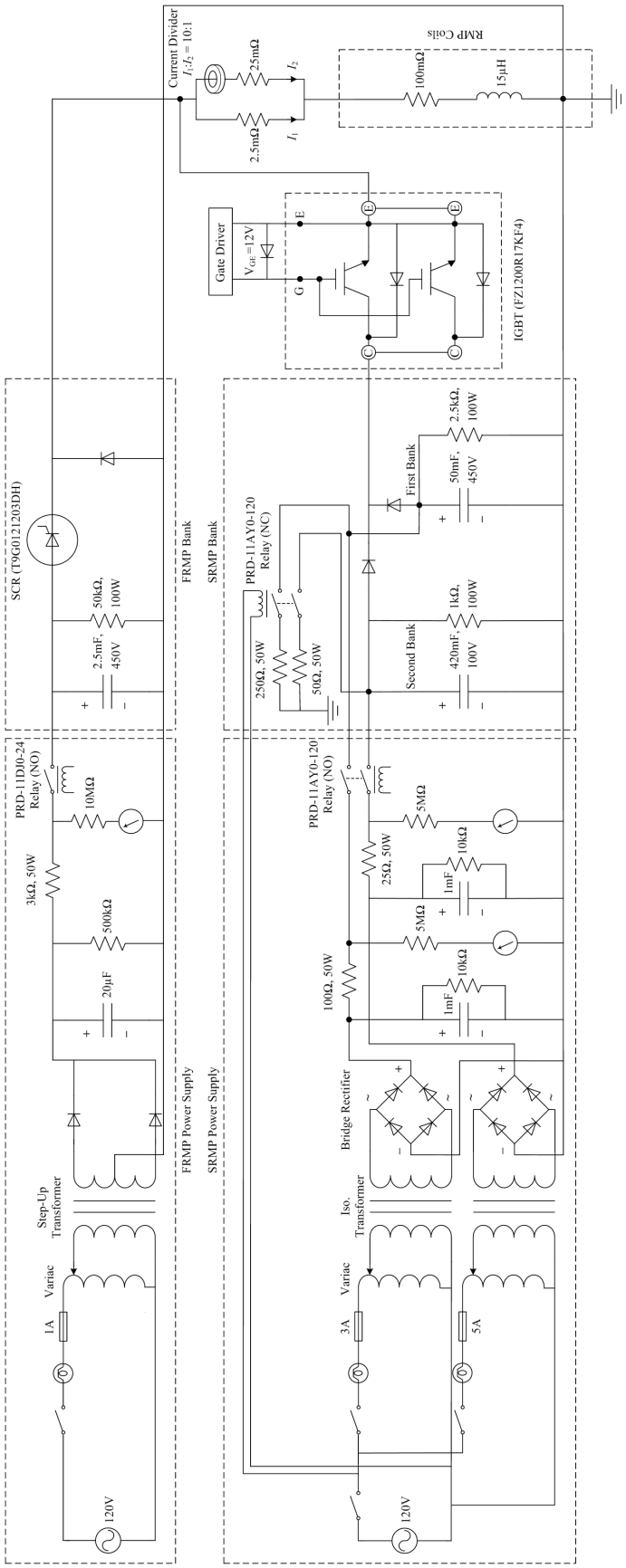

Figure 4.8: RMP circuit in STOR-M.

RMP current generated by the SRMP and FRMP power supplies is monitored by a commercial Rogowski coil with a calibration factor of 100 A/V positioned at the low branch of a 10:1 current divider. The RMP current waveform is transmitted to the data acquisition system using a coaxial cable and attenuated by a standard 10× BNC attenuator.

The SRMP pulse is gated by a 1200 A, 1700 V Eupec IGBT module (model no. FZ1200R17KF4). The IGBT switch is connected to an isolated trigger circuit shown in Figure 4.9. The IGBT circuit is triggered by an optical signal sent from a computer-controlled pulse generator located in the control room. The output signal of the circuit is about 12 V, which is sufficient for the gate-emitter voltage of IGBT (8-20 V) [178]. The pulse width of the output signal can be adjusted by a 100 kΩ variable resistor connected to a 555 timer chip. The trigger circuit generates an output signal with a duration up to 26 ms. The IGBT module is mounted on a heat sink and shielded in a metal housing. The IGBT module can be operated at twice the rated current limit as long as the module temperature does not exceed the rated temperature (i.e. 150 C°). The increase in the IGBT temperature is determined by the pulse width and the repetitive rate of RMP, which are relatively small in the RMP experiments conducted in STOR-M (single RMP pulse with a maximum duration of 8 ms).

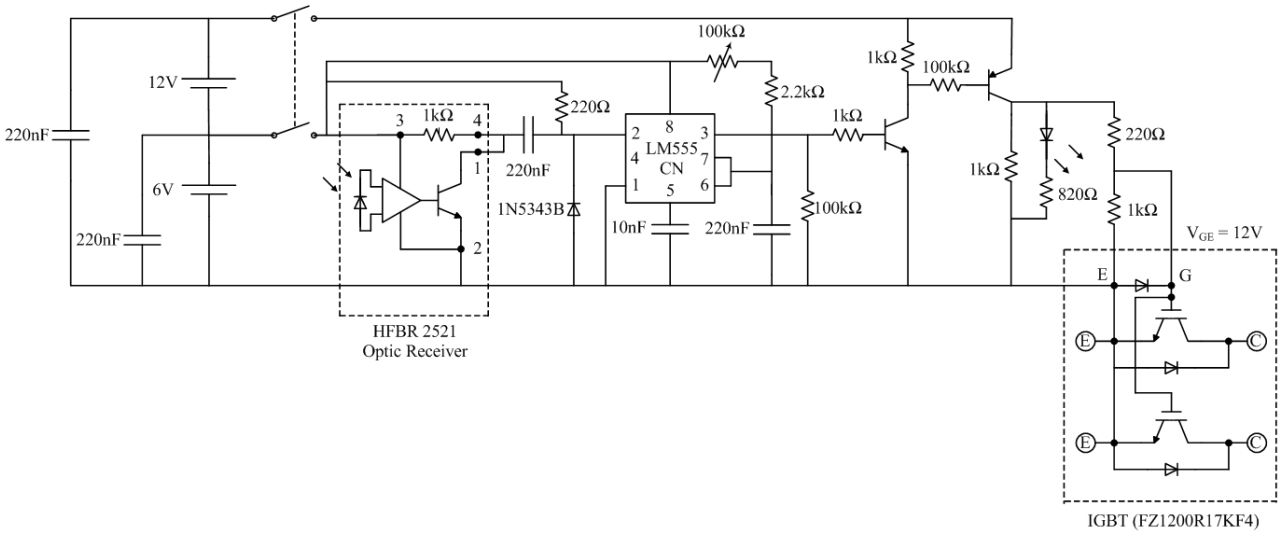

Figure 4.9: IGBT trigger circuit.

The FRMP bank is discharged through a Powerex SCR switch clamped with two aluminum busbars and secured by a homemade fiberglass clamps. The SCR module (model no. T9G0121203DH)

is rated for a voltage of 2400 V and a single pulse current of 27 kA [179]. The typical gate voltage of SCR is about 3 V, which is provided by a gate driver shown in Figure 4.10. The gate driver receives the trigger signal from the control room via optical fiber. The gate driver circuit is enclosed in an aluminum box and isolated from the high voltage components.

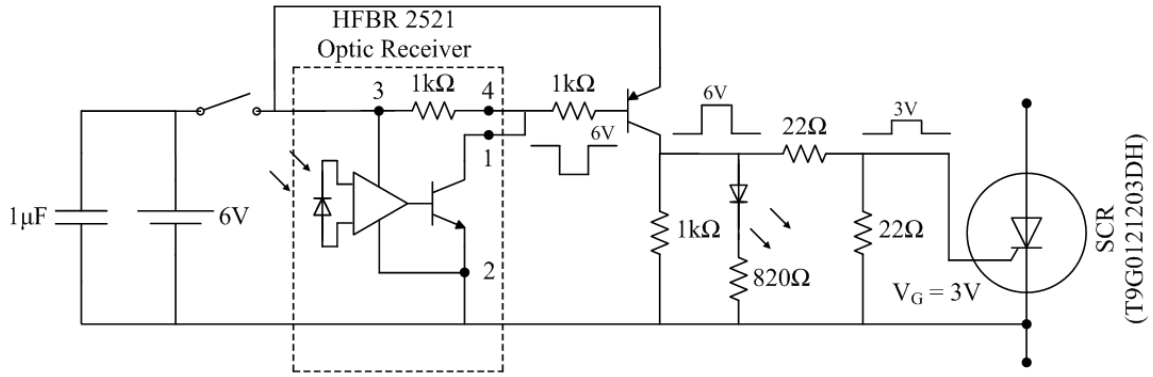

Figure 4.10: SCR gate driver.

A double RMP (DRMP) pulse is generated by modulating the input trigger signal of the IGBT module using an astable 555 timer circuit. The astable circuit shown in Figure 4.11 is powered by a 6 V battery and triggered by an optical signal sent from the control room. The output signal of the circuit is a square wave alternating between 0 and 6 V. The high and low times of the output signal are adjusted by 1 kΩ variable resistors. The output signal is sent to an optical transmitter connected to the IGBT trigger circuit by an optical cable. The typical DRMP pulse used in STOR-M consists of two consecutive RMP pulses with a length of 3 ms and separated by a 2 ms period.

4.6.3 RMP Circuit Analysis

Circuit analyses have been carried out for the RMP discharges. The RMP discharge circuit in STOR-M can be simplified to a series RLC circuit shown in Figure 4.12. The RLC circuit consists of two sub-circuits. A circuit consisting of first and second banks generates the SRMP current, and the second circuit consisting of a fast bank produces the FRMP current. The SRMP and FRMP circuits are respectively gated by IGBT and SCR switches. The capacitor banks of the SRMP circuit are independently charged to voltages denoted by V_{s1} and V_{s2}. The capacitance of

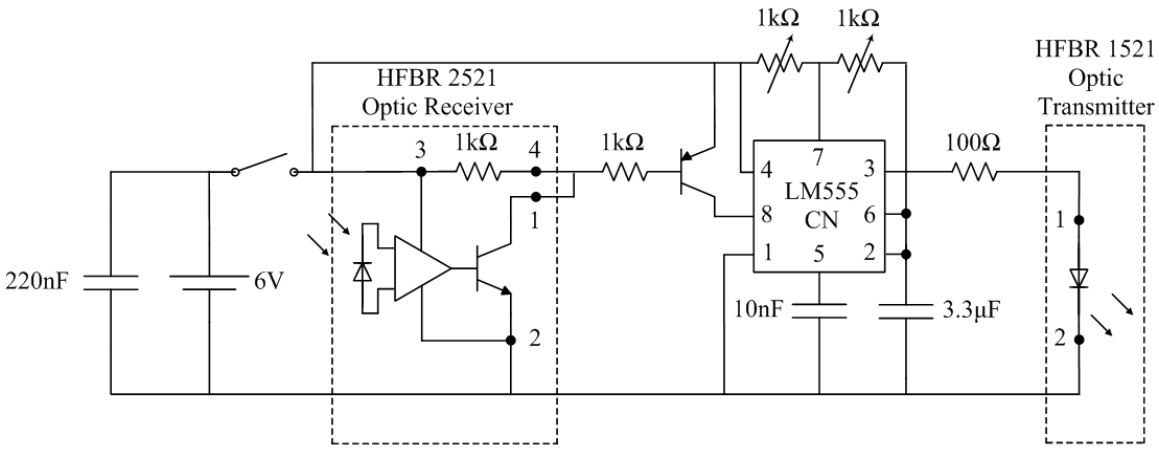

Figure 4.11: Astable timer circuit for the double RMP pulse.

the first and second banks are given by C_{s1} and C_{s2}, respectively. The charging voltage and the capacitance of the fast bank are denoted by V_f and C_f. The capacitor banks in both circuits are connected in parallel when they are all conducting currents, so that the total capacitance is given by $C_{s1} + C_{s2} + C_f$.

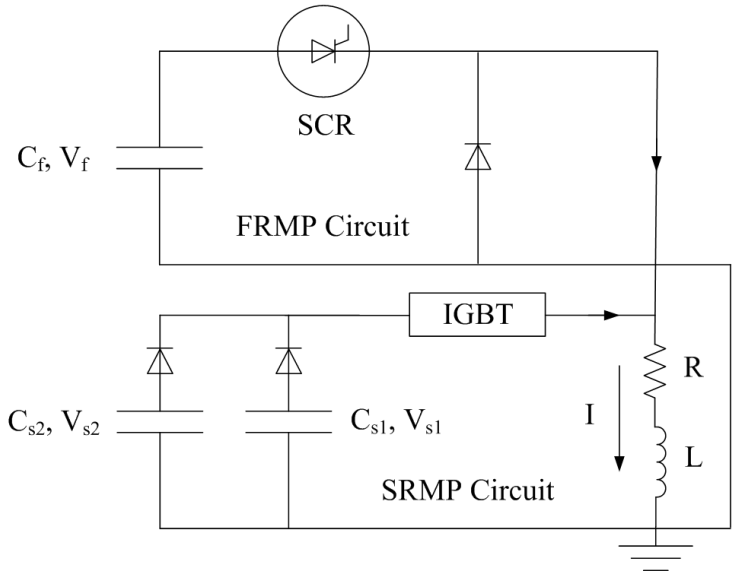

Figure 4.12: RLC circuit of the RMP system.

The governing differential equation of an RLC circuit can be found by substituting the voltages across R, L and C into Kirchhoff's voltage law (KVL). The current equation of a source-free, series

RLC circuit is given by:

$$L\frac{dI}{dt} + RI + \frac{1}{C}\int Idt = 0 \tag{4.5}$$

where L and R are the inductance and resistance of the RMP coil. Differentiating the previous equation leads to:

$$L\frac{d^2I}{dt^2} + R\frac{dI}{dt} + \frac{I}{C} = 0 \tag{4.6}$$

The current I is related to the capacitor(s) voltage V by:

$$I = C\frac{dV}{dt} \tag{4.7}$$

Substituting the above equation into Equation 4.5 and dividing by C yields the voltage equation of the RLC circuit:

$$L\frac{d^2V}{dt^2} + R\frac{dV}{dt} + \frac{V}{C} = 0 \tag{4.8}$$

Equations 4.6 and 4.8 are second-order linear homogeneous equations with a characteristic equation defined by:

$$Lm^2 + Rm + \frac{1}{C} = 0 \tag{4.9}$$

The complementary solution of the characteristic equation is called the natural response of the circuit which depends on the natural frequency m:

$$m_{1,2} = -\frac{R}{2L} \pm \sqrt{\frac{R^2}{4L^2} - \frac{1}{LC}} = -\alpha \pm \sqrt{\alpha^2 - \omega_0^2} \tag{4.10}$$

where α is the damping coefficient and ω_0 is the resonance frequency of the circuit. The damping factor ζ is defined by the ratio of α and ω_0:

$$\zeta = \frac{\alpha}{\omega_0} = \frac{R}{2}\sqrt{\frac{C}{L}} \tag{4.11}$$

The differential equations of the circuit have three different characteristic solutions depending on

the value of ζ. The natural response of the circuit is over-damped when $\zeta > 1$. The general solution of the differential equations is given by:

$$I(t) = A_1 e^{m_1 t} + A_2 e^{m_2 t} \tag{4.12}$$

$$V(t) = B_1 e^{m_1 t} + B_2 e^{m_2 t} \tag{4.13}$$

where the roots m_1 and m_2 are real, distinct and negative. The circuit is critically damped if $\zeta = 1$, so that:

$$I(t) = (A_1 + A_2 t) e^{-\alpha t} \tag{4.14}$$

$$V(t) = (B_1 + B_2 t) e^{-\alpha t} \tag{4.15}$$

The roots of the characteristic equation (Equation 4.9) are negative, real and equal to $-\alpha$. The general solution for an under-damped circuit ($\zeta < 1$) is expressed by:

$$I(t) = (A_1 \cos \omega t + A_2 \sin \omega t) e^{-\alpha t} \tag{4.16}$$

$$V(t) = (B_1 \cos \omega t + B_2 \sin \omega t) e^{-\alpha t} \tag{4.17}$$

which implies that the roots of Equation 4.9 are complex conjugates ($-\alpha \pm i\omega$). The frequency ω is the damped resonance frequency of the circuit defined by:

$$\omega = \sqrt{\frac{1}{LC} - \frac{R^2}{4L^2}} = \sqrt{\omega_0^2 - \alpha^2} \tag{4.18}$$

Figure 4.13 shows an analytical RMP discharge consisting of SRMP and FRMP pulses. At the beginning, the capacitor banks are charged at different voltages, so that $V_f > V_{s1} > V_{s2}$. The first SRMP bank is fired at $t = 0$ to achieve the current ramp-up of SRMP pulse. The voltage V_{s1} drops until $t = t_1$ at which the voltages on the first and second banks are equal ($V_{s1}(t_1) = V_{s2}$). Both capacitor banks discharge together with a total capacitance $C_{s1} + C_{s2}$ until firing the FRMP pulse

at $t = t_2$. Since $V_f > V_{s1} > V_{s2}$, the SRMP circuit stops conducting momentarily. The FRMP pulse rises and drops quickly due to the small capacitance and the high voltage of the fast bank. The voltage of the fast bank (V_f) decreases until $t = t_3$ at which the voltages on all banks are the same. The banks discharge together with a total capacitance $C_{s1} + C_{s2} + C_f$ until turning off the IGBT switch at $t = t_4$. The voltage on the fast bank continues to drop until it reaches zero at $t = t_5$. Since there is no voltage to drive the current in the circuit, the only available current is the induction current produced by the energy stored in the RMP coils. The stored energy decays exponentially at a rate of R/L. The induction current in the circuit is readily defined by:

$$I(t) = I_0 e^{-tR/L} \tag{4.19}$$

The diode in the FRMP circuit reduces the ringing as well as it prevents the fast bank from being charged negatively. Table 4.1 contains the natural response, the initial conditions, and the coefficients of the general solutions for the RMP circuit at different discharge phases.

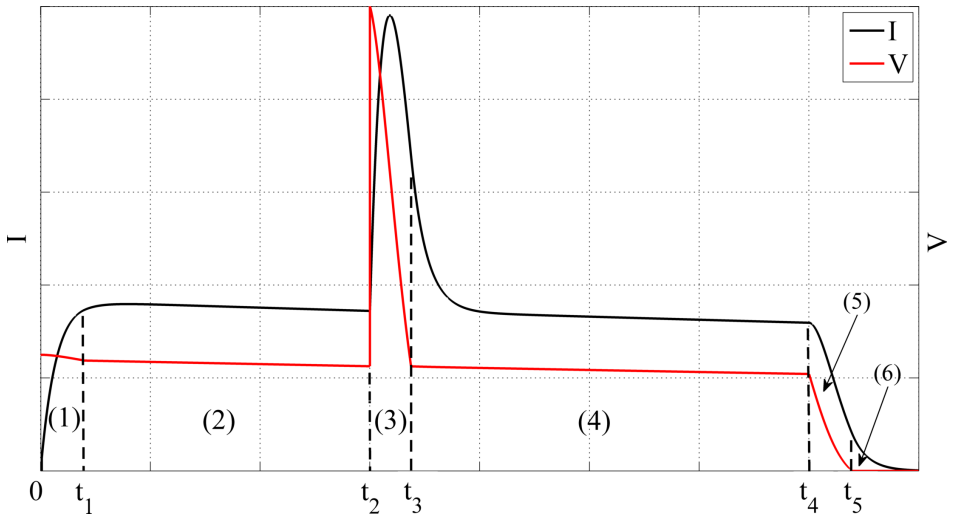

Figure 4.13: RMP discharge waveforms. The numbers 1-6 indicate different discharge phases.

A comparison between analytical and experimental RMP pulses are shown in Figure 4.14. The experimental RMP pulse is about 7 ms long with a FRMP pulse fired around 3 ms. The first and second SRMP banks are charged to respective voltages of 100V and 90V. The FRMP bank is charged to 350V. The amplitude of SRMP current is about 900 A with a rising time of 600 μs. The

Discharge Phase	Circuit Response	Initial Conditions	Solution Coefficients
(1)	Over-Damped	$I(0) = 0$ $\frac{dI}{dt}(0) = \frac{V_{s1}}{L}$ $V(0) = V_{s1}$ $\frac{dV}{dt}(0) = 0$	$A_1 = \frac{V_{s1}}{L(m_1-m_2)}$ $A_2 = \frac{-V_{s1}}{L(m_1-m_2)}$ $B_1 = \frac{m_2 V_{s1}}{m_2-m_1}$ $B_2 = \frac{-m_1 V_{s1}}{m_2-m_1}$
(2)	Over-Damped	$I(0) = I(t_1)$ $\frac{dI}{dt}(0) = \frac{V_{s2}-RI(t_1)}{L}$ $V(0) = V_{s2}$ $\frac{dV}{dt}(0) = \frac{-I(t_1)}{C_{s1}+C_{s2}}$	$A_1 = \frac{V_{s2}-(R+m_2L)I(t_1)}{L(m_1-m_2)}$ $A_2 = I(t_1) - A_1$ $B_1 = \frac{V'(0)-m_2 V_{s2}}{m_1-m_2}$ $B_2 = V_{s2} - B_1$
(3)	Under-Damped	$I(0) = I(t_2)$ $\frac{dI}{dt}(0) = \frac{V_f-RI(t_2)}{L}$ $V(0) = V_f$ $\frac{dV}{dt}(0) = \frac{-I(t_2)}{C_f}$	$A_1 = I(t_2)$ $A_2 = \frac{V_f-(R-\alpha L)I(t_2)}{\omega L}$ $B_1 = V_f$ $B_2 = \frac{V'(0)+\alpha V_f}{\omega}$
(4)	Over-Damped	$I(0) = I(t_3)$ $\frac{dI}{dt}(0) = \frac{V_{s1}(t_2)-RI(t_3)}{L}$ $V(0) = V_{s1}(t_2)$ $\frac{dV}{dt}(0) = \frac{-I(t_3)}{C_{s1}+C_{s2}+C_f}$	$A_1 = \frac{V_{s1}(t_2)-(R+m_2L)I(t_3)}{L(m_1-m_2)}$ $A_2 = I(t_3) - A_1$ $B_1 = \frac{V'(0)-m_2 V_f(t_3)}{m_1-m_2}$ $B_2 = V_{s1}(t_2) - B_1$
(5)	Under-Damped	$I(0) = I(t_4)$ $\frac{dI}{dt}(0) = \frac{V_f(t_4)-RI(t_4)}{L}$ $V(0) = V_f(t_4)$ $\frac{dV}{dt}(0) = \frac{-I(t_4)}{C_f}$	$A_1 = I(t_4)$ $A_2 = \frac{V_f(t_4)-(R-\alpha L)I(t_4)}{\omega L}$ $B_1 = V_f(t_4)$ $B_2 = \frac{V'(0)+\alpha V_f(t_4)}{\omega}$
(6)	RL Discharge	$I(0) = I(t_5)$ $V(0) = 0$	–

Table 4.1: Natural response, initial conditions, and solution coefficients of the RMP circuit at different discharge phases.

SRMP current drops roughly by 100 A ($\sim 12\%$) during the 7 ms pulse duration. The FRMP pulse is about 0.5 ms long with a peak current of 1.3 kA and a rising time of 80 μs.

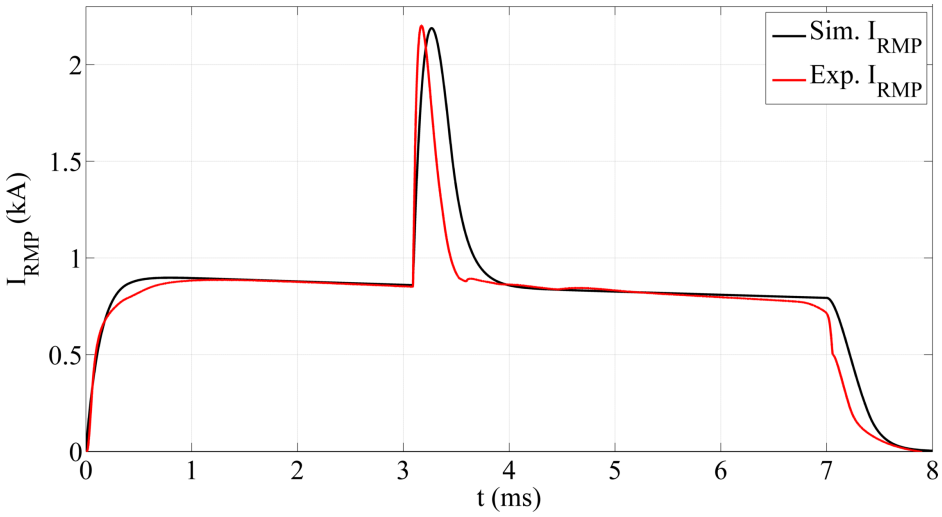

Figure 4.14: Comparison between analytical and experimental RMP current discharges.

4.7 Internal Magnetic Probe Array

The measurements of magnetic fluctuations are conducted in STOR-M using a movable internal magnetic probe array. The internal array consists of 4 miniature magnetic probes oriented in the poloidal direction to measure the poloidal magnetic field at different radial locations. Each probe consists of 50 turns of 32 AWG magnet wire with a cross section of 5 $\times$ 6 mm^2. The probes are 3 mm long and radially separated from center to center by 1 cm. The resistance and the inductance of the probes are around 1 Ω and 4.5 μH, respectively. The cutoff frequency of the probes is about 35 kHz. The cutoff frequency is the frequency at which the probe attenuates the signal to half its original amplitude. The cutoff frequency f_c is calculated by the following relation:

$$f_c = \frac{R}{2\pi L} \tag{4.20}$$

The probe coils are wound around a teflon rod with a diameter of 6 mm and a length of 72.5 mm. The array is center bored from one end to feed through the magnet wires from the coils. The

bore is 25 mm long and 3 mm in diameter. Each pair of magnet wires is twisted around each other to reduce the pickup noise. The twisted pairs of wires are insulated from each other by flexible teflon tubes. The array is inserted into a 65 mm tube closed on one end to protect the probes from the hot plasma. The tube is made of alumina ceramic with inner and outer diameters of 7 mm and 9 mm. The schematic design of the internal probe array and the alumina tube are shown in Figure 4.15.

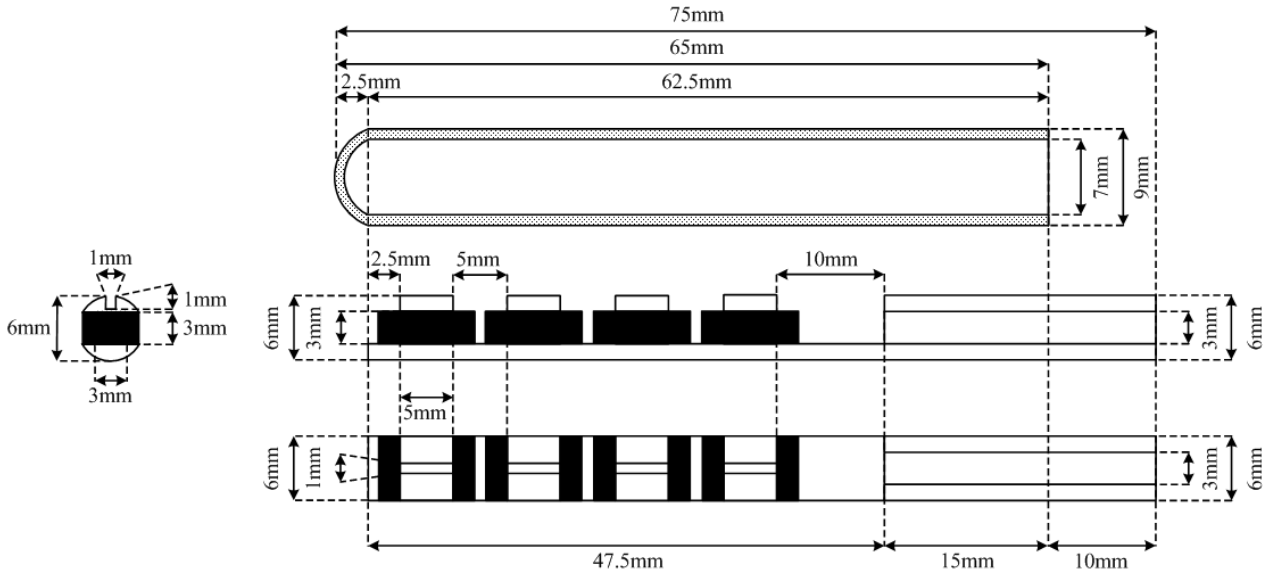

Figure 4.15: Schematic of the internal probe array and the alumina tube.

The probe array is attached to a stainless steel cylinder with Torr Seal epoxy. The cylinder is fixed to the array mount with a machine screw. The array mount consists of a linear-rotary manipulator and a circular 8-pin electrical feedthrough welded to a flange adapter. Each pair of pins is connected to one probe on the vacuum side and a BNC connector on the other side. The array mount is equipped with a stainless steel bellows to reduce the mechanical stresses and vibrations. The array assembly is mechanically supported by two aluminum brackets attached to the STOR-M structure. The array mount allows the innermost probe to be moved between minor radii 180 mm and 80 mm. The radial positions of probes can be adjusted with a manual dial. The probe array is inserted from the low-field side of STOR-M through a horizontal port. The signals collected by the probes are transmitted across the tokamak room to the data acquisition system via coaxial cables.

Due to the high impedance of the data acquisition system ($\sim$ 1 MΩ), it is important to terminate the signals by 50 Ω resistors installed parallel to the digitizers to avoid any reflection in the signals. Figure 4.16 shows a photograph and installation of the internal probe array in STOR-M.

The magnetic probes are calibrated using the FRMP power supply. The current generated by the power supply passes through a 4 m long aluminium rod with a radius of 0.5 cm. The rod is aligned parallel to the magnetic probes and connected to a inductor used to produce the desired current pulse waveform for calibration. The distance between the rod and the probes is 13 cm. The current passing through the rod induces an azimuthal magnetic field on the probes with the same amplitude. The azimuthal magnetic field B_θ is related to the current I by:

$$B_\theta(r) = \frac{\mu_0 I}{2\pi r} \tag{4.21}$$

where r is the distance between the aluminum rod and the probes. The power supply is charged to a voltage of 400 V and fired manually using a hand-held trigger. The current waveform is monitored by a commercial Rogowski coil mounted on a 10:1 current divider. Several discharges are performed for the same distance between the rod and the probes (r = 13 cm). The signals picked up by the probes are collected simultaneously by the data acquisition system and integrated numerically using MATLAB. The waveforms of the source current/magnetic field and the integrated signals of magnetic probes are shown in Figure 4.17. The innermost probe in the array is denoted by P1, whereas the outermost probe is labelled P4. There is a different response time between the current waveform collected by the Rogowski coil and the array signals. The time delay in the array signals ($\sim$ 70-200 μs) might be caused by either the slow response time of probes or the numerical integration of signals. This delay affects the measurements of RMP penetration as it will be shown later in Section 5.6.

Similar calibration discharges are carried out for 4 other distances (15, 17, 19, and 21 cm). The distance between the rod and the probes is increased incrementally by 2 cm and the calibration procedure is repeated for every new distance. The absolute calibration factor of each probe is calculated by dividing the source field over the integrated probe signal and taking the mean value at

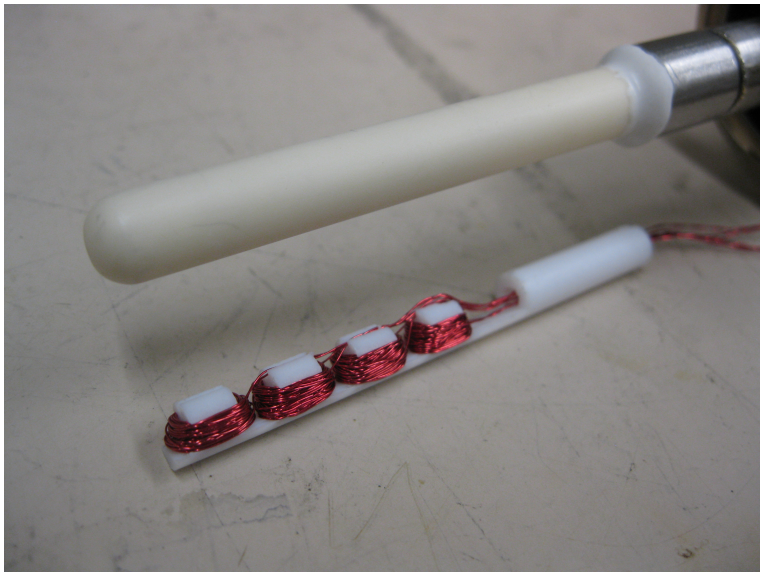

(a) Photograph of the internal probe array (assembled) and a spare coil assembly.

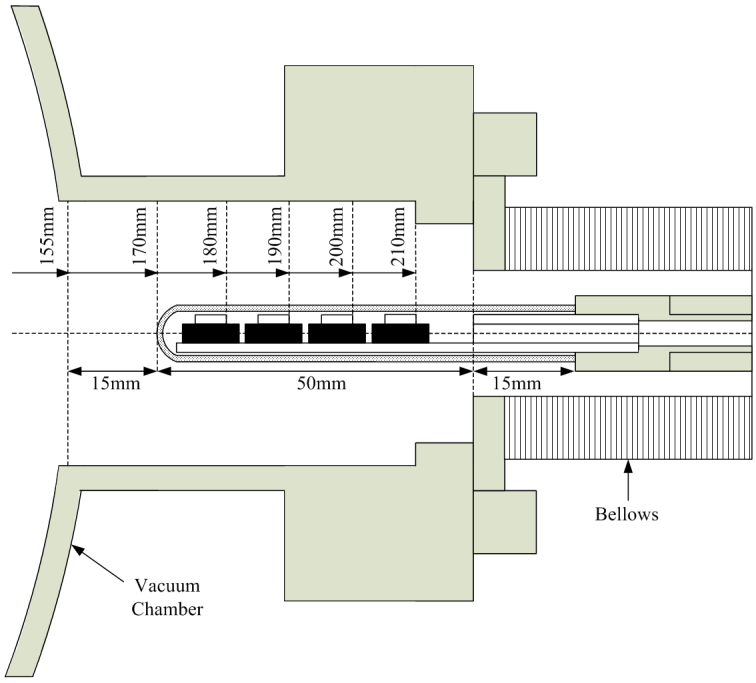

(b) Installation of the internal probe array in STOR-M.

Figure 4.16: Photograph and installation of the internal probe array in STOR-M.

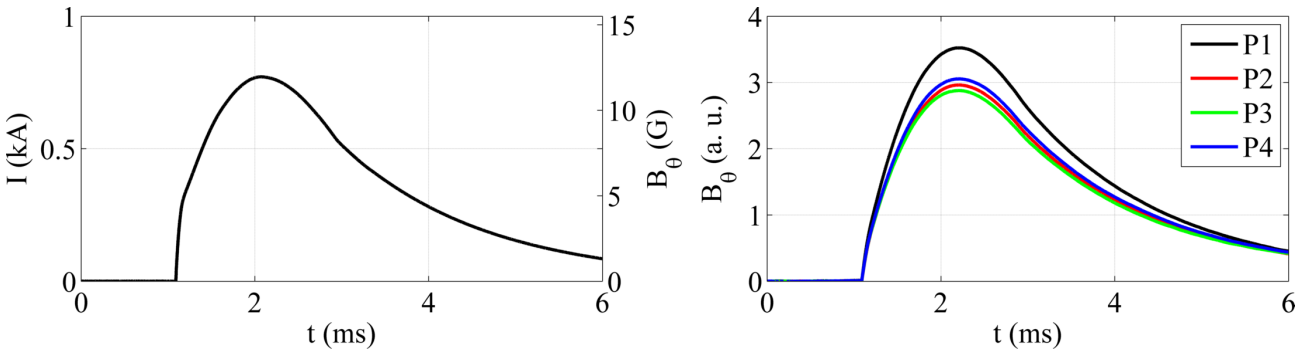

Figure 4.17: (Left) The current/azimuthal field waveform from the current source. (Right) The integrated signals of the internal probes before the calibration. The distance between the current source and the probes is 13 cm.

all distances. The error bars of each probe are estimated by the standard deviation of the measured field at all distances. The absolute calibration factors of the probes are listed in Table 4.2.

Probe	Calibration Factor (G/V)
P1	3.5082 ± 0.1106
P2	4.1654 ± 0.1278
P3	4.1809 ± 0.0606
P4	4.0060 ± 0.0852

Table 4.2: Calibration factors of the internal magnetic probes.

Figure 4.18 shows the azimuthal magnetic field measured by the probe P1 at different distances from the rod. The magnetic field induced by the current source decays at a rate of $1/r$ as suggested by Equation 4.21. The measured field can be fitted by a reciprocal function A/r, where A is a constant. The curve fitting of the measured field is illustrated by the red curve in Figure 4.18.

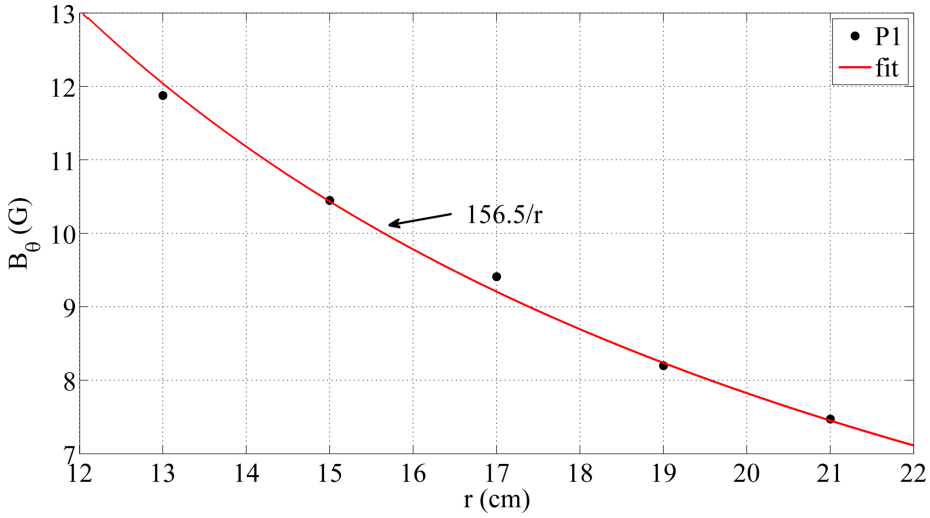

Figure 4.18: The azimuthal magnetic field measured by the first probe (P1) at different distances from the current source. The curve fitting is represented by the red curve.

Chapter 5

Experimental Results

5.1 Introduction

The resonant interaction between the RMP fields and the magnetic islands is studied in the STOR-M tokamak. The study is carried out numerically using a 2D, fixed boundary Grad-Shafranov solver code. The experimental RMP study is performed in STOR-M during low-q ohmic discharges with high MHD activities. The modification of toroidal flow velocity of impurity ions is also demonstrated by means of RMP fields. The effects of RMP on plasma edge parameters, namely the ion saturation current I_{si} and the floating potential V_f, are examined using the rake probe. Preliminary studies on RMP penetration and plasma response to the RMP field in STOR-M are conducted using the internal probe array.

5.2 MHD Measurements

5.2.1 RMP Simulation

The mechanism of resonant interaction between RMP and magnetic islands has been studied theoretically by several groups [180, 181]. Two analytical methods have been proposed to model the magnetic influence of RMP on MHD fluctuations. The first method is purely additive, meaning the RMP field is directly added to the perturbed magnetic field of the target island [182, 183]. This

method depends on the phase difference between the RMP field and the magnetic island. The method was revised later using the Hamiltonian formulation of magnetic field lines to describe the perturbative effect of RMP [184, 185]. The second method takes into the account the change in the plasma current, density and temperature profiles due to the application of RMP [186]. A numerical RMP simulation, adopted from the first method, is carried out in STOR-M. The simulation produces an equilibrium contour of poloidal flux surfaces, then adds magnetic perturbations on a selected resonant surface ($q = 2$ surface in this case). Afterwards, the simulation adds the perturbations of RMP to model the interaction between the RMP field and the magnetic island. It should be pointed out that the resonant interaction between magnetic islands and RMP can be treated as a two-fluid MHD problem [187]. The model described here uses a zeroth order approximation and does not take into consideration the attenuation of the RMP field due to the vacuum chamber or the plasma itself.

The numerical simulation is performed for three different scenarios of STOR-M equilibrium for actual STOR-M geometries ($a = 0.12$ m and $R = 0.46$ m), helical coil configurations and plasma parameters [188]. A 2D, fixed boundary Grad-Shafranov code, called the TOSCA code [189], is used to calculate the poloidal magnetic flux surfaces in equilibrium. The code also calculates the Shafranov shift as well as the profile of the safety factor q. A supplementary MATLAB code has been developed to impose magnetic perturbations on the $q = 2$ resonant surface, simulating an $m = 2$ magnetic island. The magnetic perturbations are approximated by [190]:

$$\psi_{mn} = \sum_{m,n} \alpha_{mn} \left[\frac{mq(1 + \cos(n\phi - m\theta))}{2|m - nq|} \right] \tag{5.1}$$

where m and n are the poloidal and toroidal mode numbers and α_{mn} is a numerical factor designated for the strength of the island perturbations for a particular mode. Since the above equation diverges when $m = nq$, the term $(m - nq)$ in the dominator must be excluded from the perturbation calculations at the resonant surface $q = m/n$. The perturbations are calculated for a (2, 1) island with $\alpha_{21} = 0.3\times\ 10^{-6}$, $0.25\times\ 10^{-6}$ and $0.2\ \times\ 10^{-6}$. It should be mentioned that other formulae

for poloidal flux perturbations have been proposed in other works which provide a better fit for the experimental observations [191]. The MATLAB code has also been used to model the RMP coils by four toroidal current conductors with a square cross-section of 25 mm^2. The coils located at poloidal angles 45° and 225° carry negative currents, while those located at 135° and 315° carry positive currents. The coils are placed at a distance 17 cm from the plasma center. Three cases are considered in this simulation, all with the same poloidal beta β_p (= 0.5) and B_ϕ (= 0.575 T), but different plasma currents I_p (20, 22.5 and 25 kA). The corresponding edge safety factors $q(a)$ for the three cases are 4.5, 4 and 3.6, respectively. The q-profile and the unnormalized radial profile of the magnetic perturbations $(\psi_{21})_r = mq/|m - nq|$ are shown in Figure 5.1 for the case with I_p = 22.5 kA.

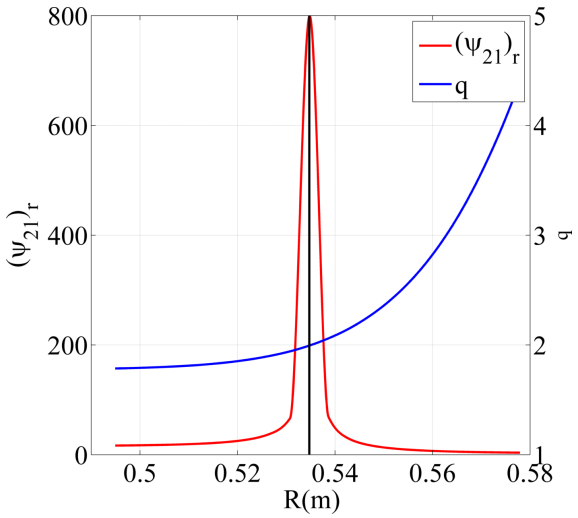

Figure 5.1: The radial profiles of the magnetic perturbations $(\psi_{21})_r$ and the q-profile for the intermediate case (I_p = 22.5 kA). The vertical line indicates the radial location of the resonant surface (2, 1).

The first case considered in the numerical simulation was a discharge with parameters of I_p = 20 kA, B_ϕ = 0.575 T, $q(a)$ = 4.5 and α_{21} = 0.3× 10^{-6}. A discharge with such parameters has been routinely established in STOR-M. Figure 5.2(a) shows the flux surfaces at equilibrium (no RMP applied) with an $m = 2$ magnetic island located at 3.2 cm from the plasma center. In Figure 5.2(b), the width of the $m = 2$ island does not change when the RMP current (I_{RMP}) increases from 0 to 1.2 kA (about 6% of I_p). The attenuation of RMP by the conducting plasma is not included

in this simulation and all other simulations to follow. A further increase in I_{RMP} to 2.4 kA and 3.6 kA (Figures 5.2(c) and (d), respectively) does not show any significant impact on the island width either. This qualitatively agrees with the results of RMP experiment conducted in the HT-6B tokamak (a small tokamak with a size similar to STOR-M) [25]. In that experiment, it was difficult to observe any effect from RMP on the $m = 2$ resonant surface when $q(a) > 4$. The simulation clearly indicates that the RMP coils are too far from the island and the current in the coils severely distorts the outer tokamak magnetic surface before it has any effect on the island itself.

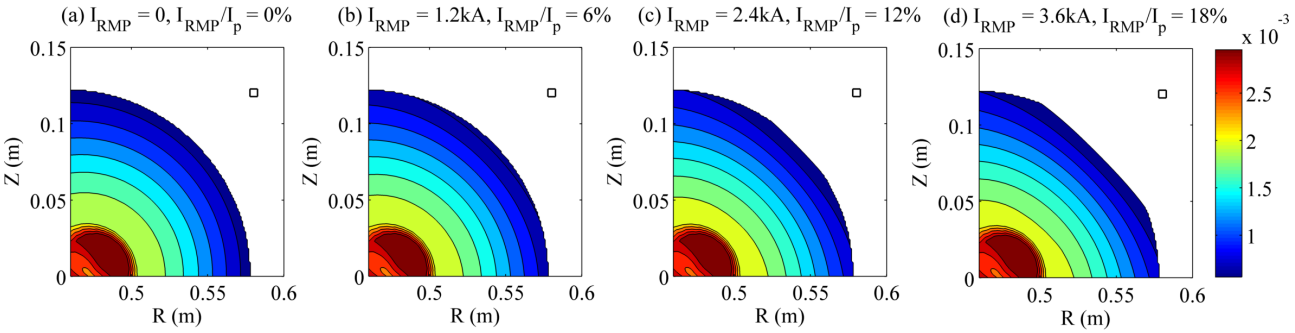

Figure 5.2: Effect of RMP current on an $m = 2$ magnetic island during a STOR-M discharge with $I_p = 20$ kA, $B_\phi = 0.575$ T, $q(a) = 4.5$ and $\alpha_{21} = 0.3\times\ 10^{-6}$.

The RMP experiment in HT-6B also demonstrated that RMP could effectively suppress the $m = 2$ fluctuations when $q(a)$ was near or lower than 4. In order to model those cases, a discharge with $I_p = 22.5$ kA, $B_\phi = 0.575$ T, $\alpha_{21} = 0.25\times\ 10^{-6}$ and low $q(a)$ (~ 4) is simulated to study the effect of RMP on $m = 2$ islands. At equilibrium, the $m = 2$ island, shown in Figure 5.3(a), has a width of approximately 0.28 cm and is located at a radius of 7.4 cm. The distance between the island and the RMP coil is approximately 9.6 cm. As shown in Figure 5.3(b), the island width is diminished to half its value (0.14 cm) when I_{RMP} increases from 0 to 1 kA. The island completely vanishes (Figure 5.3(c)) when I_{RMP} reaches a critical value of 2 kA, which corresponds to 8.8% of I_p. Exceeding the critical I_{RMP} triggers a disruptive $m = 2$ instability. This can be clearly seen in Figure 5.3(d) as I_{RMP} increases to 3 kA; a new $m = 2$ magnetic island is formed with a width of 0.28 cm at a radius of 6.9 cm. Increasing I_{RMP} even further aggravates the island which may eventually lead to a major disruption in the plasma discharge as observed previously in other tokamaks (e.g. the Tokoloshe tokamak) [192].

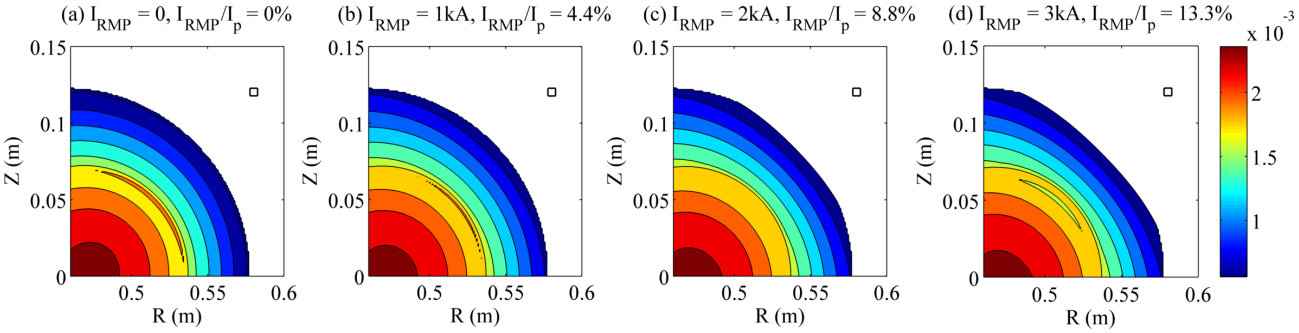

Figure 5.3: Effect of RMP current on an $m = 2$ magnetic island during a STOR-M discharge with $I_p = 22.5$ kA, $B_\phi = 0.575$ T, $q(a) = 4$ and $\alpha_{21} = 0.25\times\ 10^{-6}$.

Based on the simulation results for $q(a) = 4.5$ and 4 tokamak discharges, it is expected to reduce the critical value of I_{RMP} by decreasing the safety factor $q(a)$. However, q-value at the plasma edge should be kept above 3 to avoid deterioration in confinement time and large helical magnetic perturbations [193]. In another numerical simulation, the plasma current I_p is increased to 25 kA, corresponding to $q(a) = 3.6$ at $B_\phi = 0.575$ T. The α_{21} parameter is $0.2\times\ 10^{-6}$. The $m = 2$ island shown in Figure 5.4(a) is now located 8.5 cm from the plasma center. The width of the island is roughly 0.35 cm in the absence of I_{RMP}. Increasing I_{RMP} gradually from 0 to 800 A decreases the island width from 0.35 to 0.14 cm, as illustrated in Figure 5.4(b). It should be pointed out that in the previous case a higher I_{RMP} (about 1 kA) was required to reduce the $m = 2$ island width from 0.28 to 0.14 cm. Figure 5.4(c) shows a nearly complete suppression of the $m = 2$ island when the I_{RMP} magnitude reaches a critical value of 1.6 kA, which is about 6.4% of the total plasma current. Suppressing the $m = 2$ island with a lower I_{RMP} is an expected result as the distance between the $q = 2$ surface and the RMP coils (8.5 cm) is shorter compared with the previous case (9.6 cm). When I_{RMP} increases to a value of 2.4 kA, a new $m = 2$ island with a width of 0.14 cm is produced (shown in Figure 5.4(d)).

The simulation clearly illustrates that the width of the intrinsic $m = 2$ islands can be controlled by the RMP fields. If the controlled islands are made too wide, they interact with the limiter and induce disruptions. However, if the controlled islands are made smaller, they flatten the current profile at the $q = 2$ surface and reduce the shear on that surface. The shear reduction slows down the growth of tearing modes, thus improving the discharge and avoiding disruptions. Therefore,

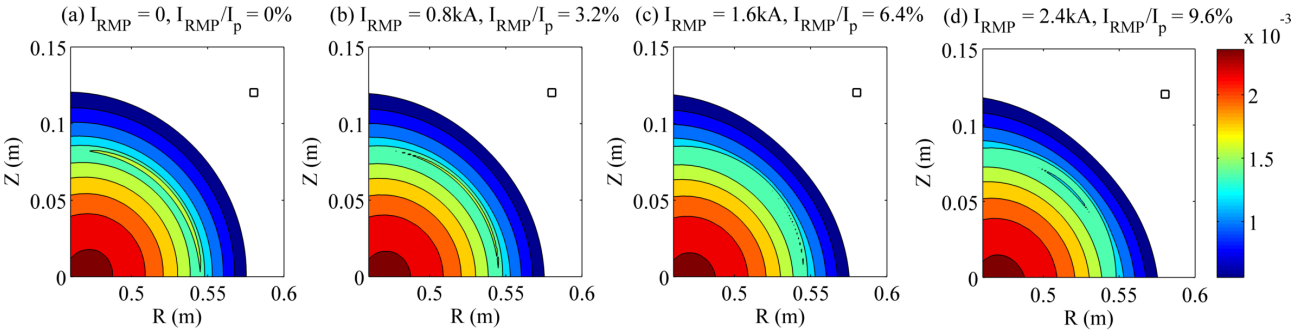

Figure 5.4: Effect of RMP current on an $m = 2$ magnetic island during a STOR-M discharge with $I_p = 25$ kA, $B_\phi = 0.575$ T, $q(a) = 3.6$ and $\alpha_{21} = 0.2\times\ 10^{-6}$.

natural disruptions occur in the plasma only when the discharge conditions allow the growth of very large islands [194].

5.2.2 RMP Experiment

The influence of RMP on plasma parameters was investigated experimentally in STOR-M [195]. During the discharge #225915, an RMP current pulse of about 2 ms was applied during an MHD active phase. The discharge parameters shown in Figure 5.5(a) are, from the top, plasma current I_p, loop voltage V_l, horizontal plasma position ΔH, H_α radiation, edge safety factor $q(a)$, SXR emission and Mirnov fluctuations. In this discharge ($I_p = 23.5$ kA, $V_l = 3.5$ V, $q(a) = 3.7$), the RMP pulse is applied at 20 ms during the plasma flat-top. The current in the RMP coils is about 600 A (2.5% of total plasma current). Flatness in the plasma current with a slight reduction in the loop voltage and clear suppression in the H_α emission level ($\sim 40\%$) are observed approximately 0.7 ms after applying RMP. The plasma column is shifted by 3 mm in the outward direction. The main effect of RMP on the discharge is the significant suppression in the MHD fluctuation signal and the increased SXR emission from the plasma core. Figure 5.5(b) shows the three expanded waveforms of I_{RMP}, central SXR and Mirnov fluctuation signals. The negative peak in I_{RMP} is an artefact due to the fast change in the current when the IGBT is switched off. This spike was later removed after adding the FRMP circuit with a diode connected across the RMP coil (see Figure 4.8). The amplitude of MHD oscillations is strongly attenuated between 20.7 and 22 ms. However,

the MHD activities start to grow even before the termination of RMP and resume the fluctuation level to the initial frequency and amplitude when I_{RMP} is turned off.

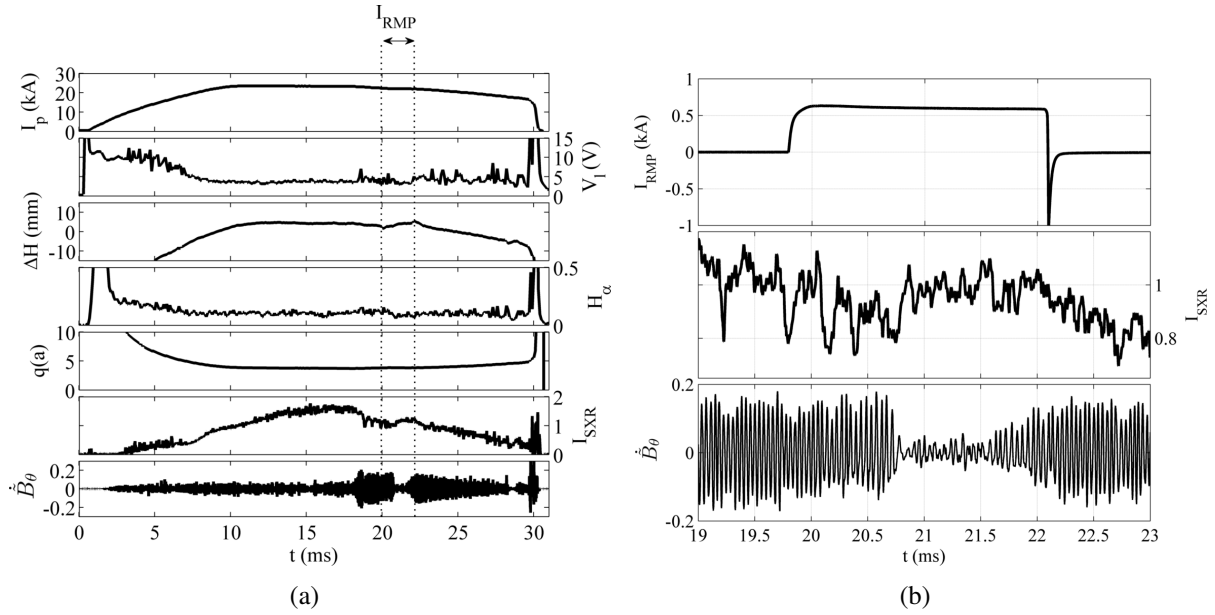

Figure 5.5: Effect of RMP on plasma parameters during STOR-M discharge #225915. The resonant field was applied at 20 ms for about 2 ms during the plasma current plateau.

The frequency characteristics of MHD and SXR signals are examined using wavelets. Mirnov signals before, during and after applying RMP are analyzed using SVD and the spatial Fourier series. Contour plots of Mirnov and SXR raw signals during the RMP pulse are shown in Figure 5.6(a). The suppression of Mirnov oscillations does not occur immediately when the RMP pulse is applied, possibly to due the time needed for the RMP field to penetrate the plasma. The emission level of SXR increases around the time when Mirnov oscillations are suppressed. Figure 5.6(b) shows wavelet spectra of Mirnov and SXR signals. Both signals are clearly coherent at a frequency of 25 kHz before and after applying RMP. However, during the RMP pulse, a gradual reduction in MHD amplitude and frequency can be seen on the Mirnov spectrum between 20 and 20.7 ms. The MHD frequency is reduced from 25 to 20 kHz. This gradual reduction in amplitude and frequency is missing on the SXR spectrum since the $m = 2$ oscillations on the SXR signal reduced to an undetectable level immediately following application of RMP. The difference in the response time of SXR and Mirnov signals to RMP seems to suggest that the plasma temperature peaks before the

magnetic structure of island vanishes. This phenomenon demonstrates that the response time for temperature/density in the plasma is different from that for the current and magnetic field. Another plausible explanation is the nonlinear response of the SXR detector to the emission intensity.

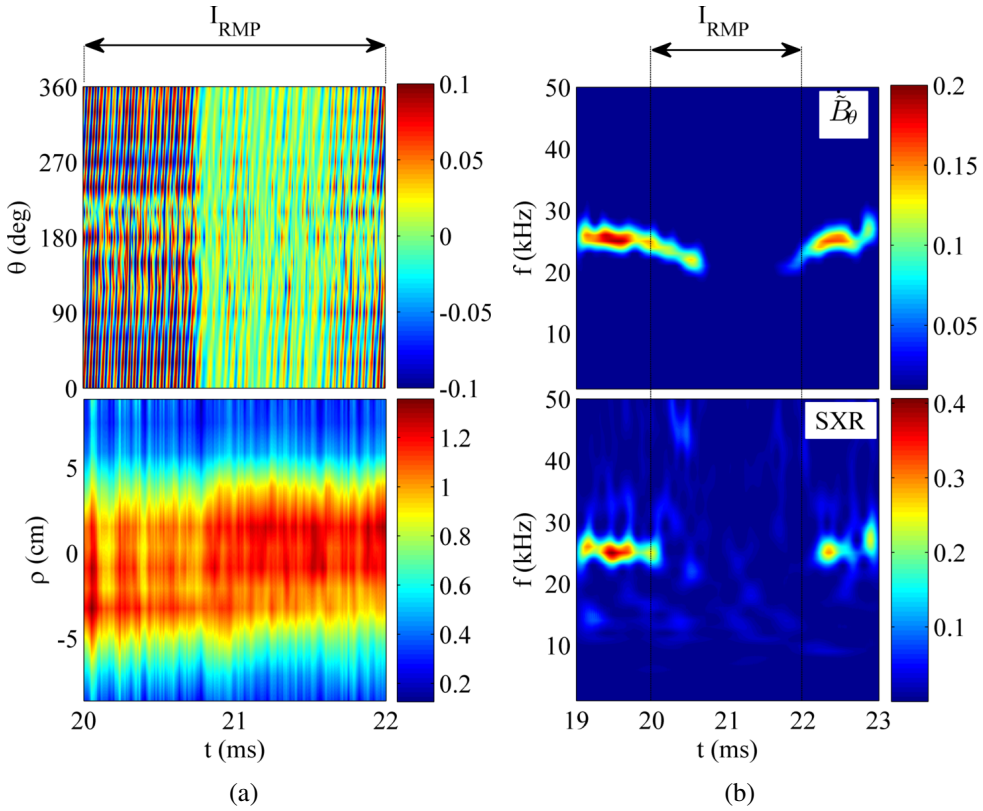

Figure 5.6: Comparison between the effect of the RMP field on Mirnov and SXR signals using (a) contour plots and (b) wavelet power spectra. Mirnov and SXR signals are highly coherent at 25 kHz before and after the RMP pulse.

Figure 5.7 shows the expanded traces of Mirnov and SXR signals around the time of the RMP pulse. The traces shown in this figure are signals from two central SXR chords V7 and V8 (see Figure 4.2) and from an inboard magnetic probe. Clear sawtooth and inverted sawtooth oscillations can be seen in V7 and V8 signals, respectively, indicating that the $q = 1$ surface is located between 0.9 cm and 2.1 cm at that time. Sawtooth oscillations are active when the relative amplitude of Mirnov signals is low during the period from 15 to 18 ms. However, the sawtooth oscillations vanish when Mirnov oscillations start growing at 18 ms. During the high Mirnov amplitude phase, the oscillations imposed on SXR signals are found to be well correlated with Mirnov oscillations

(refer to Figure 5.6(b)). The helical current applied at 20 ms causes a strong decay in the Mirnov amplitude and an increase in the averaged SXR level in the V7 channel.

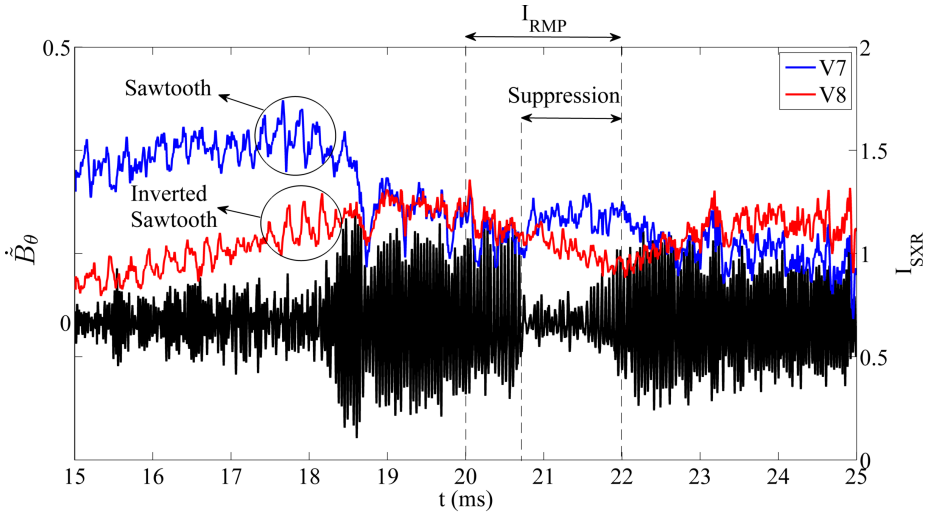

Figure 5.7: Expanded traces of Mirnov and SXR signals during shot#225915.

The spatial structure and the temporal evolution of MHD modes before applying RMP, during the MHD suppression and after turning off RMP are extracted using the SVD analysis. Three time windows, each 0.5 ms long, are chosen for the SVD analysis. The time windows are located before (19.5-20 ms), during (21-21.5 ms) and after (22.25-22.75 ms) applying RMP. As mentioned in Subsection 3.8.2, SVD extracts the spatial and temporal features of MHD modes in a form of eigenvectors called PAs and PCs. PAs and PCs of the dominant poloidal MHD modes before, during and after the RMP pulse are, respectively, shown in Figures 5.8(a), (b) and (c). The middle polar plot corresponds to the dominant mode during the MHD suppression. The spatial structure can be clearly identified as an $m = 3$ mode. The first and last modes are spatially distorted, although they have a similar structure. The distortion in PA indicates that two or more modes oscillate at the same frequency (i.e. mode coupling). The coupled MHD harmonics can be identified by performing a spatial Fourier analysis on the distorted PA. The toroidal mode number corresponds to $n = 1$ in this discharge, which is the typical case for most of the STOR-M discharges.

Figure 5.9 shows the relative mode spectra of PAs as extracted by the Fourier analysis. The spectrum of the first PA (before firing RMP) shows that the coupled mode consists mainly of $m = 2$

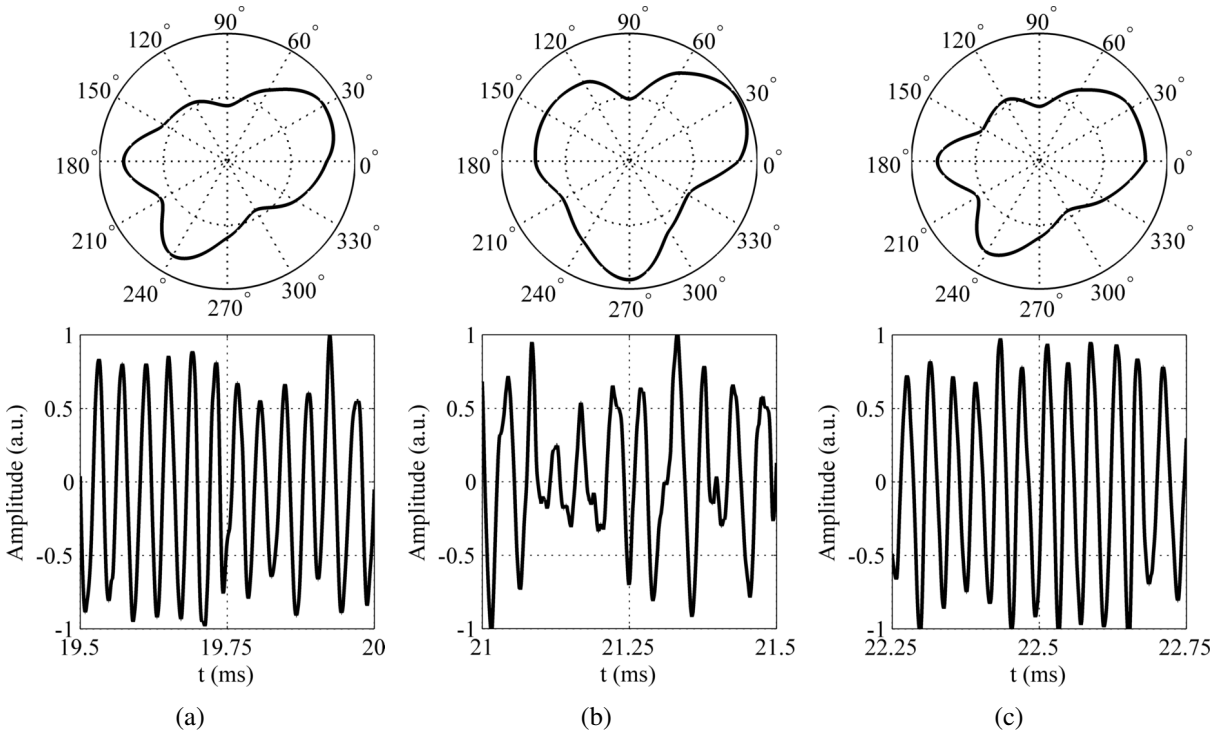

Figure 5.8: Spatial structure and temporal evolution of dominant poloidal MHD modes (a) before (b) during and (c) after applying RMP as extracted by SVD.

mode ($\sim 52\%$) and $m = 3$ mode ($\sim 26\%$). Other modes (i.e. $m = 1$ and $m = 4$ modes) also appear in the spectrum with no significant contribution to the global mode amplitude. During the MHD suppression phase (21-21.5 ms), the mode spectrum indicates that the dominant poloidal number is $m = 3$ with energy content up to 54%. Although $m = 2$ also contributes to the spectrum by 23%, it does not distort the spatial structure of the dominant $m = 3$ mode, as shown in Figure 5.8(b). After turning off RMP, the $m = 2$ mode grows again causing a spatial distortion to the dominant mode, similar to the case before applying RMP. The $m = 2$ mode oscillates with a relative amplitude of 48%, while the $m = 3$ mode oscillates with an amplitude of 28%. Apparently RMP does not have a strong effect on $m = 1$ and $m = 4$ modes since they maintain the same relative amplitude in the three cases. Note that the plots are percentage amplitudes normalized for signals within each time window. The absolute amplitudes of any particular mode for the three time windows cannot be extracted from Figure 5.9.

The magnitudes of harmonics from $m = 1$ to $m = 4$ modes can be obtained using the spatial

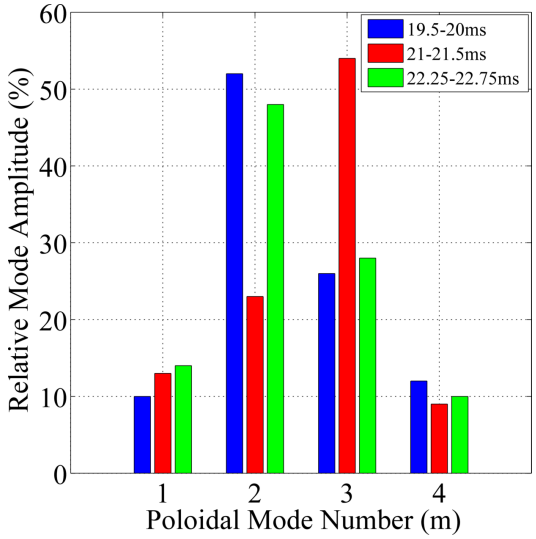

Figure 5.9: Spatial Fourier analysis of PAs before, during, and after applying RMP.

Fourier series. The spatial Fourier series decomposes the sine and cosine components of each mode from raw Mirnov signals. The analysis was performed on the time segment 19-23 ms (1 ms before and after applying RMP). The mode magnitudes are plotted in Figure 5.10. The $m = 2$ mode has the highest magnitude among the other modes before firing the RMP pulse. There is no visible change in mode magnitudes for about 0.7 ms after applying the helical current. However, the $m = 2$ magnitude drops suddenly by 90% at 20.7 ms, while the other modes are suppressed by approximately 65-75%. The $m = 3$ fluctuation amplitude dominates over the other modes during the suppression phase. The suppression lasts for about 1.5 ms until $t = 22$ ms when the modes start oscillating at their original amplitudes prior to applying RMP, with $m = 2$ being the dominant mode again. The spike on the figure at 22 ms is caused by a noise spike in RMP when the current is suddenly turned off by the IGBT switch, as shown in Figure 5.5(b). The spike appears on some Mirnov signals when the coil is close to RMP windings, but it does not appear on other diagnostic signals (see Figure 5.5(a)). As mentioned earlier, this spike was eliminated in the later RMP experiments by adding a diode that blocks any return currents in the RMP circuit.

Figures 5.5, 5.6 and 5.10 show that the amplitude of $\dot{B}_\theta$ fluctuation signal remains intact during the initial 0.7 ms after applying the RMP pulse even though the frequency reduces from 25 to 20 kHz. This behaviour seems to be different from that associated with the locked mode described

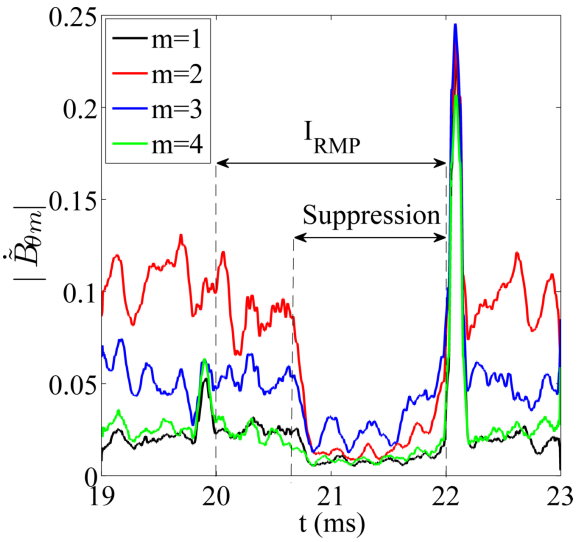

Figure 5.10: Mode magnitudes for MHD modes up to $m = 4$ around the time of firing RMP.

in other devices [196]. After 0.7 ms, the $m = 2$ mode and other harmonics suddenly decrease significantly (up to 90% for $m = 2$ mode, see Figure 5.10). After the suppression phase, the fluctuation level gradually increases even before the RMP pulse is turned off, indicating a transient feature of MHD suppression by RMP. After RMP is switched off, the MHD fluctuation level returns to the level before application of RMP.

Figure 5.11(a) shows the radial distribution of SXR intensity for the time period 15-25 ms. The intensity profile is constructed along the impact parameter of vertical SXR chords ρ (in cm), where $\rho = 0$ corresponds to the tokamak center. The SXR profile peaks during the sawtooth activities from 15 to 18 ms. The profile flattens afterwards as the Mirnov oscillations grow in amplitude. When RMP is applied at 20 ms, a slight increase and displacement in SXR radial profile occur, associated with the MHD suppression and the low H_α emission level. Figure 5.11(b) shows three radial profiles of SXR emissivity constructed at 19.84, 21.96 and 22.74 ms. The profiles at 19.84 and 22.74 ms, corresponding to the phase before and after applying RMP, have a similar radial distribution centered around channel V8. However, during the RMP pulse (21.96 ms), a high SXR emission level is observed in channel V5. In addition, the radial SXR brightness profile shifts outwards along with the plasma displacement ΔH.

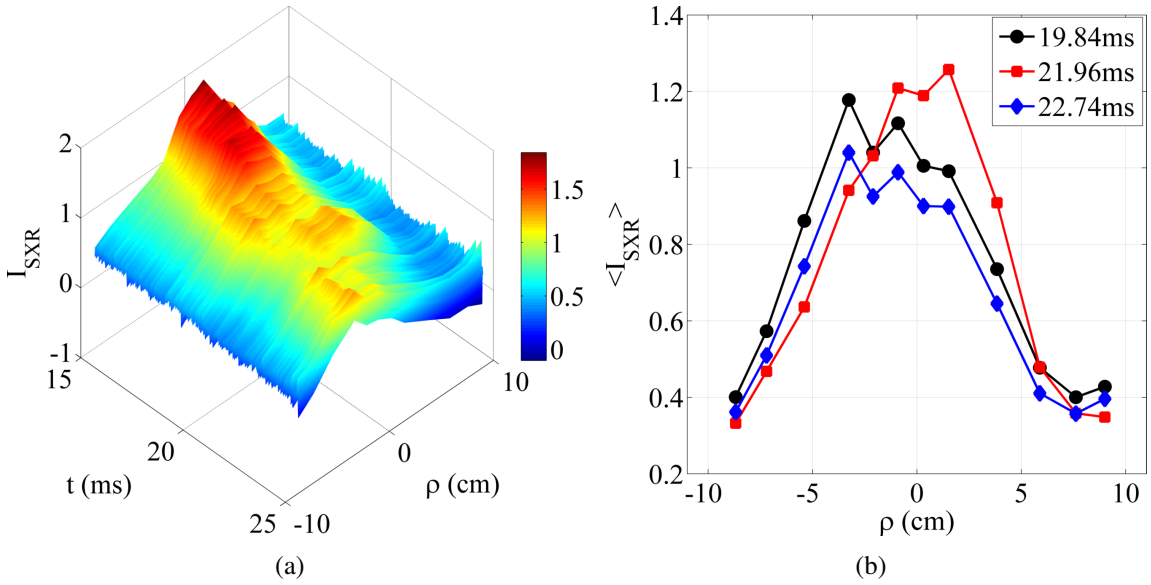

Figure 5.11: (a) 3D radial distribution of SXR emissions and (b) radial profiles of SXR intensity for instants before, during and after applying the RMP pulse.

5.3 Plasma Flow Measurements

5.3.1 MHD Frequency Simulation

It is commonly recognized in the ideal MHD theory that the magnetic perturbations created by magnetic islands are frozen within the plasma, forcing the islands to move at the same macroscopic velocity of the plasma [197]. However, the two-fluid theory suggests the inclusion of the electron diamagnetic frequency in the island rotation velocity. The magnetic islands observed in tokamaks rotate in the direction of the electron diamagnetic drift, which is the characteristic of resistive MHD modes. The extended theory of tearing modes, which takes into account the effects of the finite Larmor radius, predicts that the MHD rotation frequency is in the order of the electron drift frequency. The experimental observations, however, have shown a rough agreement between the MHD frequency and the electron diamagnetic frequency. It has been observed experimentally that the MHD frequency is often associated with the toroidal plasma rotation at the rational q surfaces. The recent observations in the MAST tokamak suggested that the poloidal plasma rotation may also contribute to the MHD frequency [198]. However, previous experiments conducted in

ASDEX-U [199] and TEXTOR [200] tokamaks have shown that the poloidal plasma rotation can be neglected due to the poloidal flow damping. Furthermore, it has been observed in the TEXT tokamak that the toroidal plasma rotation is damped by the momentum loss due to the ion-neutral charge exchange [201]. The sheared radial electric field can also play an important role in the MHD frequency as some ideal and resistive modes rotate with the $\mathbf{E} \times \mathbf{B}$ drift velocity.

A model is adopted for STOR-M to understand the main mechanisms that determine the rotation frequency of islands. Various assumptions for the MHD frequency have been considered in previous theoretical works to link the observed MHD frequency with the plasma flow velocities. One of the common approaches to study the rotation of magnetic islands in tokamaks is to assume rigid body rotation of the plasma column and to measure the MHD frequency associated with the fluctuations in the electron cyclotron emission (ECE), reflectometry, or magnetic probe signals.

A magnetic island rotating in the toroidal/poloidal direction causes fluctuations in the signal detected by a magnetic probe at a fixed location. The magnetic signals collected by the Mirnov probes can be used to identify the direction of the island rotation. The coordinate system is chosen so that the positive ϕ direction is along the toroidal magnetic field and the positive θ direction is along the electron diamagnetic drift velocity (v_e^*). Therefore, if the direction of the plasma current and the toroidal field is the same, then B_θ is positive. Otherwise, B_θ is negative. In STOR-M, the direction of I_p is typically counter-clockwise and B_ϕ is clockwise (viewed from the top), unless stated otherwise. Figure 5.12 shows poloidal and toroidal contour plots obtained by the poloidal and toroidal Mirnov arrays. The colored stripes on the contour plots point to the direction of the island propagation. The plots suggest that the island rotates poloidally in the direction of electron diamagnetic drift and toroidally in the direction opposite to the plasma current direction (counter-current). There are two peaks on the poloidal contour plot when θ changes from 0 to 2π at a fixed time, indicating an $m = 2$ mode. Similarly, the toroidal $n = 1$ mode can be identified from the toroidal contour plot. Experiments on STOR-M have shown that reversing I_p does not change the direction of the island rotation because the electron diamagnetic drift is only determined by the directions of B_ϕ and the electron pressure gradient ∇p_e.

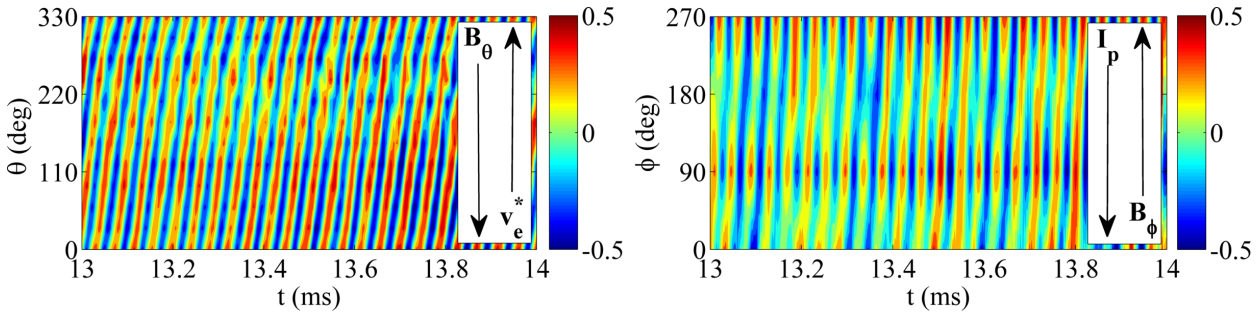

Figure 5.12: Poloidal and toroidal contour plots of Mirnov oscillations. The magnetic island rotates poloidally in the direction of v_e^* and toroidally in the counter-current direction.

The model requires extracting the poloidal and toroidal MHD mode numbers from the fluctuation signals. In addition, poloidal drifts of charged electrons and ions play important roles in determining MHD fluctuation frequencies. Two well-known cross-field drifts are the diamagnetic and the $\mathbf{E} \times \mathbf{B}$ drifts determined by the local radial profiles of pressure, temperature, density, and electric field. Since the local measurements of plasma equilibrium profiles are rather complicated, the so-called Kadomtsev-Tayler (K-T) model can be used to produce these profiles [202]. The natural density, temperature and pressure profiles are respectively expressed by:

$$n_e(r) = n_i(r) = n(0) \cdot f(r) \tag{5.2}$$

$$T_e(r) = T_i(r) = T(0) \cdot f^2(r) \tag{5.3}$$

$$p_e(r) = p_i(r) = p(0) \cdot f^3(r) \tag{5.4}$$

where $n(0)$, $T(0)$ and $p(0)$ are the density, the temperature and the pressure at the plasma center ($r = 0$). The axially symmetric distribution function $f(r)$ is given by:

$$f(r) = \left(1 + \left(\frac{q(a)}{q(0)} - 1\right)\frac{r^2}{a^2}\right)^{-2/3} \tag{5.5}$$

where $q(a)$ is the safety factor at the plasma edge. The safety factor at the magnetic axis $q(0)$ can

be approximated for a sawtoothing plasma by:

$$q(0) = \frac{q(a)}{q(a)+1} \tag{5.6}$$

The distribution function $f(r)$ can be simplified by:

$$f(r) = \left(1 + q(a)\frac{r^2}{a^2}\right)^{-2/3} \tag{5.7}$$

Figure 5.13 shows the radial profiles of plasma parameters in STOR-M which are calculated using the following experimental values: $I_p = 20$ kA, $B_\phi = 0.575$ T, $a = 0.12$ m, $R = 0.46$ m, $\langle n_e \rangle = 1 \times 10^{19}$ m^{-3}, and $T_e(0) = 200$ eV.

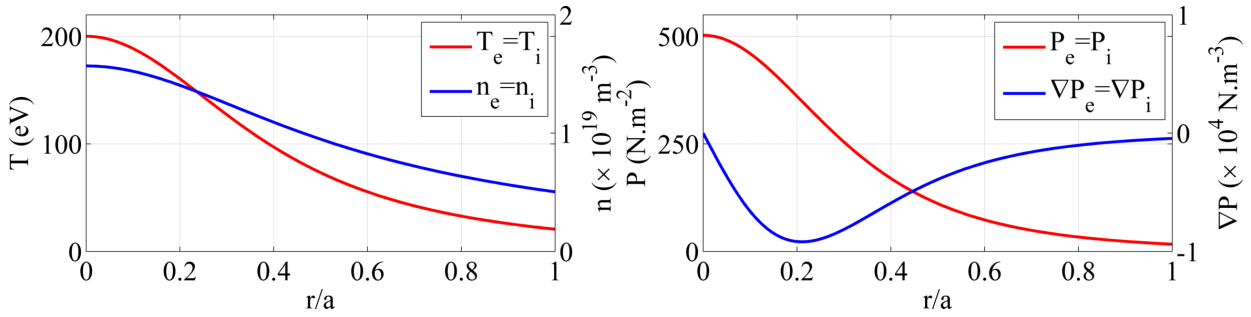

Figure 5.13: Radial profiles of temperature, density, pressure and pressure gradient assumed for the STOR-M tokamak.

The diamagnetic drift in tokamaks is mainly in the poloidal direction due to the large toroidal magnetic field compared with the poloidal field. The diamagnetic drift of a selected MHD mode is often expressed in terms of frequency rather in velocity. In order to calculate the electron diamagnetic frequency, the pressure gradient and local density profiles are needed. The electron diamagnetic frequency at any given minor radius r is expressed by:

$$f_e^* = \frac{1}{2\pi r}\frac{1}{en_eB_\phi}\frac{dp_e}{dr} \tag{5.8}$$

The poloidal and toroidal components of ion velocity in tokamaks can be calculated from the neoclassical theory of plasma rotation [203]. The neoclassical expressions for the poloidal velocity

and the derivative of toroidal velocity are given by [204]:

$$v_{\theta}^{\text{neo}} = \frac{\kappa}{eB_{\phi}} \frac{dT_i}{dr} \tag{5.9}$$

$$\frac{dv_{\phi}^{\text{neo}}}{dr} = 0.107 \frac{\kappa T_i q^2}{eB_{\theta}} \left(\frac{d \ln T_i}{dr} \right)^2 \tag{5.10}$$

where the collisionality coefficient κ depends on the collisionality regime: $\kappa = 1.17$ in the banana regime, $\kappa = -0.5$ in the plateau regime, and $\kappa = -1.83$ in the Pfirsch-Schlüter regime. The radial profile of q is assumed to be quadratic, so that:

$$q(r) = q(0) \left(1 + q(a) \frac{r^2}{a^2} \right) \tag{5.11}$$

The radial profile of B_{ϕ} in Equation 5.9 can be obtained from the following expression:

$$B_{\phi}(r) = \frac{\mu_0}{2\pi} \frac{NI}{r + R} \tag{5.12}$$

where N is the total number of turns in the toroidal windings and I is the current passing through the windings. In STOR-M, N is 144 turns and I is about 9 kA to generate a 0.575 T toroidal field. The local poloidal magnetic field in Equation 5.10 can be derived from the plasma current profile:

$$B_{\theta}(r) = \frac{\mu_0}{2\pi} \frac{I_p(r)}{r} \tag{5.13}$$

The current profile can be estimated from the radial profile of the plasma current density J_p which is defined by:

$$J_p(r) = J_p(0) \cdot f^3(r) = J_p(0) \left(1 + q(a) \frac{r^2}{a^2} \right)^{-2} \tag{5.14}$$

where $J_p(0)$ is the current density in the plasma center which is given by:

$$J_p(0) = \frac{1 + q(a)}{\pi a^2} I_p(a) \tag{5.15}$$

Integrating Equation 5.14 from 0 to r and over the plasma cross-section yields:

$$I_p(r) = \int_0^{2\pi} \int_0^r J_p(r')r'dr'd\theta = I_p(a)\left(\frac{r^2}{a^2}\frac{1+q(a)}{1+q(a)r^2/a^2}\right) \tag{5.16}$$

Substituting Equation 5.16 into Equation 5.13 leads to:

$$B_\theta(r) = \frac{\mu_0}{2\pi}\frac{I_p(a)}{r}\left(\frac{r^2}{a^2}\frac{1+q(a)}{1+q(a)r^2/a^2}\right) \tag{5.17}$$

Figure 5.14 shows the radial profiles of I_p, J_p, B_ϕ and B_θ used in the model.

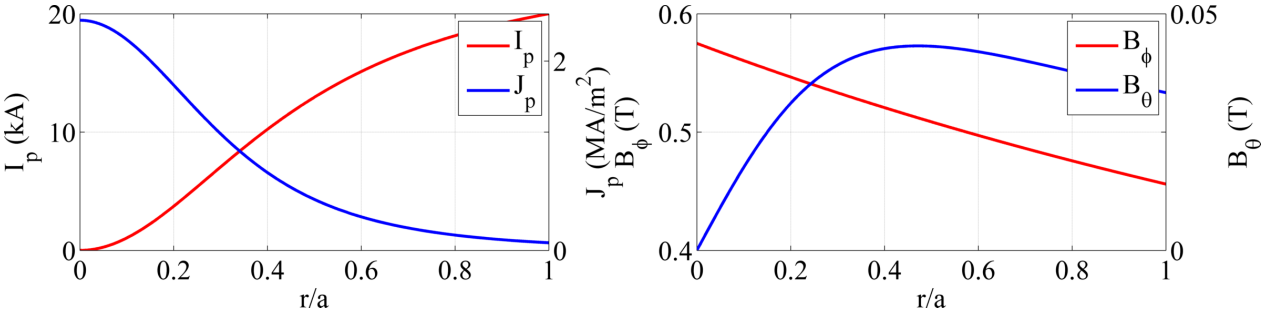

Figure 5.14: Radial profiles of plasma current, toroidal and poloidal magnetic fields in STOR-M.

The related analyses and calculations of the electron diamagnetic frequency and the neoclassical plasma velocities are shown in Figure 5.15. The κ parameter is chosen to be -1.83 for STOR-M discharge conditions. Note that the κ coefficient determines the direction of poloidal rotation. In the banana regime, the poloidal plasma flow rotates in the direction of the ion diamagnetic drift direction, whereas, in the collisional (Pfirsch-Schlüter) regime, the poloidal rotation is in the direction of the electron diamagnetic drift.

The toroidal rotation calculated from the neoclassical theory seems higher than the toroidal flow measurements conducted recently in STOR-M. One reason is that the neoclassical toroidal rotation is assumed only for primary ions in plasma without taking into the account the impurity flow velocity. As mentioned in Section 4.4, the experimental flow measurements in STOR-M are only carried out for some impurity species at selected radial locations. Moreover, the neoclassical poloidal rotation seems significant in STOR-M, although a comparison with experimental data is

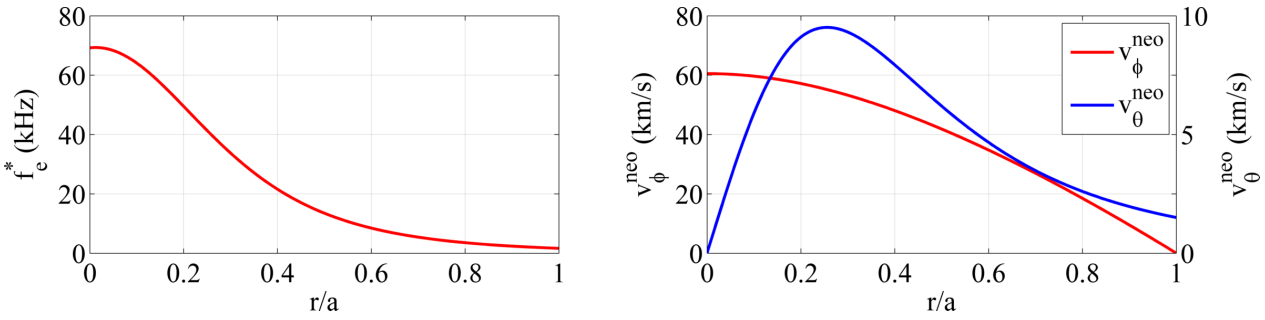

Figure 5.15: (Left) Radial profile of calculated electron diamagnetic drift frequency. (Right) Theoretical (neoclassical) calculations of poloidal and toroidal rotation velocities in STOR-M with $\kappa = -1.83$.

not possible since the poloidal flow measurements are not available in STOR-M. In small tokamaks such as CT-6B [205] and TCABR [206] tokamaks, the poloidal rotation was reported to be significant and unaffected by the poloidal flow damping, indicating that the poloidal rotation in STOR-M might behave similarly to the poloidal rotation in those tokamaks.

Many plasma rotation theories either assume that the impurity rotation is in the same order of the primary ions rotation or completely omit the impurities contribution. However, there is a fundamental discrepancy between the experimental observations and the theoretical predictions of plasma rotation, at least in the collisional regime. In the collisional plasma, the toroidal flows of primary ions and impurities are strongly coupled through the parallel friction, while the poloidal flows are weakly coupled due to the poloidal flow damping. It has been found that the difference in the poloidal rotation depends mainly on the pressure gradients of impurities and primary ions, whereas the toroidal rotation depends only on the gradients of ion density and temperature. Furthermore, the toroidal flow in pure ohmic plasmas rotates at different values and directions, depending on the local discharge conditions of a tokamak. It has been observed that the ion flow rotates in the counter-current direction in some machines, and in the co-current direction in others. The toroidal flow can change directions in the same discharge, or even rotates in one direction in the plasma core and in the opposite direction at the plasma edge.

The magnetic fluctuations observed in the STOR-M tokamak usually oscillate in the frequency range of 20-40 kHz. The dominant MHD mode numbers associated with such oscillations are

typically between $m = 2$ and $m = 4$ with low toroidal mode number ($n = 1$). In this model, various assumptions are considered for the MHD frequency observed in STOR-M. The different assumptions are described by the following equations:

$$f_{\text{MHD}} = m f_e^* \tag{5.18}$$

$$f_{\text{MHD}} = n f_\phi + m f_e^* \tag{5.19}$$

$$f_{\text{MHD}} = n f_\phi + n f_\theta \tag{5.20}$$

$$f_{\text{MHD}} = n f_\phi + n f_\theta + m f_e^* \tag{5.21}$$

where m and n are the poloidal and toroidal mode numbers. f_ϕ and f_θ are the toroidal and poloidal rotation frequencies associated with the toroidal and poloidal flow velocities v_ϕ and v_θ. The toroidal and poloidal rotation frequencies are evaluated respectively by:

$$f_\phi = \frac{v_\phi}{2\pi R} \tag{5.22}$$

$$f_\theta = \frac{v_\theta}{2\pi r} \tag{5.23}$$

The radial profiles of frequency assumptions are plotted in Figure 5.16 against a quadratic q-profile. The vertical lines in the figure indicate the radial location of resonant surfaces. It seems Equation 5.18 represents the lowest boundary estimation of MHD frequency as the case in many MHD theories. The MHD frequency peaks in the plasma core and decreases towards the plasma edge. At the plasma center it appears that Equation 5.21 yields the highest MHD frequency ($\sim$ 150 kHz) among other assumptions. The frequency of all assumptions becomes comparable at the plasma edge region.

Figure 5.17 shows a comparison between theoretical MHD frequencies at different rational surfaces and an experimental MHD frequency. The experimental MHD frequency is an averaged value of MHD frequencies of a series of STOR-M discharges with similar conditions. The dominant MHD mode and frequency of each discharge were extracted by the spatial Fourier series. The

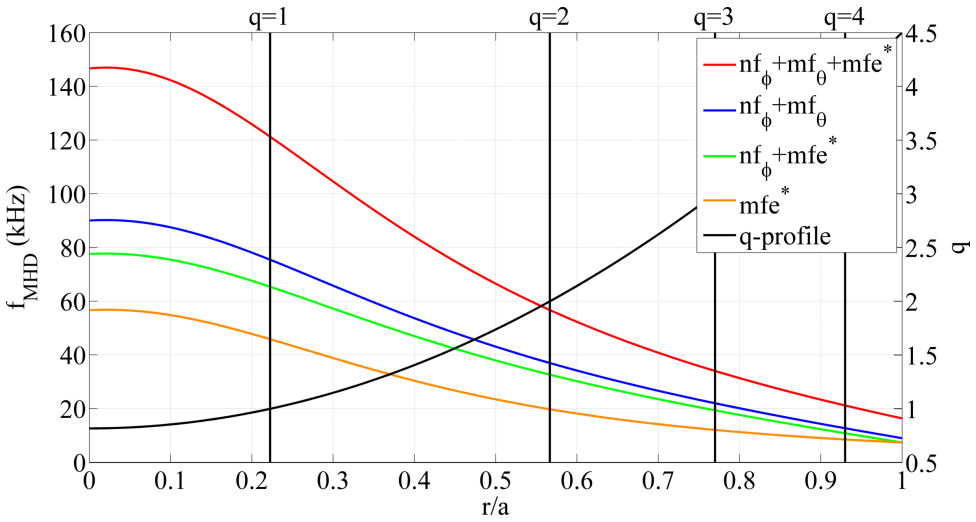

Figure 5.16: Radial profiles of different assumptions for the MHD frequency. The vertical lines indicate the radial location of the rational q surfaces.

dominant MHD mode was found to be (3, 1) oscillating at an average frequency of 38.6±3.1 kHz. There is a rough agreement between the theoretical and experimental MHD frequencies near the $q = 3$ surface. However, Equation 5.21 seems to provide the best fit for the observed MHD frequency in STOR-M. The theoretical MHD frequency calculated by Equation 5.21 and the experimental frequency of (3, 1) island differ only by 4.6 kHz. The frequency of electron diamagnetic term (mf_e^*) is around 12 kHz, which corresponds to 35.4% of the total frequency of (3, 1) island. The toroidal flow frequency (nf_ϕ) is about 7.3 kHz, comprising only 21.5% of the MHD frequency. The rotation frequency of poloidal flow ($mf_\theta = 14.7$ kHz) contributes by 43.1% to the MHD frequency at the $q = 3$ surface.

5.3.2 Toroidal Flow Measurements

The influence of RMP on magnetic fluctuations was examined during the discharge #247587. The RMP pulse was applied at 20 ms during the plasma flat-top for a duration of 8 ms. The current in the RMP coils is about 1.1 kA. The top panel in Figure 5.18(a) shows the waveforms of I_{RMP} and magnetic fluctuations. The spatial harmonic analyses revealed that the magnetic fluctuations are associated with a dominant (3, 1) magnetic island. It has been shown previously in Subsection 5.2.2 that the RMP field suppresses not only the (2, 1) islands, but also interacts with other islands,

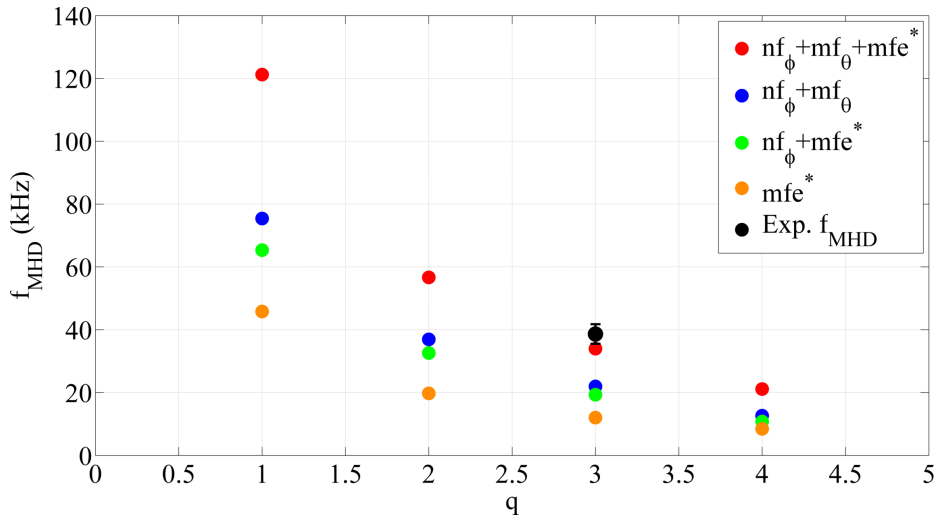

Figure 5.17: Comparison between theoretical MHD frequencies and experimental MHD frequency of (3, 1) island.

such as (3, 1) and (4, 1) islands, via the sideband islands. The corresponding wavelet spectrum of a magnetic fluctuation signal during the RMP pulse is shown in the middle panel. Clear reduction in (3, 1) amplitude and frequency can be seen on the wavelet spectrum. The frequency and amplitude of MHD oscillations seem to respond differently to RMP as the mode frequency drops immediately, while the suppression of mode amplitude occurs 0.5 ms after applying the RMP pulse. The MHD frequency drops from 40 kHz to about the half ($\sim$ 20 kHz). The amplitude of Mirnov oscillations also drops by $\sim$ 50% during the RMP pulse, suggesting that the reduction in Mirnov signal is mainly due to the reduction in frequency. The amplitude and frequency of (3, 1) fluctuations return to the normal levels prior to applying RMP. The last panel in Figure 5.18(a) shows the fluctuation frequency and amplitude (RMS value) of the dominant (3, 1) magnetic island during application of the RMP field. The frequency and amplitude of magnetic island are substantially reduced during the RMP pulse. The island frequency is reduced from 40 kHz to roughly 20 kHz. This braking phenomenon illustrates the effect of the electromagnetic (EM) torque induced by the RMP field on the magnetic island.

The toroidal EM torque exerted by RMP on magnetic islands is similar to the EM torque generated by error fields during the mode locking. The resonant flux surfaces can be treated as a thin conducing layer. When the RMP field penetrates the resonant surface, helical eddy currents are

generated on that surface in response to the radial component of RMP field. The RMP field interacts with a fraction of the eddy currents to produce an EM torque. The EM torque is sensitive to the phase difference between the RMP field and the eddy currents. If the phase shift between RMP and the eddy currents is denoted by φ, then the EM torque is proportional to $\sin\varphi$. The EM torque is maximum when the phase shift is $\frac{\pi}{2}$ and minimum when the phase shift is zero. The phase shift has a strong dependence on the rotation frequency at the resonant surface [207].

The toroidal flow velocities of C_{III}, O_V and C_{VI} impurity lines were measured by the IDS system in the presence of the RMP field. The C_{III} emission line is located near $r = 7$ cm and O_V line is at $r = 3$ cm, while the C_{VI} line peaks at $r = 0$. It should be mentioned that the radial profile of C_{III} line peaks near the $q = 2$ resonant surface (~ 7 cm) as shown in Subsection 5.3.1 and suggested by other calculations of safety factor profile in STOR-M. When the $q = 2$ surface is located at $r = 7$ cm, a 1 kA RMP current generates a 30 G radial magnetic field at that radial location, which is about 0.5% of the total toroidal field. Figure 5.18(b) shows the change of the impurity velocities during a 600 A RMP pulse applied between 12 and 17 ms. In the figure, the positive velocity indicates a rotation in the counter-current direction (clockwise), and the negative sign indicates a rotation in the co-current direction (counter-clockwise). Before turning on RMP the C_{III} impurities rotate in the co-current direction, while O_V and C_{VI} impurities rotate in the counter-current direction. When the RMP pulse is fired at 12 ms, the flow velocity of C_{III} increases in the co-current direction. The RMP field, however, slows down the toroidal velocities of O_V and C_{VI} impurities and even reverses their direction to the co-current direction.

The relationship between the change of toroidal flow velocity of impurities in the core region ($q < 2$) and the magnitude of RMP current is investigated. As mentioned before, the O_V and C_{VI} impurities are respectively located at $r = 3$ cm and 0 cm. Figure 5.19 shows the flow velocity of O_V and C_{VI} impurities for the cases with zero RMP current and with three other I_{RMP} values. Without I_{RMP} (black curves), the direction of toroidal flow is in the counter-current direction (positive). Once the current of the RMP pulse, applied between 20 and 28 ms, exceeds a threshold, the magnitude of toroidal flow velocity of O_V and C_{VI} impurities is reduced and the change is more significant

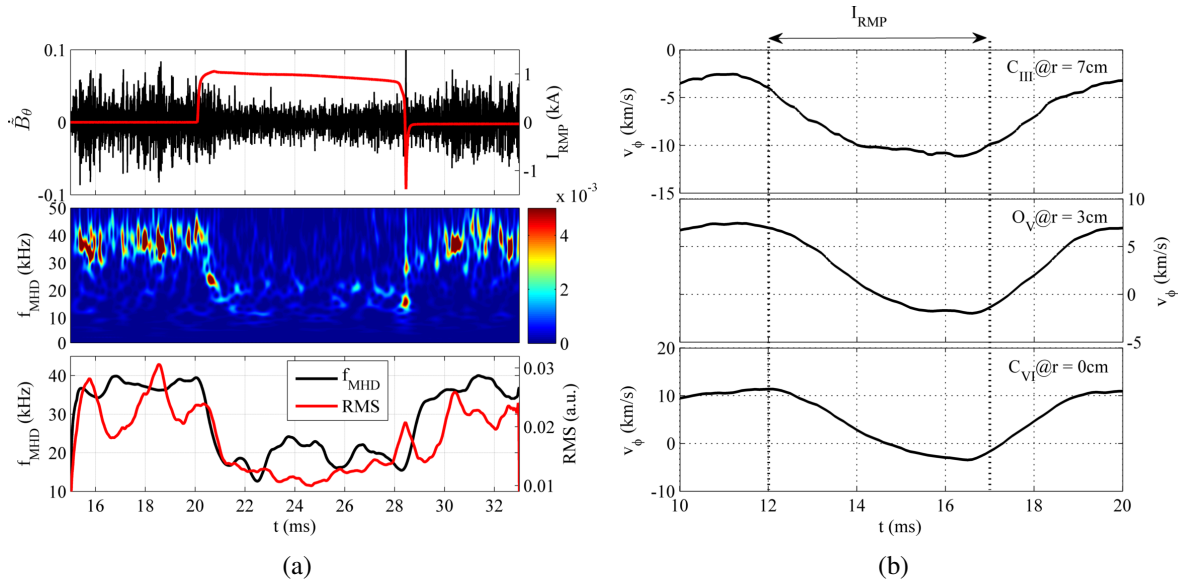

Figure 5.18: (a) Suppression and braking of magnetic islands by a single RMP pulse during shot#247587. The RMP current is about 1.1 kA and applied between 20 and 28 ms. (b) Effect of a 600 A RMP pulse on the toroidal velocities of C_{III}, O_V and C_{VI} impurities.

with the increase of the RMP current. The toroidal O_V and C_{VI} flows even reverse their directions at $I_{RMP} = 850$ A and 1.1 kA to the co-current direction (negative).

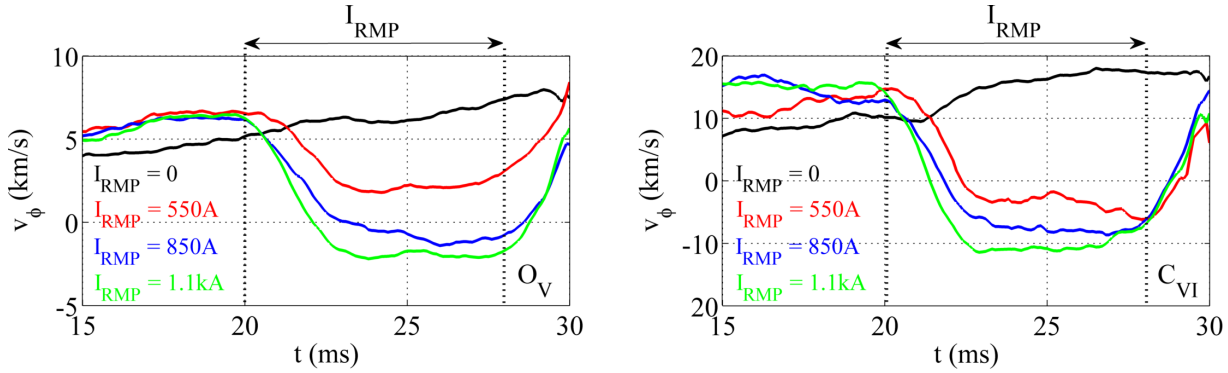

Figure 5.19: Modification of the toroidal flow velocities of O_V and C_{VI} impurities at several RMP currents. The RMP current is turned on at 20 ms for 8 ms. The tokamak discharge current is 20 kA.

The toroidal rotation of magnetic islands in STOR-M is in the counter-current direction, consistent with the impurity flow direction measured by the IDS system near the island location. The difference in the ion flow and magnetic island velocities is caused by the combination of diamagnetism and neutral damping effects. The ion velocity profile generally peaks inside the magnetic

island, resulting in flattening in the pressure gradient. The pressure flattening inside the island eliminates the diamagnetic term which leaves only the contribution of the $\mathbf{E} \times \mathbf{B}$ drift term in the ion flow velocity [208]. In STOR-M, larger RMP current induces stronger suppression in the magnetic fluctuations and greater change in the toroidal flow velocities. The frequency of magnetic islands and the toroidal flow velocity of O_V impurities are plotted in Figure 5.20(a) against the RMP current and the amplitude of MHD fluctuations (RMS value). The trend of modification against the RMP currents and the RMS values is the same for both the O_V flow velocity and the island frequency. The O_V flow velocity changes nearly linearly with the RMP current at low current values and shows some signs of saturation at larger RMP currents. When the RMP current is 1.1 kA, the velocity of the O_V flow changes from 5.3 km/s in the counter-current direction to 2.3 km/s in the co-current direction. The change in the C_{VI} flow velocity, shown in Figure 5.20(b), against the RMP currents and the RMS values of magnetic fluctuations is similar to that for O_V impurities.

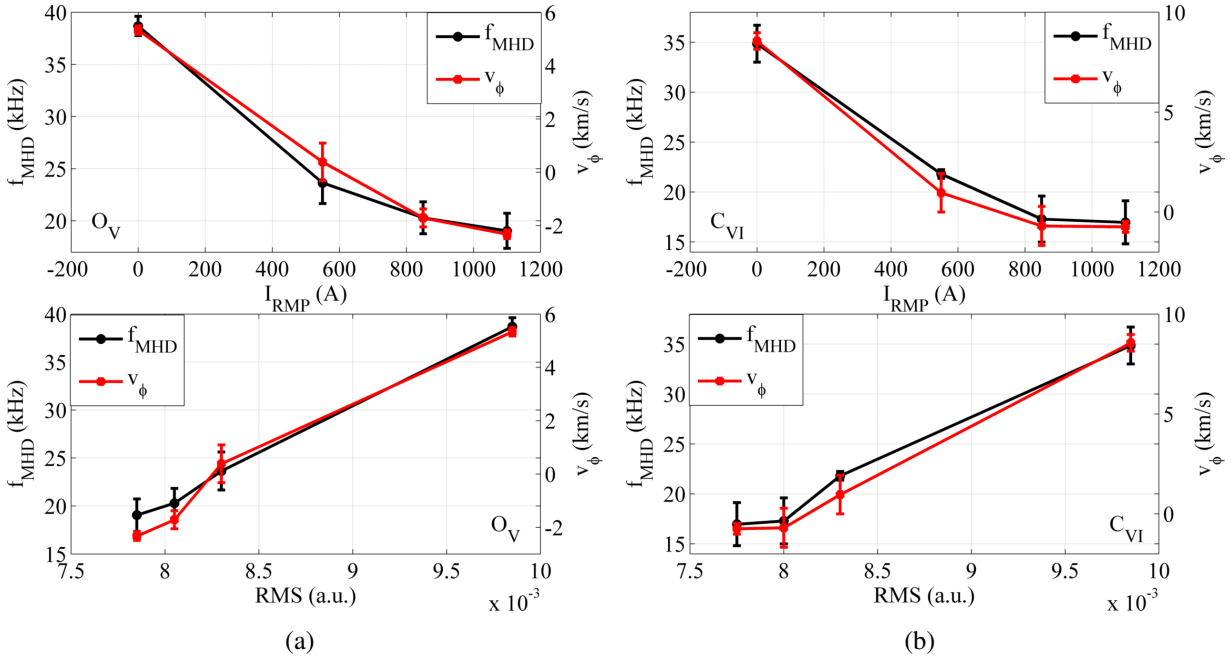

Figure 5.20: Comparison between the frequency of magnetic islands and the toroidal flow velocity of (a) O_V and (b) C_{VI} impurities as functions of the RMP current and the RMS value of magnetic fluctuations.

Another RMP experiment was conducted in STOR-M to demonstrate the possibility to continuously modulate the flow velocity by the double RMP (DRMP) pulse. During the ohmic discharge

#251349, the first RMP pulse was turned on at 15 ms for 3 ms and the second pulse with the same duration at 20 ms. The two pulses are separated by 2 ms. The traces of the DRMP pulse and a MHD fluctuation signal are shown in the top diagram of Figure 5.21. The fluctuations of (3, 1) island are dominant before applying the DRMP pulse. The wavelet spectrum of (3, 1) oscillations shown in the middle diagram of Figure 5.21 reveals a clear modulation in the MHD frequency and amplitude. The frequency of (3, 1) fluctuations drops significantly during DRMP and grows back after DRMP is turned off. The last diagram of Figure 5.21 shows the corresponding frequency and RMS value of MHD fluctuation amplitude, behaving similarly to the case with single RMP pulse in terms of the reduction in both frequency and amplitude.

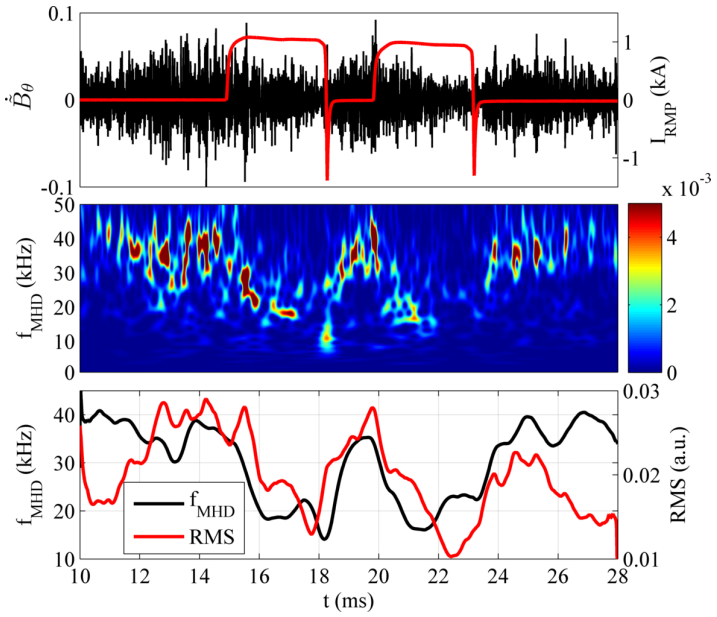

Figure 5.21: Effect of the DRMP pulse on the frequency and amplitude of MHD fluctuations during shot#251349.

Figure 5.22 shows the modulation of toroidal flow velocities of O_V and C_{VI} impurities induced by the DRMP pulse. The direction of the toroidal flow of O_V and C_{VI} impurity ions is in the counter-current direction before applying the DRMP pulse. As the first RMP pulse is turned on at 15 ms, the directions of O_V and C_{VI} flow velocities change towards the co-current direction and a greater change is observed with a larger RMP current. When the first RMP pulse is switched off at 18 ms, the toroidal flow velocities return to the original direction and amplitude. The second

RMP pulse applied at 20 ms induces a change in the flow velocities similar to that induced by the first RMP pulse. It is expected that a continuous modulation of flow velocity can be achieved with additional RMP pulses.

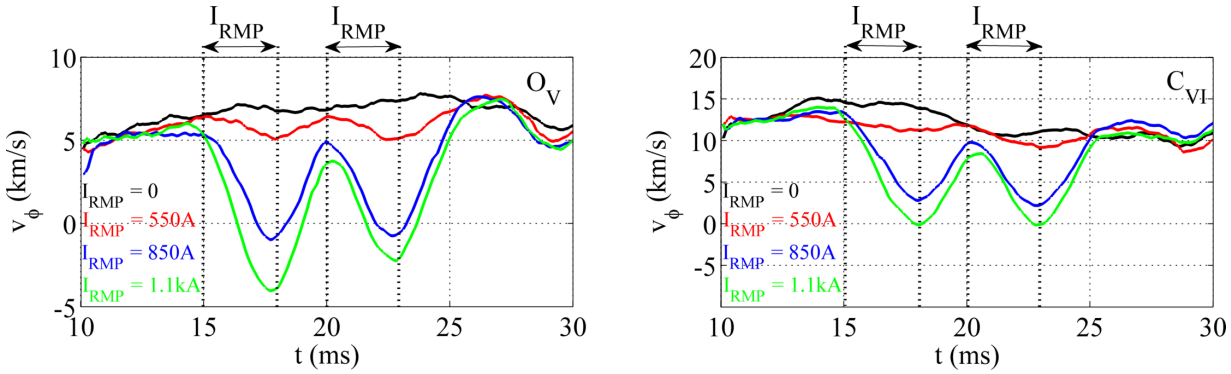

Figure 5.22: Modulation of toroidal flow velocities of O_V and C_{VI} impurities by the DRMP pulse. The 3 ms long RMP pulses are switched on at 15 and 20 ms.

Although the single and DRMP pulses have shown a consistent effect on the rotation of magnetic islands and impurity ions, the effect of non-resonant RMP (NRMP) pulse on the rotation of islands and impurity flow was quite different. As mentioned in Subsection 4.6.1, the NRMP configuration can be achieved by reversing the direction of the plasma current from counter-clockwise to clockwise (see Figure 4.7(a)), resulting in a helicity direction mismatch between the RMP windings and the helicity of magnetic field lines. The non-resonant interaction between the NRMP pulse and magnetic islands was studied during the STOR-M discharge #250060. The waveforms shown in Figure 5.23 are, from the top, the NRMP current (I_{NRMP}), a Mirnov signal, the wavelet spectrum of Mirnov signal, the frequency and RMS value of MHD fluctuations. The NRMP pulse is applied between 20 and 28 ms with a current magnitude of 1.1 kA.

The NRMP pulse induces some effects on MHD activities as seen by the amplitude reduction of the Mirnov signal. The spatial structure of the dominant magnetic island before firing NRMP is (3, 1) structure as extracted by the harmonic analysis. The reduction of (3, 1) amplitude is also visible in the wavelet spectrum, which is similar to the amplitude suppression observed during the previous RMP experiments. The (3, 1) frequency, however, responds differently to NRMP as it drops at slower rate compared with the RMP case. While the MHD frequency drops immediately

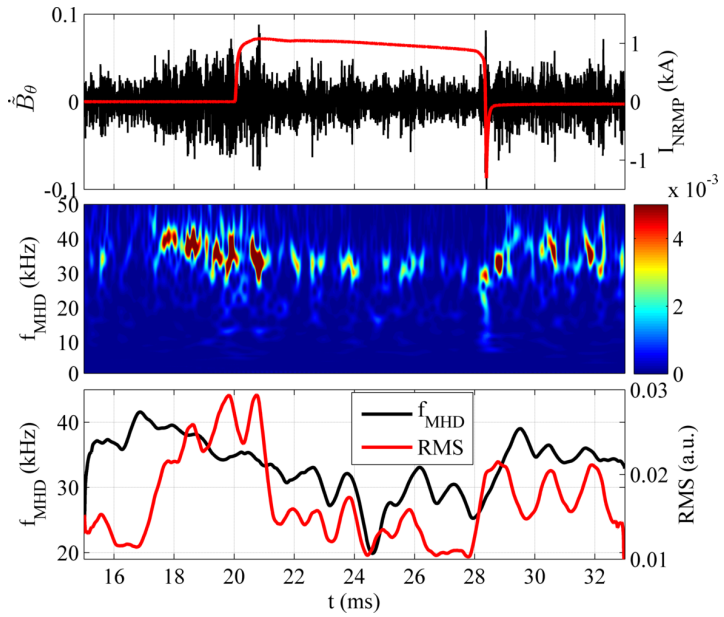

Figure 5.23: The non-resonant interaction between magnetic islands and NRMP during shot#250060. The NRMP pulse is applied at 20 for 8 ms. The NRMP current is around 1.1 kA.

from 40 to 20 kHz during the RMP pulse, it is slowly reduced from 40 to 30 kHz during the NRMP pulse. As a result, the magnetic island requires a longer time to slow down, suggesting that the island experiences different braking mechanism.

The application of NRMP field during STOR-M discharges causes a slight change in the toroidal flow of O_V and C_{VI} impurities. As shown in Figure 5.24, the base flow velocity without NRMP (black curves) is now reversed to the counter-clockwise direction (negative) and remains in the counter-current direction since the direction of plasma current is also reversed. The flow velocities of O_V and C_{VI} impurity ions at different NRMP currents are also shown in Figure 5.24. The NRMP pulse is applied between 20 and 28 ms. It is clear from the figure that the toroidal flow during NRMP is reduced only when the NRMP current is increased to a very high value of 1.1 kA.

5.4 Edge Plasma Measurements

The other effects of RMP on plasma parameters in STOR-M, particularly at the plasma edge and SOL regions, were investigated during an L-mode ohmic discharge #247580. The rake probe

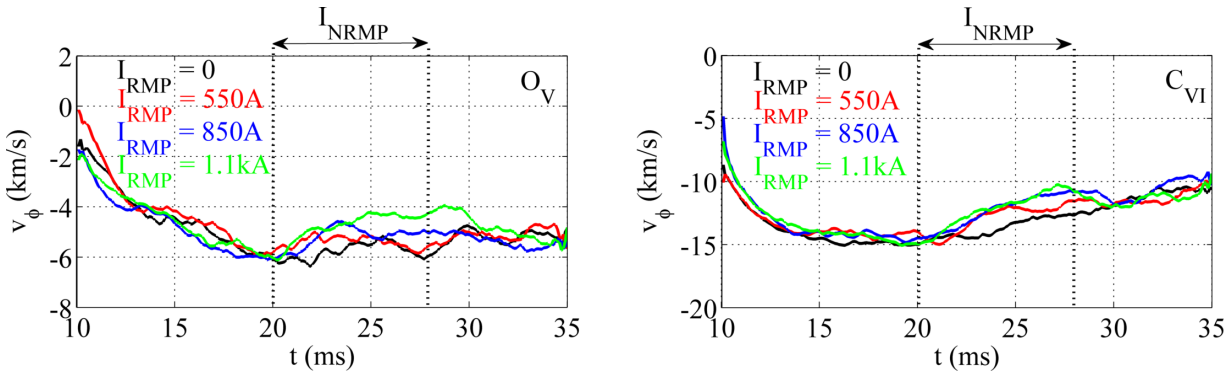

Figure 5.24: The flow measurements of O_V and C_{VI} impurity lines during the NRMP pulse. The NRMP current is fired at 20 ms for 8 ms.

described in Section 4.5 was used to measure the radial profiles of the ion saturation current (I_{si}) and the floating potential (V_f). Figure 5.25 shows from the top the time traces of MHD fluctuations, the RMP current waveform, the wavelet spectrum of MHD fluctuations, and the mean values of I_{si} and V_f signals obtained during the discharge. The RMP pulse is applied at 20 ms for 8 ms with a current magnitude of 1.1 kA. The harmonic analysis conducted on this discharge revealed that the (3, 1) mode, oscillating at a frequency of 40 kHz as illustrated in the wavelet spectrum, is dominant before applying RMP. When the RMP pulse is fired at 20 ms, the island is strongly suppressed and slowed down to a frequency of 20 kHz.

During the MHD suppression phase, the ion saturation current responds immediately to RMP and increases from 160 to 370 mA. Since the ion saturation current is the direct measure of the quantity $n_e\sqrt{T_e}$ (refer to Equation 4.3), there is a clear indication that the local edge density is increased by about 56%, assuming a constant temperature in the edge region during the discharge. The temperature measurements were absent in this experiment, however the average electron temperature at the edge region is in the range of 20 eV as reported in previous experiments conducted in STOR-M [127]. During the RMP pulse, the floating potential also experiences a change from $+20$ to -10 V. As the RMP current is terminated at 28 ms, the magnitudes of MHD fluctuations, I_{si} and V_f signals return to their original values prior to applying RMP.

The profiles of I_{si} can be obtained by moving the rake probe at different radial locations between a series of ohmic discharges with similar conditions. The radial profiles of I_{si} are constructed by

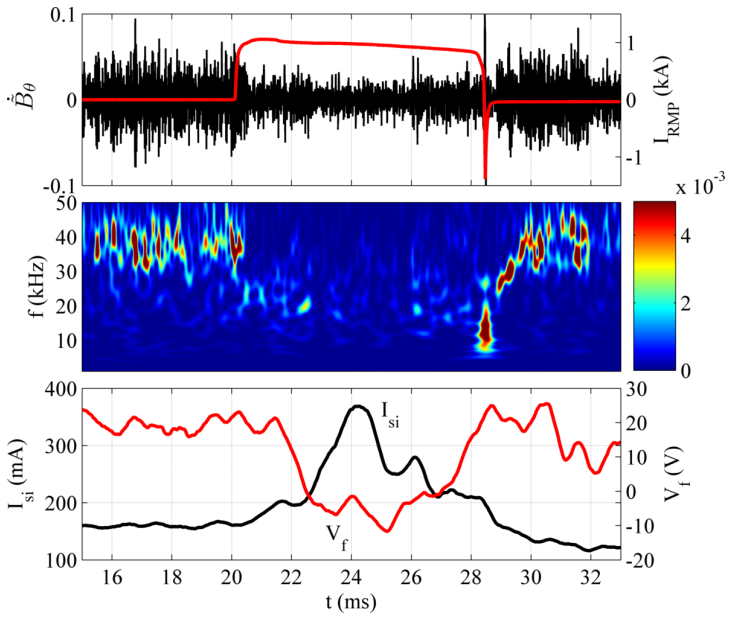

Figure 5.25: The influence of a single RMP pulse on MHD fluctuations, the ion saturation current I_{si} and the floating potential V_f during shot#247580. I_{si} and V_f signals are collected at $r = 11.5$ cm ($r/a = 0.95$). The RMP pulse is applied at 20 ms for 8 ms with a current magnitude of 1.1 kA.

averaging a 1 ms time window around the maximum value of I_{si} during the RMP pulse. The error bars are estimated by the standard deviation of all measured values at a particular position over a number of similar STOR-M discharges. Figure 5.26(a) shows the radial profiles of I_{si} and ΔI_{si} (the difference in I_{si} before and during RMP) between the radial locations $r = 11.5$ cm and $r = 12.75$ cm. The limiter is located approximately at $r = 12$ cm. There is a clear increase in the I_{si} values as the RMP current increases from 0 to 1.1 kA. The increase in the gradient of I_{si} profile suggests an increase in the gradient of plasma density n (and subsequently ∇p) at the edge and SOL regions. It seems that the increase is larger in the plasma edge than in SOL. The value of I_{si} at $r = 12$ cm along with the frequency of magnetic islands are plotted in Figure 5.26(b) against different RMP currents and RMS values of MHD fluctuations. The I_{si} value gradually increases with the increase of RMP current, consistent with the decrease of island frequency. I_{si} increases roughly from 165 mA at $I_{\text{RMP}} = 0$ to 300 mA at $I_{\text{RMP}} = 1.1$ kA, resulting in a 45% higher $n_e\sqrt{T_e}$ value at the plasma edge.

The rake probe was also used to measure the floating potential at different radial locations for various RMP currents. The radial profiles of V_f are constructed similarly by taking the average

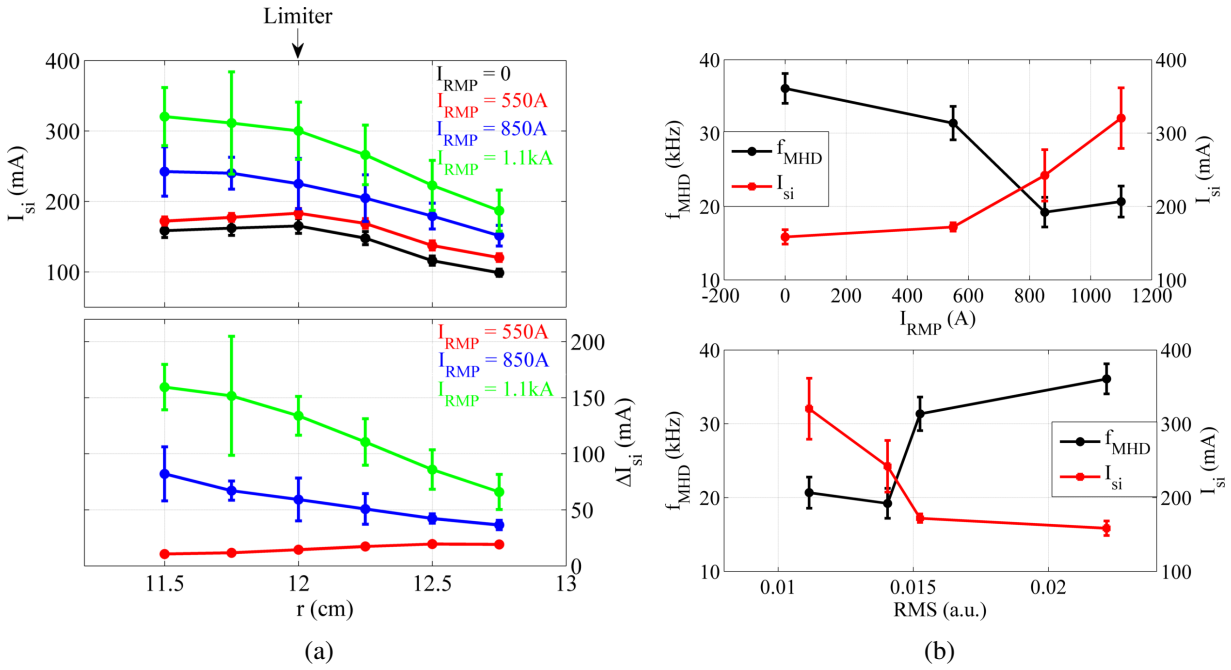

Figure 5.26: (a) Radial profiles of I_{si} and ΔI_{si} at different I_{RMP} values. (b) The frequency of magnetic islands and the value of I_{si} (at $r = 12$ cm) against different RMP currents and RMS values of MHD fluctuations.

value of a 1 ms time window around the minimum value of V_f at the same radial position of rake probe for a set of similar discharges. The standard deviation is used to estimate the error bars of all measured values at a fixed position over a number of similar discharges. The ΔV_f profiles are calculated by taking the difference in V_f values before and during RMP. The radial profiles of V_f and ΔV_f are shown in Figure 5.27(a). The figure shows that RMP not only reduces the magnitude of floating potential, but also modifies the gradient of V_f as the RMP current increases from 0 to 1.1 kA. As the V_f value drastically decreases with the increase in the RMP current, a negative E_r is generated near the limiter at 11.5 cm $< r <$ 12.5 cm. The modification of E_r is an expected result as the slowdown of plasma rotation by RMP causes a significant change in the $\mathbf{E} \times \mathbf{B}$ shear around the rational surfaces. Figure 5.27(b) shows the change of V_f (at $r = 12$ cm) and the MHD frequency with respect to the RMP currents and the RMS values of magnetic fluctuations. As I_{RMP} increases the value of V_f drops and more negative E_r is produced at the plasma periphery. V_f is reduced from $+11.3$ to -13.5 V as I_{RMP} increases from 0 to 1.1 kA.

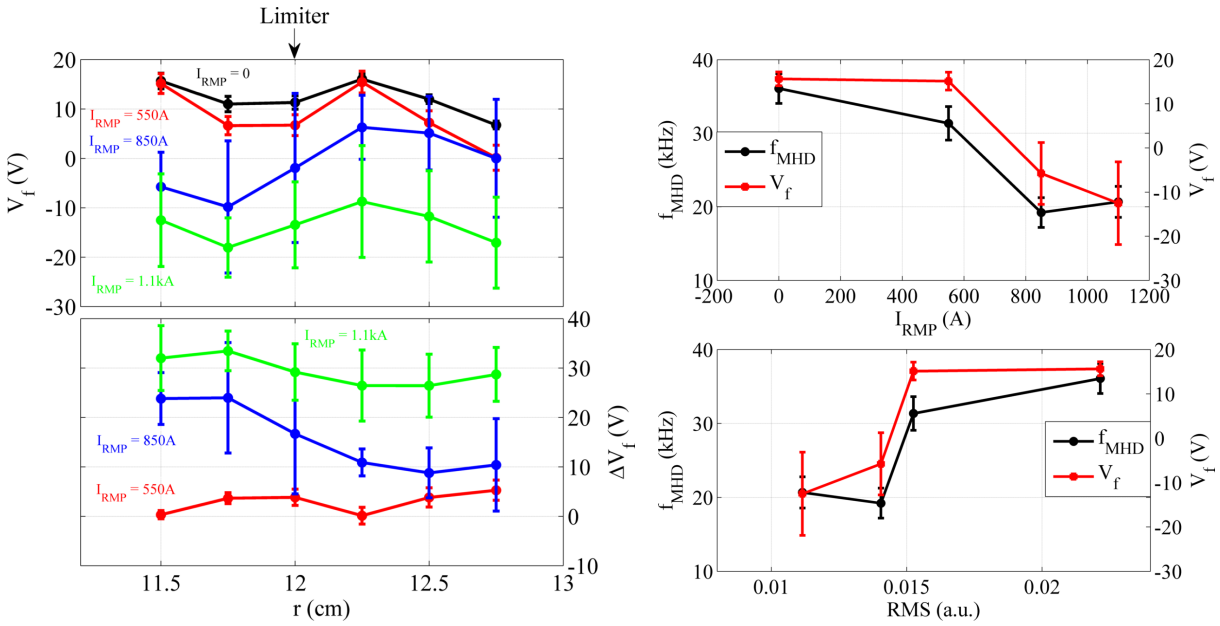

Figure 5.27: (a) Radial profiles of V_f and ΔV_f at different I_{RMP} values. (b) The frequency of magnetic islands and the V_f value (at $r = 12$ cm) against different RMP currents and RMS values of MHD fluctuations.

5.5 Plasma Response

The plasma response to the RMP field was experimentally measured in the STOR-M tokamak using the internal probe array described in Section 4.7. The plasma, like any conducting medium, is sensitive to external magnetic fields such as the RMP fields. The plasma responds to the RMP field by generating induction currents in the plasma. The induction currents in return modify the original magnetic topology of the RMP field. The plasma response to the RMP field is different from the plasma response to the vacuum field in tokamaks which is defined by the Grad-Shafranov equation.

Before carrying out the measurements of plasma response, the internal probe array was first tested in STOR-M without RMP. The local magnetic fluctuations were measured by moving the internal array at different radial locations between discharges. In the following experiments the original limiter was replaced by a new one installed at $r = 13$ cm. Figure 5.28 shows the RMS values of magnetic fluctuations and the local poloidal field B_θ at the plasma edge ($r = 11$ cm), the

limiter ($r = 13$ cm) and the SOL region ($r = 15$ cm). The local poloidal field is plotted with the plasma current I_p in the same diagram for comparison. The RMS values indicate that the magnetic fluctuations are higher in the plasma edge and lower in the SOL region. The RMS values are tripled as the probe array is moved from $r = 15$ cm to $r = 11$ cm. The poloidal field also increases as the probe array is moved from the SOL region to the plasma edge. The waveforms of B_θ and I_p are similar because the two quantities are mutually proportional (see Equation 5.13).

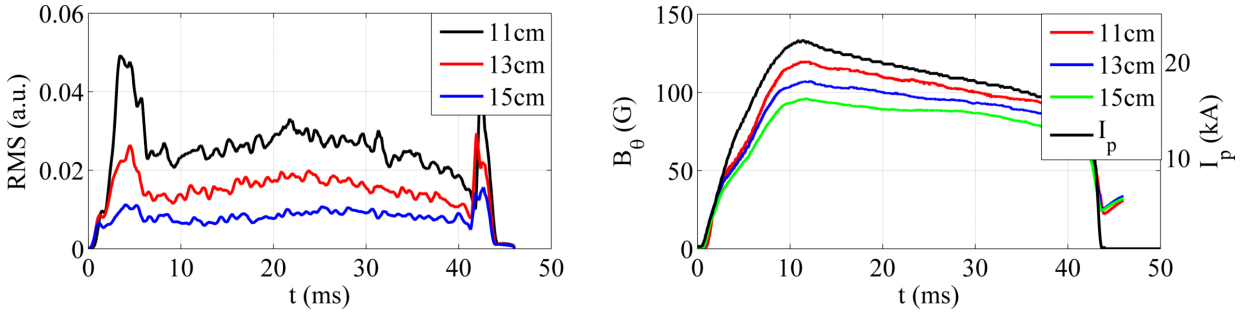

Figure 5.28: Time traces of the RMS value and the poloidal magnetic field at different radial locations. The poloidal field is plotted with the I_p waveform in the same diagram for comparison.

The radial profiles of the RMS values and the local poloidal field are shown in Figure 5.29. The radial profiles of RMS and B_θ are constructed by moving the internal magnetic probes between discharges from $r = 21$ cm (outside the vacuum chamber) to $r = 8.5$ cm (inside the plasma). The RMS value increases from almost zero outside the vacuum chamber to 0.056 inside the plasma. The local poloidal field gradually increases as the probe array is moved deeper into the plasma. However, the poloidal field drastically increases from 128 G to 182 G as the innermost probe is moved from 9 to 8.5 cm.

The plasma response measurements were carried out for a series of ohmic discharges with an RMP pulse fired during the plasma flat-top. The discharges have similar plasma parameters ($I_p =$ 20 kA, $V_l = 3$ V, $q(a) = 4.5$). The RMP pulse was applied between 15 and 22 ms with a current magnitude of 1 kA. Figure 5.30 shows the waveforms of RMS and the poloidal field at different radial locations (11, 13, and 15 cm). Slight reduction can be seen on the RMS waveforms during the RMP pulse, indicating the suppression of MHD fluctuation signals. The reduction is more clear at smaller radius ($r = 11$ cm) compared with that at outer location ($r = 15$ cm). The local poloidal

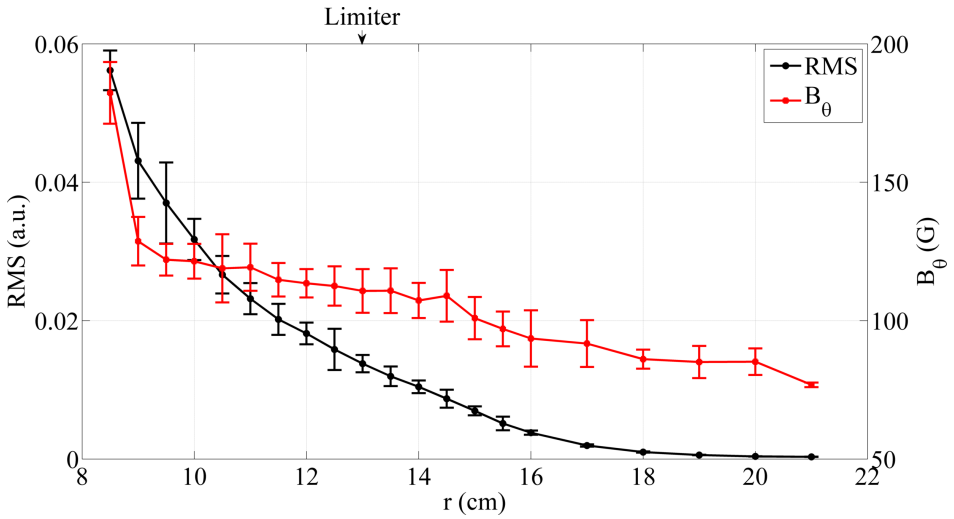

Figure 5.29: Radial profiles of the RMS values and the poloidal field. The limiter is located at 13 cm.

field is also reduced during the RMP pulse. The poloidal field is reduced by almost 20% in the edge and limiter regions, and by only 15% in the SOL region. The reduction in the local poloidal field is caused by the sign difference between the total plasma field and the RMP field.

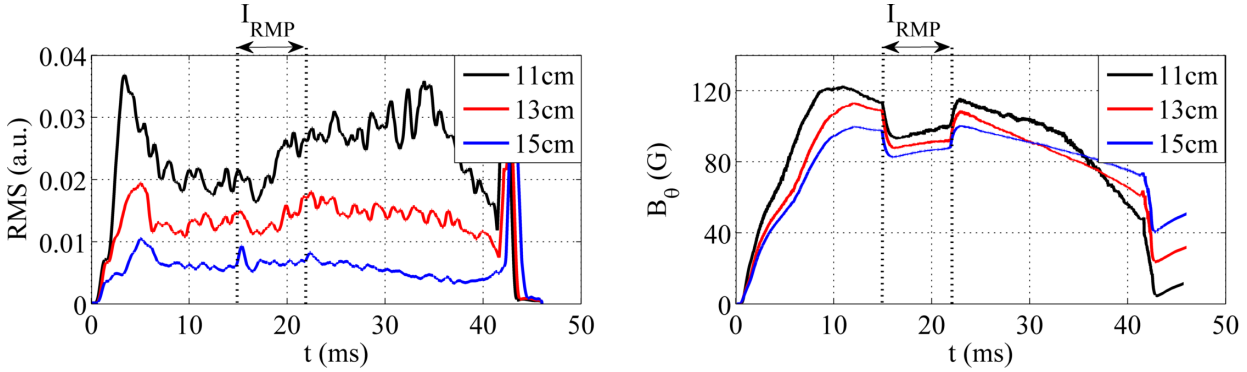

Figure 5.30: Time traces of RMS and B_θ at different radial locations during the RMP pulse. The RMP current is about 1 kA applied between 15 and 22 ms.

Figure 5.31 shows the radial profiles of the RMS values and the poloidal field with and without the RMP field. The RMS profiles with and without RMP are nearly the same outside the plasma (r = 15-16 cm). The RMS profiles, however, diverge near the limiter. The difference between the RMS profiles at the radial location r = 11.5 cm is more apparent ($\sim$ 12%). The radial profiles of local poloidal field with and without RMP are also similar outside the plasma, and diverge in the region around the limiter. The difference in B_θ profiles is consistent throughout the edge region ($\sim$

18%), contrary to the RMS profiles.

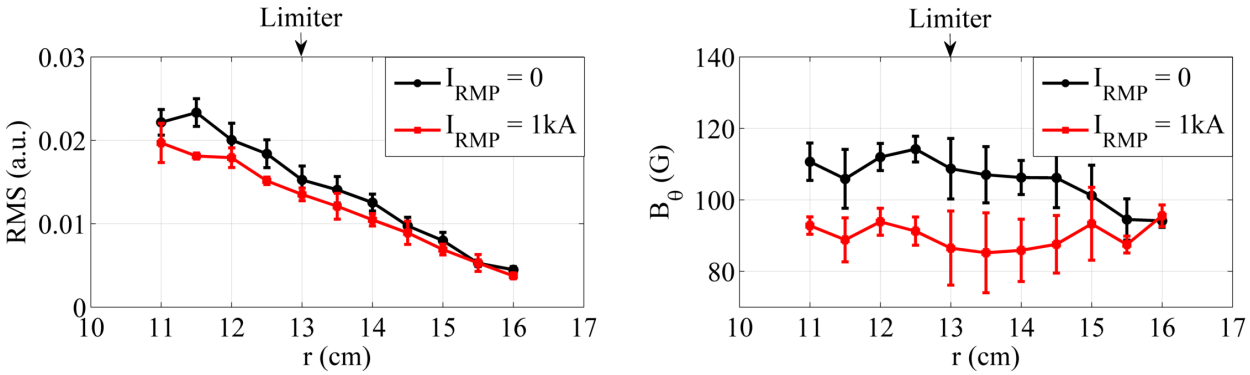

Figure 5.31: Radial profiles of RMS and B_θ with and without the RMP field.

The plasma response to the RMP field is plotted at three radial locations (11, 13, and 15 cm) in Figure 5.32(a). The RMP pulse is about 1 kA and applied at 15 ms for a duration of 7 ms. The plasma response (B_p) is calculated by measuring the vacuum field (B_v) in the presence of RMP at one radial location and subtracting it from the total magnetic field (B_{tot}) measured at that location. The plasma response during the RMP pulse is about 85 G in the SOL region (r = 15 cm) and increases respectively by 20% and 40% in the limiter and edge regions. Figure 5.32(b) shows the radial profiles of the total field B_{tot}, the plasma response B_p, and the vacuum field B_v during the RMP flat-top. The B_p profile is higher than the B_{tot} profile because the total and the vacuum fields are in opposite direction. The polarity of the vacuum field is reversed from positive outside the vacuum chamber (r = 16 cm) to negative inside the vacuum chamber (r = 11-15.5 cm), resulting in a higher plasma response compared with the total field.

5.6 RMP Penetration

The RMP propagation in STOR-M was examined using the internal probe array. A 2 kA FRMP pulse was applied at 18 ms for a duration of 400 μs. The FRMP field was fired 3 ms after applying a 1 kA SRMP with a duration of 7 ms. The FRMP propagation was studied in both vacuum and plasma. Figure 5.33(a) shows the waveform of the FRMP pulse along with the probe signals at different radial locations in vacuum. The magnetic signals are integrated numerically between

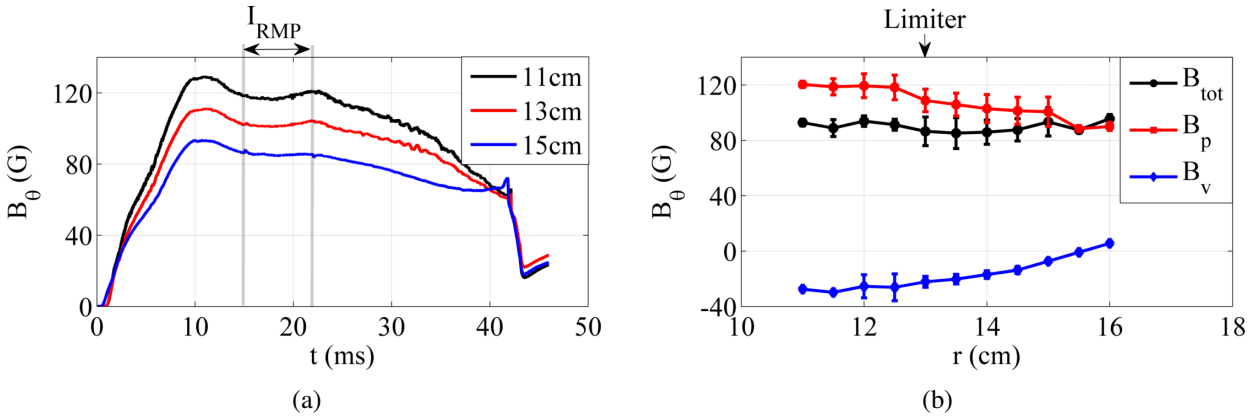

Figure 5.32: (a) Plasma response at different radial locations to a 1 kA RMP pulse fired at 15 ms for 7 ms. (b) Radial profiles of the total magnetic field B_{tot}, the plasma response B_p, and the vacuum field B_v during the RMP pulse.

17.5-19 ms (during the SRMP flat-top). There is a time delay between the FRMP pulse and the probe signals which has also been observed while calibrating the probes (see Section 4.7). The time delay is associated with either the slow response time of probes or the numerical integration of signals. This discrepancy should be eliminated in future experiments. The delay increases as the probes are moved away from the RMP windings which are located outside the vacuum chamber at $r = 17$ cm. The waveforms of the FRMP pulse and the probe signals at different radial locations in plasma are shown in Figure 5.33(b). The time delay is also clear between the FRMP pulse waveform and the probe signals. However, the delay seems shorter compared with the vacuum case. The probe signals at $r = 11$ cm experience different time delays in vacuum and plasma as the delay in vacuum (177 μs) is higher than that in plasma (158 μs). The probe signals, however, experience the same time delay (148 μs) at the limiter ($r = 13$ cm).

The radial profiles of time delay (τ) between the magnetic signals and the FRMP pulse in plasma (τ_p) and vacuum (τ_v) are shown in Figure 5.34(a). The black curve in the figure is the difference between the time delays in vacuum and plasma. The time difference remains nearly constant in the SOL region and increases in the plasma edge. Figure 5.34(b) shows the radial profiles of time difference (ΔT) between two adjacent probe signals in plasma (ΔT_p) and vacuum (ΔT_v). The time differences in plasma and vacuum are similar in the SOL region, implying that the

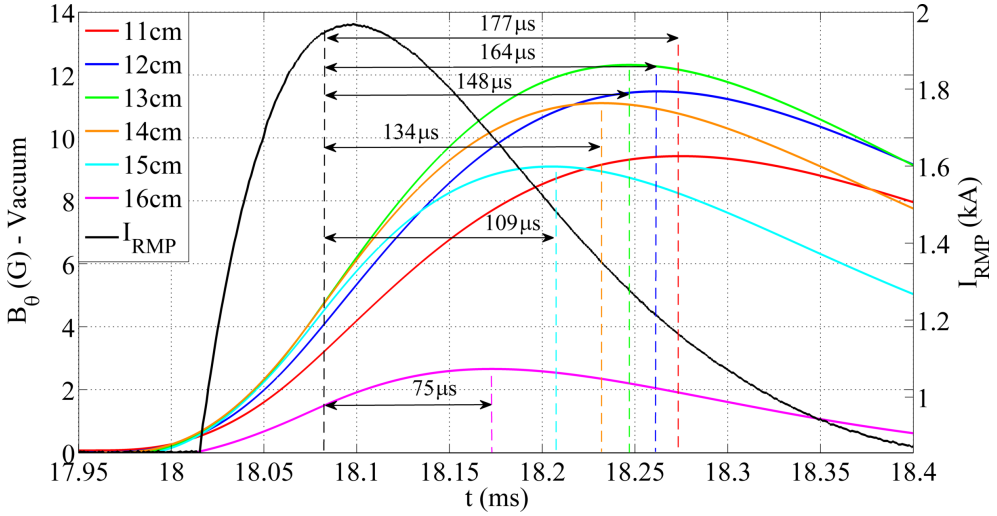

(a)

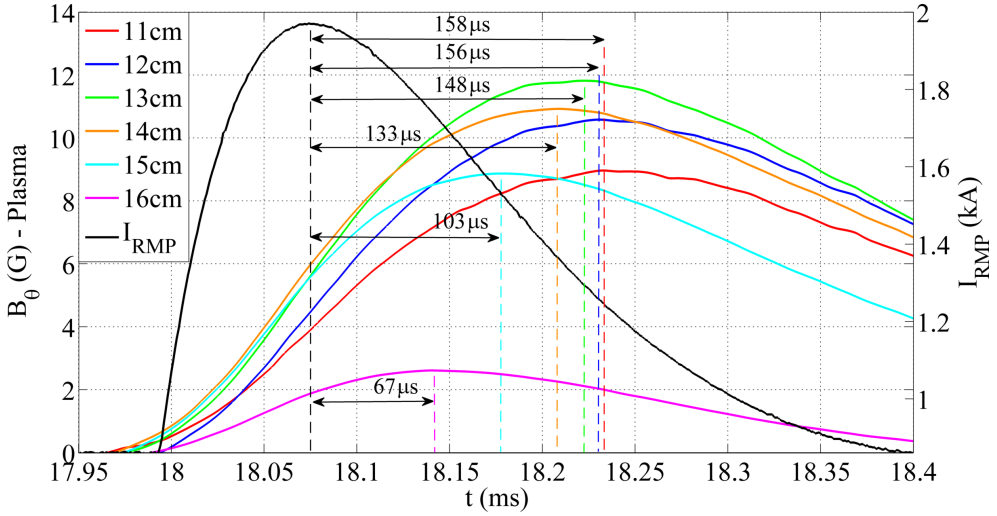

(b)

Figure 5.33: Waveforms of FRMP current (black line) and integrated magnetic signals at different radial locations in (a) vacuum and (b) plasma. The FRMP pulse is fired around 18 ms (3 ms during the SRMP pulse) for a duration of 400 μs.

FRMP pulse travels at the same speed in both cases. However, The ΔT profiles in the edge region suggest that the FRMP pulse propagates differently in plasma and vacuum.

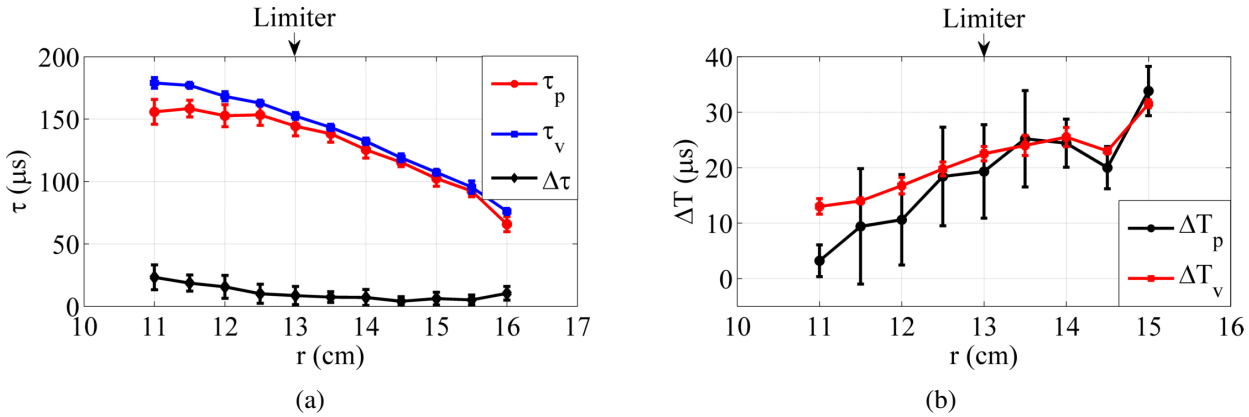

Figure 5.34: (a) Radial profiles of time delay (τ) in plasma and vacuum. (b) Radial profiles of time difference (ΔT) between two adjacent probes in plasma and vacuum.

Figure 5.35(a) shows the radial profiles of the peak values of magnetic signals in plasma (B_p) and vacuum (B_v). The radial profiles gradually increase in the SOL region and peak at the limiter region ($r = 13$ cm) before they decay at the plasma edge. The radial profiles of B_p and B_v are similar in the SOL region and diverge at the edge region. The B_p profile is lower than the B_v profile at the plasma edge, suggesting that the FRMP pulse is attenuated and screened by the plasma. Figure 5.35(b) shows the radial profiles of the difference in signal peaks for two adjacent magnetic probes in plasma (ΔB_p) and vacuum (ΔB_v) during the FRMP pulse. The radial profiles of ΔB_p and ΔB_v are reduced at the same rate as the FRMP pulse penetrates deeper into the plasma. The radial profiles change their sign at the edge region, indicating that the FRMP pulse experiences more attenuation in that region.

Figures 5.36(a) and (b) are contour and 3D plots of the signal peaks in the plasma during a FRMP pulse. The FRMP current is about 2 kA and fired at 18 ms for a duration of 0.4 ms. The limiter location is represented by the horizontal dashed line at $r = 13$ cm. The time delay between the signal peaks and the FRMP pulse is illustrated by the slope of the dashed black line on the contour plot. The time delay increases as the FRMP pulse travels deeper into the plasma. The radial distribution of signal peaks is uniformly centered around the limiter region.

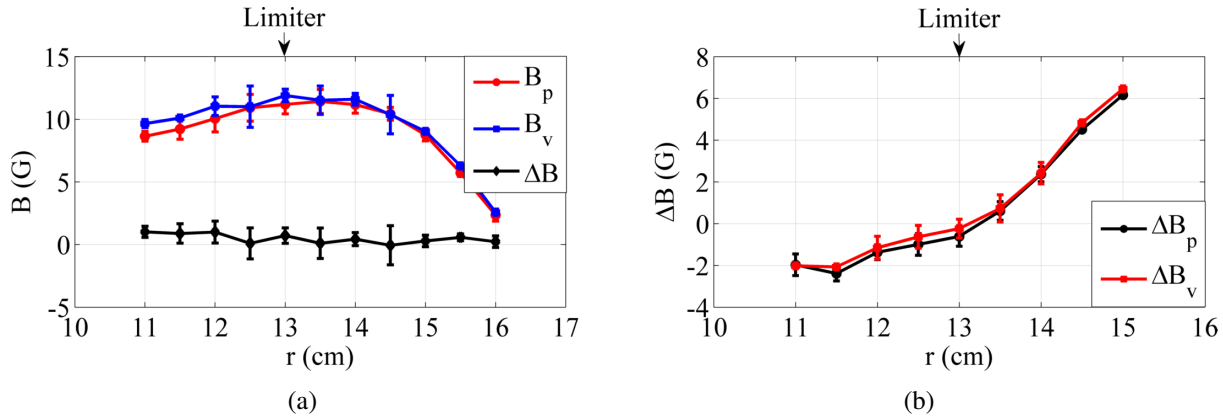

Figure 5.35: (a) Radial profiles of signal peaks during the FRMP pulse in plasma and vacuum. (b) Radial profiles of the difference in signal peaks of two adjacent probes during the FRMP pulse in plasma and vacuum.

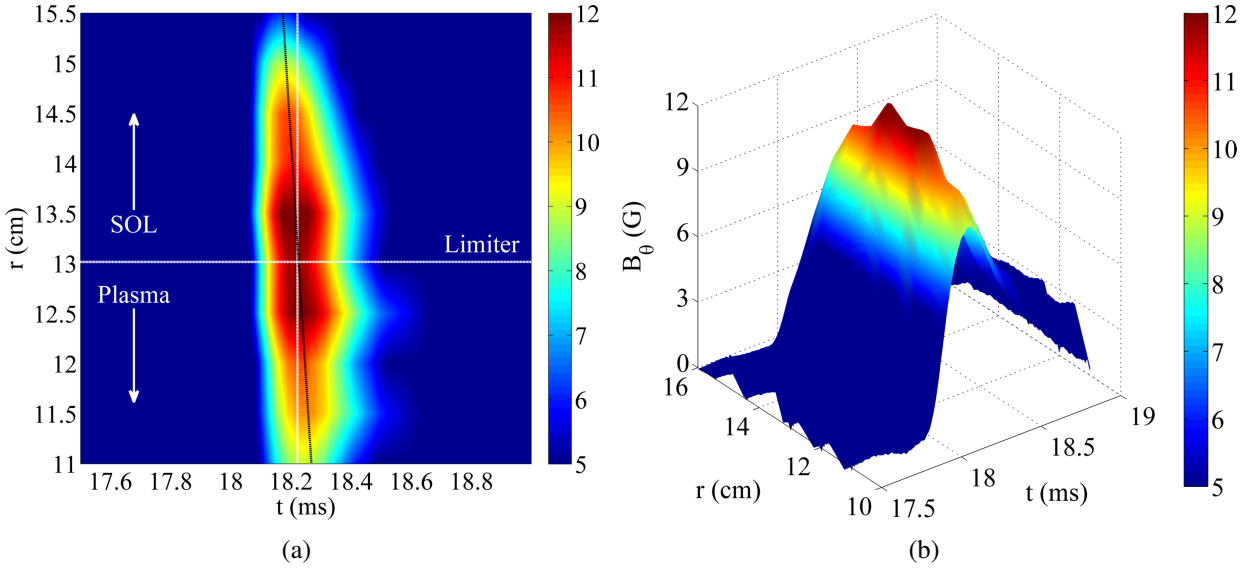

Figure 5.36: (a) Contour and (b) 3D plots of the signal peaks in plasma during a FRMP pulse fired at 18 ms.

Chapter 6

Summary and Suggested Future Work

6.1 Summary

Active control of MHD instabilities and other plasma parameters, such as the plasma rotation, has been an intriguing topic in the fusion energy research. One of the promising techniques developed for this purpose involves the use of RMP fields. RMP has been successfully used for the ELM mitigation and the error field correction. RMP has also been implemented in many applications in tokamaks such as modifying the edge transport, controlling the plasma rotation, and suppressing the tearing modes and the runaway electrons. The RMP technique was successfully implemented in the STOR-M tokamak. The RMP system in STOR-M consists of ($l = 2$, $n = 1$) helical coils powered by a set of capacitor banks and gated by IGBT and SCR switches. Experimental studies were carried out in the STOR-M tokamak to investigate the effects of RMP on the tokamak plasma, particularly on the tearing modes, the plasma rotation, and plasma parameters in the edge and SOL regions. An internal magnetic probe array was also used to study the plasma response and the RMP penetration in STOR-M.

The use of external resonant helical windings is made in the STOR-M tokamak to generate magnetic field perturbations with (2, 1) helical structures which are used to control MHD instabilities, particularly the tearing instabilities associated with the magnetic islands. It is found that externally applied helical fields during STOR-M discharges could effectively interact with magnetic islands of

the same helicity, leading to the suppression of MHD activities. A significant reduction in Mirnov oscillation frequencies is observed in STOR-M as the magnitude of RMP is increased. The resonant condition, however, cannot be established when the applied helical fields and tearing modes have opposite helicity configurations. It is demonstrated experimentally in other tokamak machines that as the RMP magnitude increased, a critical current limit is exceeded at which a disruptive-like instability is triggered.

The interplay between RMP and magnetic islands was simulated for different STOR-M discharge conditions. The simulation was conducted for three equilibrium states of STOR-M with different I_p (20 kA, 22.5 kA and 25 kA) and the same B_ϕ (0.575 T), corresponding to different edge safety factors $q(a)$ (4.5, 4 and 3.6, respectively) in STOR-M. In this simulation, different RMP currents were tested to estimate the required critical I_{RMP} to completely suppress a (2, 1) magnetic island. In the first case with $q(a) = 4.5$, the RMP currents did not exhibit any significant influence on the $q = 2$ surface due to the fact that the island superimposed on that surface was located deep inside the plasma core and far away from the RMP coils. However, when the $q(a)$ value was lowered to 4 in the second case, the (2, 1) island was successfully suppressed by the RMP field. The critical amount of I_{RMP} required to eliminate the island was about 8.8% of the total plasma current. In the third case, a further decrease in $q(a)$ to 3.6 reduced the threshold of the helical current required to eliminate the (2, 1) island to 6.4% of I_p, which qualitatively agreed with the experimental observations made in other tokamaks. Moreover, an island with (2, 1) helical structure was produced when the helical current exceeded a critical limit, which may disrupt a real tokamak discharge in a manner similar to the disruptive instabilities. This condition has not been tested due to the current limitation of IGBT switches.

The influence of RMP was investigated experimentally in STOR-M during a low-q ohmic discharge ($I_p = 23.5$ kA, $V_l = 3.5$ V, $q(a) = 3.7$). During a phase with rich Mirnov activities, a short RMP pulse ($\sim 2.5\%$ of I_p) was applied for 2 ms at approximately 20 ms during the plasma flat-top region. A clear reduction in loop voltage V_l and H_α traces was observed 0.7 ms after application of RMP. The effect of RMP was more pronounced on Mirnov signals as the fluctuation amplitude

and frequency of MHD oscillations were remarkably reduced. The harmonic analysis performed around the time of firing RMP revealed that the amplitude of $m = 2$ dropped by about 90% while only by 65-75% for $m = 1$, $m = 3$ and $m = 4$ fluctuation modes. It was inferred that the $m = 3$ mode was predominant during the MHD suppression phase before the $m = 2$ oscillations dominated the discharge again when the RMP field was turned off. The wavelet spectrum analysis revealed that both SXR and Mirnov oscillations were strongly coherent at a frequency of 25 kHz before and after applying RMP. During the MHD suppression phase, high SXR emissions were observed by central SXR chords, owing to improved plasma confinement.

A theoretical study was carried out to investigate the mechanisms that determine the rotation frequency of MHD modes in STOR-M. The plasma profiles required for the study, such as density, temperature and pressure profiles, were constructed using the Kadomtsev-Tayler model. Various assumptions were considered for the MHD frequency observed in STOR-M. In previous theoretical works, it has been reported that different combinations of poloidal, toroidal, and electron diamagnetic frequencies might provide an explanation for the observed MHD frequency in tokamaks. The poloidal and toroidal rotation frequencies were calculated by the neoclassical rotation theory which does not take into consideration the velocity of impurities. A comparison between the theoretical MHD frequencies and the experimental MHD frequency of (3, 1) island revealed that the MHD rotation in STOR-M is mainly governed by the electron diamagnetic rotation and changes with the toroidal rotation of impurity ions. However, due to the absence of poloidal flow measurements in STOR-M, it is still inconclusive if the poloidal rotation is significant enough to contribute to the MHD frequency in STOR-M.

The toroidal plasma flow in STOR-M was experimentally studied under the influence of RMP field. It was observed that the toroidal flow could be significantly modified by RMP fields. The toroidal flow measurements were conducted in STOR-M using the IDS system which utilizes the line emission from selected impurity ions (namely C_{III}, O_V and C_{VI} ions) to calculate the toroidal flow velocity at different radial locations. The experiments were carried out using resonant and non-resonant RMP configurations. It was observed that RMP not only reduced the amplitude and

frequency of magnetic islands, but also modified the toroidal plasma flow. The flow measurements of C_{III}, O_V and C_{VI} impurity lines revealed that the flow direction changed towards the co-current direction during RMP. The change in the flow velocity of O_V and C_{VI} impurity ions behaved consistently with the change in the frequency of magnetic islands. The flow velocity and the island frequency were both reduced at the same rate during RMP. The reduction was nearly proportional to the RMP current when $I_{\text{RMP}} < 850$ A, and showed some saturation with further increase in I_{RMP}. Similar observations were made during the double RMP experiments. The NRMP field, however, interacted differently with the plasma. Despite the reduction in the island frequency during NRMP, the reduction in the toroidal flow velocity seemed insignificant even at high NRMP currents.

The modification of the ion saturation current and the floating potential was investigated by the rake probe in the presence of the RMP field. The radial profile of I_{si} increased at the plasma edge and the SOL region as the RMP current increased, indicating an improved confinement accompanied by an enhanced pressure gradient at the edge region. RMP also reduced and modified V_f profile, generating more negative radial electric field E_r near the limiter. The modification of E_r was attributed to the change in the $\mathbf{E} \times \mathbf{B}$ shear rate caused by the spin-down of plasma rotation.

The internal probe array was used to study the plasma response and the RMP penetration in STOR-M. The plasma response was obtained by measuring the vacuum field (including the RMP field) at a particular radial location and subtracting it from the total field at that location. The plasma response was found to be higher than the total field due to the polarity difference between the vacuum and the total fields. The propagation of RMP was also studied in vacuum and plasma. More experimental work is needed to interpret the results of this experiment due to the systematic time delay between the RMP field and the magnetic signals collected by the internal array. The time delay was believed to be caused by either the slow response time of probes or the numerical integration of signals.

6.2 Suggested Future Work

The RMP system developed for the STOR-M tokamak in this research will facilitate the RMP studies in future experiments. Further experiments have already been planned to study the effects of RMP on the plasma rotation using the SRMP and FRMP pulses. The SRMP pulse will be used for setting a specific plasma rotation speed, whereas the FRMP pulse will be used to study the penetration of the RMP field at the preset rotation speed. It has also been planned to study the effects of edge safety factor $q(a)$ on the effectiveness of RMP by changing the plasma current and/or toroidal magnetic field. Changing the edge safety factor will change the radial location of $m = 2$ island which will determine the distance between the $m = 2$ island and the RMP coils.

The existing helical RMP coils will be replaced with discrete saddle coils like those installed in the J-TEXT tokamak [209]. The saddle coils are easy to install and maintain, unlike the helical coils installed now in STOR-M. Due to the existence of several large ports in STOR-M, installing helical windings of selected modes around the tokamak chamber with high accuracy has been difficult. Discrete saddle coils will be designed, fabricated and installed outside the STOR-M vacuum vessel. Combinations of currents passing through coils with various amplitudes and polarities provide a convenient means to produce any desired dominant modes of RMP. The plan is to install 8 poloidal by 4 toroidal coil arrays. Each coil will be driven by an off-shelf professional audio amplifier, similar to an arrangement on the EXTRAP T2R reversed field pinch device [210]. The advantage of discrete saddle coils for generating radial magnetic field is the possibility for feedback control of MHD modes if the sensing coils are installed and the data analyzed in real-time. The previous experience of feedback control of the STOR-M tokamak plasma position using fuzzy logic algorithm [139] will be extended to feedback control of MHD instabilities in STOR-M.

The internal probe array is currently installed on STOR-M and ready for use in any future experiments. The internal probe array was successfully used to measure the plasma response to the RMP fields. However, the slow response time of probe array affected the measurements of RMP penetration. The response time of probe array has to be improved by redesigning the probe array and the associated electronics.

Bibliography

[1] A. Pasternak, *Global Energy Futures and Human Development: A Framework for Analysis*, US Department of Energy Report UCRL-ID-140773, Lawrence Livermore National Laboratory, Livermore, CA (2000).

[2] S. Barabashi *et al.*, *Fusion Programme Evaluation*, UR 17521, Office for Official Publications of the EU, Luxembourg (1996).

[3] ITER: http://www.iter.org/.

[4] F. F. Cap, *Handbook on Plasma Instabilities: Volume 1*, Academic Press (1976).

[5] J. Wesson, *Tokamaks 4th Ed*, Oxford University Press (2011).

[6] K. Miyamoto, *Controlled Fusion and Plasma Physics*, Tylor and Francis (2007).

[7] S. Nakai and H. Takabe, Rep. Prog. Phys. **59**, 1071 (1996).

[8] A. L. Bezbatchenko, I. N. Golovin, P. I. Kozlov *et al*., Plasma Physics and Problems of Controlled Fusion **1**, 116 (1955).

[9] H. J. de Blank, Trans. Fusion Sci. Technol. **49**, 118 (2006).

[10] R. Fitzpatrick and F. L. Waelbroeck, Phys. Plasmas **15**, 012502 (2008).

[11] A. Sykes and J. A. Wesson, Phys. Rev. Lett. **44**, 1215 (1980).

[12] S. V. Mirnov and I. B. Semenov, At. Energ., USSR **30**, 20 (1971).

[13] S. Von Goeler, W. Stodiek and N. Sauthoff, Phys. Rev. Lett. **33**, 1201 (1974).

[14] I. H. Tan, I. L. Caldas, I. C. Nascimento, R. P. Silva, E. K. Sanada and R. Bruha, IEEE Transactions on Plasma Science **PS-14**, 279 (1986).

[15] Zhen Xiangjun, Hu Liqun, Wan Baonian *et al*., Plasma Sci. Technol. **8**, 147 (2006).

[16] D. E. Roberts, J. A. M. DeVilliers, J. D. Fletcher *et al*., Nucl. Fusion **26**, 785 (1986).

[17] P. V. Savrukhin, E. S. Lyadina, D. A. Martynov *et al*., Nucl. Fusion **34**, 317 (1994).

[18] B. V. Waddell, B. Carreras, H. R. Hicks *et al*., Phys. Rev. Lett. **41**, 1386 (1978).

[19] F. Karger, H. Wobig, S. Corti *et al.*, IAEA Proc. 5th Int. Conf. on Plasma Physics and Controlled Nuclear Fusion **1**, 207 (1974).

[20] Qiming Hu, Bo Rao, Q. Yu *et al*., Phys. Plasmas **20**, 092502 (2013).

[21] T. N. Todd, Nucl. Fusion **32**, 1071 (1992).

[22] F. Karger, H. Wobig, S. Corti *et al.*, in Plasma Physics and Controlled Nuclear Fusion Energy Research, Proceedings of 5th IAEA Int. Conf. Tokyo, 1974, **1**, 207 (1975).

[23] K. Bol, J. L. Cecchi, C. C. Daughney *et al.*, in Plasma Physics and Controlled Nuclear Fusion Energy Research, Proceedings of 5th IAEA Int. Conf. Tokyo, 1974, **1**, 83 (1975).

[24] N. V. Ivanov and A. M. Kakurin, Sov. J. Plasma Phys. **5**, 54 (1979).

[25] Jiayu Chen, Jikang Xie, Yuping Huo *et al.*, Nucl. Fusion **30**, 2271 (1990).

[26] H. Franco, C. Ribeiro, R. P. da Silva *et al.*, Rev. Sci. Instrum. **63**, 3710 (1992).

[27] D. E. Roberts, J. D. Fletcher, D. Sherwell *et al.*, in Controlled Fusion and Plasma Physics, Proceedings of 16th Eur. Conf. Venice, 1989, **13B**, Part II, European Physical Society, 493 (1989).

[28] A. W. Morris, S. Arshad, C. Balkwill *et al.*, in Controlled Fusion and Plasma Physics, Proceedings of 16th Eur. Conf. Venice, 1989, **13B**, Part II, European Physical Society, 541 (1989).

[29] G. Nothnagel, D. Sherwell, J. D. Fletcher *et al.*, in Controlled Fusion and Plasma Physics, Proceedings of 16th Eur. Conf. Venice, 1989, **13B**, Part II, European Physical Society, 489 (1989).

[30] K. M. McGuire and D. C. Robinson, in Controlled Fusion and Plasma Physics, Proceedings of 9th Eur. Conf. Oxford, 1979, European Physical Society, 93 (1980).

[31] F. Karger, W. Feneberg, J. Gernhardt *et al.*, in Controlled Fusion and Plasma Physics, Proceedings of 8th Eur. Conf. Prague, 1977, **1**, European Physical Society, 3 (1977).

[32] D. E. Roberts, J. D. Fletcher, G. Nothnagel *et al.*, Phys. Rev. Lett. **66**, 2875 (1991).

[33] I. L. Caldas, O. W. Bender, M. V. Fernandes *et al.*, Rep. IFUSP/P654 Univ. São Paulo (1987).

[34] V. V. Arsenin, L. I. Artemenkov, N. V. Ivanov *et al.*, in Plasma Physics and Controlled Nuclear Fusion Energy Research, Proceedings of 7th IAEA Int. Conf. Innsbruck, 1978, **1**, 233 (1979).

[35] T. Zhang, Y. Liang, Y. Sun *et al*., Nucl. Fusion **52**, 074013 (2012).

[36] Bo Rao, Yonghua Ding, Qiming Hu *et al*., Plasma Phys. Control. Fusion **55**, 122001 (2013).

[37] J. J. Ellis, A. A. Howling, A. W. Morris and D. C. Robinson, IAEA Proc. 10th Int. Conf. on Plasma Physics and Controlled Nuclear Fusion **1**, 363 (1984).

[38] Z. Yoshida, K. Okano, Y. Seike *et al*., in Plasma Physics and Controlled Nuclear Fusion Energy Research, Proceedings of 9th IAEA Int. Conf. Baltimore, 1982, **3**, 273 (1983).

[39] A. Vannucci, I. C. Nascimento and I. L. Caldas, Plasma Phys. Control. Fusion **31**, 147 (1989).

[40] A. Vannucci and S. C. McCool, Nucl. Fusion **37**, 1229 (1997).

[41] Pulsator Team, Nucl. Fusion **25**, 1059 (1985).

[42] T. C. Hender, R. Fitzpatrick, A. W. Morris *et al*., Nucl. Fusion **32**, 2091 (1992).

[43] M. S. T. Araújo, A. Vannucci and I. L. Caldas, Il Nuovo Cimento **18D**, 807 (1996).

[44] A. Vannucci and R. D. Gill, Nucl. Fusion **31**, 1127 (1991).

[45] P. C. de Vries, M. F. Johnson, B. Alper *et al*., Nucl. Fusion **51**, 053018 (2011).

[46] M. F. F. Nave and J. A. Wesson, Nucl. Fusion **30**, 2575 (1990).

[47] J. Wesson *et al*, Nucl. Fusion **29**, 641 (1989).

[48] R. J. Buttery, M. De' Benedetti, D. A. Gates *et al*., Nucl. Fusion **39**, 1827 (1999).

[49] J. -K. Park, A. H. Boozer, J. E. Menard and M. J. Schaffer, Nucl. Fusion **48**, 045006 (2008).

[50] A. L. Colton, R. J. Buttery, S. J. Fielding *et al*., Nucl. Fusion **39**, 551 (1999).

[51] J. T. Scoville and R. J. La Haye, Nucl. Fusion **43**, 250 (2003).

[52] R. J. Buttery, M. De' Benedetti, T. C. Hender and B. J. D. Tubbing, Nucl. Fusion **40**, 807 (2000).

[53] Yu. V. Petrov, M. I. Patrov, V. I. Varfolomeev *et al*., Plasma Phys. Rep. **36**, 455 (2010).

[54] H. Zohm, Plasma Phys. Control. Fusion **38**, 105 (1996).

[55] T. E. Evans, R. A. Moyer, P. R. Thomas *et al*., Phys. Rev. Lett. **92**, 235003 (2004).

[56] Y. Liang, H. R. Koslowski, P. R. Thomas *et al*., Phys. Rev. Lett. **98**, 265004 (2007).

[57] W. Suttrop, T. Eich, J. C. Fuchs *et al.*, Phys. Rev. Lett. **106**, 225004 (2011).

[58] A. Kirk, E. Nardon, R. Akers *et al.*, Nucl. Fusion **50**, 034008 (2010).

[59] V. Rozhansky, E. Kaveeva, P. Molchanov *et al.*, Nucl. Fusion **50**, 034005 (2010).

[60] P. Tamain, A. Kirk, E. Nardon *et al.*, Plasma Phys. Control. Fusion **52**, 075017 (2010).

[61] S. Saarelma, A. Alfier, Y. Liang *et al.*, Plasma Phys. Control. Fusion **53**, 085009 (2011).

[62] K. H. Finken, S. S. Abdullaev, M. W. Jakubowski *et al.*, Phys. Rev. Lett. **98**, 065001 (2007).

[63] A. Kirk, Yueqiang Liu, E. Nardon *et al.*, Plasma Phys. Control. Fusion **53**, 065011 (2011).

[64] E. J. Strait, T. S. Taylor, A. D. Turnbull *et al.*, Phys. Rev. Lett. **74**, 2483 (1995).

[65] R. J. Buttery, R. J. La Haye, P. Gohil *et al.*, Phys. Plasmas **15**, 056115 (2008),

[66] R. C. Wolf, Plasma Phys. Control. Fusion **45**, R1 (2003).

[67] K. H. Finken, S. S. Abdullaev, M. F. M. de Bock *et al.*, Phys. Rev. Lett. **94**, 015003 (2005).

[68] J. W. Coenen, O. Schmitz, B. Unterberg *et al.*, Nucl. Fusion **51**, 063030 (2011).

[69] L. Frassinetti, S. Menmuir, K. E. J. Olofsson *et al.*, Nucl. Fusion **52**, 103014 (2012).

[70] W. M. Solomon, K. H. Burrell, A. M. Garofalo *et al.*, Nucl. Fusion **49**, 085005 (2009).

[71] H. Reimerdes, A. M. Garofalo, E. J. Strait *et al.*, Nucl. Fusion **49**, 115001 (2009).

[72] Y. Sun, Y. Liang, K. C. Shaing *et al.*, Nucl. Fusion **52**, 083007 (2012).

[73] R. Fitzpatrick, Nucl. Fusion **33**, 1049 (1993).

[74] K. C. Shaing, Phys. Plasmas **10**, 1443 (2003).

[75] A. J. Cole, C. C. Hegna, and J. D. Callen, Phys. Plasmas **15**, 056102 (2008).

[76] R. Fitzpatrick, Phys. Plasmas **5**, 3325 (1998).

[77] M. V. A. P. Heller, R. M. Castro, Z. A. Brasilio *et al*., Nucl. Fusion **35** 59, (1995).

[78] Q. Yu and S. Günter, Nucl. Fusion **49**, 062001 (2009).

[79] H. Stoschus, O. Schmitz, H. Frerichs *et al*., Nucl. Fusion **52**, 083002 (2012).

[80] M. Lehnen, S. A. Bozhenkov, S. S. Abdullaev *et al*., Phys. Rev. Lett. **100**, 255003 (2008).

[81] G. Papp, M. Drevlak, T. Fülöp *et al*., Plasma Phys. Control. Fusion **53**, 095004 (2011).

[82] M. Forster, S. S. Abdullaev, K. H. Finken *et al*., Nucl. Fusion **52**, 083016 (2012).

[83] M. S. Foster, S. C. McCool, and A. J. Wootton, Nucl. Fusion **35**, 329 (1995).

[84] M. Kobayashi, T. Tuda, K. Tashiro *et al*., Nucl. Fusion **40**, 181 (2000).

[85] D. A. Maurer, D. Shiraki, J. P. Levesque *et al*., Phys. Plasmas **19**, 056123 (2012).

[86] R. Fitzpatrick and T. C. Hender, Phys. Fluids B **3**, 644 (1991).

[87] D. Reiser and D. Chandra, Phys. Plasmas **16**, 042317 (2009).

[88] Yueqiang Liu, A. Kirk, and E. Nardon, Phys. Plasmas **17**, 122502 (2010).

[89] Y. Yang, Y. Liang, Y. Sun *et al*., Nucl. Fusion **52**, 074014 (2012).

[90] A. H. Boozer, Phys. Plasmas **3**, 4620 (1996).

[91] Y. Kikuchi, M. F. M. de Bock, K. H. Finken *et al*., Phys. Rev. Lett. **97**, 085003 (2006).

[92] A. Nicolai, U. Daybelge, M. Lehnen *et al*., Nucl. Fusion **48**, 024008 (2008).

[93] M. Bécoulet, G. Huysmans, X. Garbet *et al*., Nucl. Fusion **49**, 085011 (2009).

[94] M. Bécoulet, F. Orain, P. Maget *et al*., Nucl. Fusion **52**, 054003 (2012).

[95] I. Condrea, E. Haddad, B. C. Gregory, and G. Abel, Phys. Plasmas **7**, 3641 (2000).

[96] A. Graf, S. Howard, R. Horton *et al*., Rev. Sci. Instrum. **77**, 10F125 (2006).

[97] J. H. F. Severo, I. C. Nascimento, Yu. K. Kuznetov *et al*., Rev. Sci. Instrum. **78**, 043509 (2007).

[98] Y. Liu, *M.Sc. Thesis*, University of Saskatchewan, Saskatoon (2012).

[99] C. Xiao, S. Elgriw, Y. Liu *et al*., 24th IAEA Fusion Energy Conference, EX/**P4-26** (2012).

[100] W. Zhang, C. Xiao, G. D. Conway *et al*., Phys. Fluids B **4**, 3277 (1992).

[101] A. Teolis, *Computational Signal Processing with Wavelets*, Birkhäuser, Boston (1998).

[102] J. S. Bendat and A. G. Piersol, *Engineering Applications of Correlation and Spectral Analysis 2nd Ed*, John Wiley and Sons Inc. (1993).

[103] C. Nardone, Plasma Phys. Control. Fusion **34**, 1447 (1992).

[104] A. A. Harms, K. F. Schoept, G. H. Miley and D. R. Kingdon, *Principles of Fusion Energy*, World Scientific Publishing (2000).

[105] D. G. Lominadze, *Cyclotron Waves in Plasma*, Pergamon Press (1981).

[106] F. F. Chen, *Introduction to Plasma Physics and Controlled Fusion 2nd Ed*, Plenum Press (1984).

[107] D. A. Gurnett and A. Bhattacharjee, *Introduction to Plasma Physics with Space and Laboratory Applications*, Cambridge University Press (2005).

[108] A. Hirose, *Plasma Waves 1*, Lecture Notes: Chapter 2, University of Saskatchewan, Saskatoon (2007).

[109] K. Miyamoto, *Fundamentals of Plasma Physics and Controlled Fusion*, Iwanami Book Service Center, Tokyo (1997).

[110] K. C. Mark, *M.Sc. Thesis*, University of Saskatchewan, Saskatoon (1993).

[111] J. Freidberg, *Plasma Physics and Fusion Energy*, MIT Press, Cambridge, MA (2007).

[112] L. Spitzer Jr., *Physics of Fully Ionized Gases*, Interscience, New York (1956).

[113] S. M. Kaye, C. W. Barnes, M. G. Bell *et al*., Phys. Fluids B **2**, 2926 (1990).

[114] K. Bol, J. L. Cecchi, C. C. Daughney *et al*., Phys. Rev. Lett. **32**, 661 (1974).

[115] R. S. Hemsworth, A. Tanga, and V. Antoni, Rev. Sci. Instrum. **79**, 02C109 (2008).

[116] H. Takahashi, J. Phys. Colloques **38**, C6-171 (1977).

[117] M. Porklab, *Radio frequency heating of magnetically confined plasma*, Academic Press (1981).

[118] O. Mitarai, S. W. Wolfe, A. Hirose and H. M. Skarsgard, Plasma Phys. Controlled Fusion **27**, 395 (1985).

[119] *Progress Report 1995/96*, Plasma Physics Laboratory, University of Saskatchewan, Saskatoon.

[120] O. Mitarai, H. M. Skarsgard and A. Hirose, Fusion Technol. **20**, 285 (1991).

[121] W. Zhang, C. Xiao and A. Hirose, Phys. Fluids B **5**, 3961 (1993).

[122] A. Hirose, M. Dreval, S. Elgriw *et al*., 17th IAEA Technical Meeting on Research Using Small Fusion Devices, AIP Conference Proceedings Series **996**, 14 (2008).

[123] C. Xiao, S. J. Livingstone, A. K. Singh *et al*., 21st IAEA Fusion Energy Conference, EX/**P4-31** (2006).

[124] C. Xiao, S. Elgriw, M. Dreval *et al*., 22nd IAEA Fusion Energy Conference, EX/**P9-3** (2008).

[125] D. Trembach, C. Xiao, M. Dreval, and A. Hirose, Rev. Sci. Instrum. **80**, 053502 (2009).

[126] M. Dreval, C. Xiao, D. Trembach *et al*., Plasma Phys. Control. Fusion **50**, 095014 (2008).

[127] M. Dreval, D. Rohraff, C. Xiao, and A. Hirose, Rev. Sci. Instrum. **80**, 103505 (2009).

[128] A. Hirose, C. Xiao, O. Mitarai *et al*., Physics in Canada (2006).

[129] S. Sen, C. Xiao, A. Hirose and R.A. Cairns, Phys. Rev. Lett. **88**, 185001 (2002).

[130] C. Xiao, A. Hirose, and S. Sen, Phys. Plasmas **11**, 4041 (2004).

[131] D. Liu, C. Xiao, A.K. Singh and A. Hirose, Nucl. Fusion **46**, 104 (2006).

[132] *TMP/NT 1000 Turbomolecular Pump and Frequency Converter Manual*, Leybold-Heraeus Vacuum Products Inc., Part No. 722-78-018 Edition C, 313B.

[133] *Precision Leak Valve PV-10 Operation and Maintenance*, Veeco Instruments Inc., 287.

[134] M. E. Khonsaari, *Ph.D. Thesis*, University of Saskatchewan, Saskatoon (1990).

[135] J. D. Jackson, *Classical Electrodynamics 3rd Ed*, John Wiley and Sons Inc. (1999).

[136] S. J. Livingstone, *M.Sc. Thesis*, University of Saskatchewan, Saskatoon (2005).

[137] E. Teller, *Fusion, Magnetic Confinement: Volume 1*, Academic Press, New York (1981).

[138] R. D. Hazeltine, F. L. Hinton, and M. N. Rosenbluth, Phys. Fluids **16**, 1645 (1973).

[139] J. E. Morelli, *Ph.D. Thesis*, University of Saskatchewan, Saskatoon (2003).

[140] G. St. Germaine, *M.Sc. Thesis*, University of Saskatchewan, Saskatoon (2006).

[141] B. D. Scott, *An Introduction to Magnetohydrodynamics (MHD), or Magnetic Fluid Dynamics*, Lect. Notes Phys. **670**, 51 (2005).

[142] R. J. Goldston and P. H. Rutherford, *Introduction to Plasma Physics*, IOP Publishing Ltd. (1995).

[143] A. Fridman and L. A. Kennedy, *Plasma Physics and Engineering*, Tylor and Francis (2004).

[144] P. M. Bellan, *Fundamentals of Plasma Physics*, Cambridge University Press (2006).

[145] G. Bateman, *MHD Instabilities*, MIT Press, Cambridge, MA (1978).

[146] A. Jeffrey and T. Taniuti, *Magnetohydrodynamic Stability and Thermonuclear Containment*, Academic Press (1966).

[147] V. E. Golant, A. P. Zhilinsky and I. E. Sakharov, *Fundamentals of Plasma Physics*, John Wiley and Sons Inc. (1980).

[148] K. Miyamoto, *Plasma Physics for Nuclear Fusion*, MIT Press (1987).

[149] A. I. Morozov and L. S. Solovev, *The Structure of Magnetic Fields, In Reviews of Plasma Physics 2*, Consultants Bureau New York (1966).

[150] S. S. Abdullaev, *Construction of Mappings for Hamiltonian Systems and Their Applications*, Lect. Notes Phys. **691**, 219 (2006).

[151] R. B. White, Rev. Mod. Phys. **58**, 183 (1986).

[152] A. Isayama, Y. Kamada, T. Ozeki and N. Isei, Plasma Phys. Control. Fusion **41**, 35 (1999).

[153] A. Hirose, *Plasma Waves 1*, Lecture Notes: Chapter 3, University of Saskatchewan, Saskatoon (2007).

[154] A. B. Hassam and R. M. Kulsrud, Phys. Fluids **21**, 2271 (1978).

[155] J. H. F. Severo, I. C. Nascimento, V. S. Tsypin and R. M. O. Galvão, Nucl. Fusion **43**, 1047 (2003).

[156] R. D. Hazeltine and F. L. Hinton, Phys. Fluids **16**, 1883 (1973).

[157] B. B. Kadomtsev and O. P. Pogutse, Nucl. Fusion **11**, 67 (1971).

[158] F. L. Hinton and M. N. Rosenbluth, Phys. Fluids **16**, 836 (1973).

[159] E. O. Brigham, *Fast Fourier Transform and Its Applications*, Prentice Hall Signal Processing Series (1988).

[160] J. O. Smith III, *Mathematics of the Discrete Fourier Transform: with Audio Applications 2nd Ed*, BookSurge Publishing (2007).

[161] J. W. Cooley and J. W. Tukey, Math. Comput. **19**, 297 (1965).

[162] B. Vidakovic, *Statistical Modeling by Wavelets*, John Wiley and Sons Inc. (1999).

[163] P. Goupillaud, A. Grossmann and J. Morlet, Geoexploration **23**, 85 (1984).

[164] G. Bachman, L. Narici and E. Beckenstein, *Fourier and Wavelet Analysis*, Springer-Verlag New York Inc. (2000).

[165] P. A. Duperrex, A. Pochelon, A. W. Edwards and J. A. Snipes, Nuclear Fusion **32**, 1161 (1992).

[166] W. H. Press, B. P. Flannery, S. A. Teukolsky and W. T. Vetterling, *Numerical Recipes in C: The Art of Scientific Computing 2nd Ed*, Cambridge University Press (1993).

[167] J. S. Kim, D. H. Edgell, J. M. Greene *et al*., Plasma Phys. Control. Fusion **41**, 1399 (1999).

[168] D. Del-Castillo-Negrete, S. P. Hirshman, D. A. Spong and E. F. D'Azevedo, Journal of Computational Physics **222**, 265 (2007).

[169] S. Gamudi Elgriw, *M.Sc. Thesis*, University of Saskatchewan, Saskatoon (2009).

[170] I. H. Hutchinson, *Principles of Plasma Diagnostics 2nd Ed*, Cambridge University Press (2002).

[171] *Datasheet of National Instuments Digitizer Card*, Model No. NI PXI-6133, http://sine.ni.com/nips/cds/view/p/lang/en/nid/14110.

[172] D. Biskamp, *Nonlinear Magnetohydrondynamics*, Cambridge University Press (1993).

[173] C. Xiao, T. Niu, J. E. Morelli *et al*., Rev. Sci. Instrum. **79**, 10E926 (2008).

[174] T. Onchi, Y. Liu, M. Dreval *et al*., Plasma Phys. Control. Fusion **55**, 035003 (2013).

[175] V. I. Demidov, S. V. Ratynskaia and K. Rypdal, Rev. Sci. Instrum. **73**, 3409 (2002).

[176] R. H. Huddlestone and S. L. Leonard, *Plasma Diagnostic Techniques*, Academic Press (1965).

[177] M. Hubeny, *M.Sc. Thesis*, University of Saskatchewan, Saskatoon (2012).

[178] *Datasheet of Eupec IGBT Module*, Model No. FZ1200R17KF4, http://www.datasheetarchive.com/dlmain/Datasheets-10/DSA-194029.pdf.

[179] *Datasheet of Powerex SCR Module*, Model No. T9G0121203DH, http://www.datasheetarchive.com/dlmain/Datasheets-26/DSA-506147.pdf.

[180] J. M. Finn, Nucl. Fusion **15** , 845 (1975).

[181] D. A. Monticello, R. B. White and M. N. Rosenbluth, in Plasma Physics and Controlled Nuclear Fusion Energy Research, Proceedings of 7th IAEA Int. Conf. Innsbruck, 1978, **1**, 605 (1979).

[182] L. H. A. Monteiro, V. Okano, M. Y. Kucinski and I. L. Caldas, Physics Letters A **193**, 89 (1994).

[183] E. C. da Silva, I. L. Caldas and R. L. Viana, IEEE Transactions on Plasma Science **29**, 617 (2001).

[184] R. L. Viana, Solitons and Fractals **11**, 765 (2000).

[185] S. S. Abdullaev, Nucl. Fusion **50**, 034001 (2010).

[186] Q. Yu and S. Günter, Nucl. Fusion **51**, 073030 (2011).

[187] Q. Yu, S. Günter and K. H. Finken, Phys. Plasmas **16**, 042301 (2009).

[188] C. Xiao, S. Elgriw, D. Liu *et al*., 23rd IAEA Fusion Energy Conference, EXS/**P5-15** (2010).

[189] K. Shinya, J. Plasma Fusion Res. **76**, 479 (2000).

[190] S. D. Pinches, *Ph.D. Thesis*, University of Nottingham, UK (1996).

[191] V. Igochine, O. Dumbrajs, D. Constantinescu *et al*., Nucl. Fusion **46**, 741 (2006).

[192] D. E. Roberts, D. Sherwell, J. D. Fletcher *et al.*, Nucl. Fusion **31**, 319 (1991).

[193] Z. A. Pietrzyk, A. Pochelon, R. Behn *et al*., Nucl. Fusion **32**, 1735 (1992).

[194] W. M. Manheimer and C. N. Lashmore-Davies, *MHD and Microinstabilities in Confined Plasma*, IOP Publishing Ltd. (1989).

[195] S. Elgriw, D. Liu, T. Asai *et al*., Nucl. Fusion **51**, 113008 (2011).

[196] R. J. La Haye, R. Fitzpatrick, T. C. Hender *et al*., Phys. Fluids B **4**, 2098 (1992).

[197] M. Kikuchi, K. Lackner and M. Tran, *Fusion Physics*, IAEA Publications (2012).

[198] A. R. Field, J. McCone, N. J. Conway *et al*., Plasma Phys. Control. Fusion **51**, 105002 (2009).

[199] O. Klüber, H. Zohm, H. Bruhns *et al*., Nucl. Fusion **31**, 907 (1991).

[200] M. F. M. De Bock, I. G. J. Classen, C. Busch *et al*., Nucl. Fusion **48**, 015007 (2008).

[201] W. L Rowan, A. G. Meigs, E. R. Solano *et al*., Phys. Fluids B **5**, 2485 (1993).

[202] B. B. Kadomtsev, Phil. Trans. R. Soc. Lond. A **322**, 125 (1987).

[203] Y. B. Kim, P. H. Diamond and R. J. Groebner, Phys. Fluids B **3**, 2050 (1991).

[204] H. A. Claassen, H. Gerhauser, A. Rogister and C. Yarim, Phys. Plasmas **7**, 3699 (2000).

[205] Feng Chun-Hua, Li Zan-Liang, Yang Xuan-Zong *et al*., Chinese Phys. **12**, 1135 (2003).

[206] J. H. F. Severo, I. C. Nascimento, V. S. Tsypin *et al*., Phys. Plasmas **11**, 846 (2004).

[207] B. E. Chapman, R. Fitzpatrick, D. Craig *et al*., Phys. Plasmas **11**, 2156 (2004).

[208] E. D. Taylor, C. Cates, M. E. Mauel *et al*., Phys. Plasmas 9, 3938 (2002).

[209] Qiming Hu, Q. Yu, Bo Rao *et al*., Nucl. Fusion **52**, 083011 (2012).

[210] L. Frassinetti, K. E. J. Olofsson, P. R. Brunsell and J. R. Drake, Nucl. Fusion **50**, 035005 (2010).